Chirality Sorted SWNTs and Their Effect on the Performance of Organic Solar Cells

Doctoral Thesis Presented by

Abasi Abudulimu

For the Degree of Doctor of Philosophy in Condensed Matter Physics and Nanotechnology

FACULTAD DE CIENCIAS

Department of Condensed Matter Physics
Autonomous University of Madrid

Madrid, December 2016

Chirality Sorted SWNTs and Their Effect on the Performance of Organic Solar Cells

Tesis doctoral presentada por

Abasi Abudulimu

Para optar al título de Doctorado Física de la Materia Condensada y Nanotecnologia

FACULTAD DE CIENCIAS

Departamento de Física de la Materia Condensada
Universidad Autónoma de Madrid
Madrid, diciembre de 2016

Directors of Thesis:

Supervisor: Dr. Larry Lüer (IMDEA Nanociencia, Spain)

Co-host supervisor: Prof. Thomas Anthopoulos (Imperial College London, UK)

Co-host supervisor: Prof. Tobias Hertel (Wurzburg University, Germany)

Tutor: Prof. Nicolás Agraït (Autonomous University of Madrid, Spain)

Thesis committee

Prof. Juan Carlos Sancho Garcia (Universidad de Alicante, Spain)

Prof. Jorge Morgado (instituto Superior Tecnico Lisboa, Portugal)

Prof. Martin Heeney (Imperial College London, United Kingdom)

Dr. Felix Zamorra (Universidad Autónoma de Madrid/IMDEA Nanociencia)

Dr. Friedrich Schoeppler (University of Wurzburg, Germany)

Dr. Emilio Perez (IMDEA Nanociencia, Spain)

Dr. Cristina Flors (IMDEA Nanociencia, Spain)

The European Union Seventh Framework Network Program funded this research

(FP7/2011 under grant agreement POCAONTAS, Project No: 316633)

Acknowledgements

First and foremost, I thank my supervisor, Dr. Larry Lüer, for giving me the chance to go on this PhD journey in his group, for his inspiration, encouragement and guidance during the last three years. I am grateful for his strong support on my traveling for various conferences, workshops and trainings all over the Europe as well as on my future career. His kindness and patients during my training on the experimental setup, spectral modelling and scientific writing kept me warm and active all the way long. One of the most important things that I have learnt from him besides the science is that never mix the personal life with work, never judge someone or someone's work based on his/her color, ethnic group, gender, marital status, citizenship, and speak with proof. I saw how a great scientist can be like.

I am grateful to all my secondment co-supervisors, Prof. Thomas Anthopoulos from the Department of Physics at Imperial College London, Prof. Tobias Hertel from the Institute of Physical and Theoretical Chemistry at Julius-Maximilians University Würzburg and Dr. Andreas Distle from BELECTRIC OPV GmbH Nuremberg, for hosting me and making their whole lab facilities available for me as well as for the great scientific collaborations we have. My thanks should be to all their group members as well, specially to Dr. Francesca Bottacchi for training me on FET, Dr. Florian Späth, Imge Namal, Klaus Eckstein, Dr. Friedrich Schöppler for helping me on SWNT preparation, Dr. Mirella El Gemayel for training me on the OSC preparation, and Dr. Hendrik Faber, Dr. James Semple, Dr. Daniel Schilling, Matthias Kastner, Kerstin Müller, Melanie Achsnich, Sabine Stahl, Sabine Walther, Dr. Han Li, Dr. Sebastian Meier for their help and support during my stay in their lab.

I am very thankful to IMDEA Nanoscience for hosting my PhD and being always helpful. I thank its members: Dr. Juan Cabanillas for the scientific discussions, suggestions and with the translation of my thesis abstract, Dr. Johannes Gierschner for the intensive theoretical lectures, discussions and lunch laughs, Dr. Reinhold Wannemacher for the technical support, suggestions and critical questions, Dr. Cristina Flors for her help on Spanish and tax declaration, Patricia Bondia for being extremely helpful, patient and supportive, Patricia Pedraz for helping me with the thesis deposition, Warren Smith for making sample holders for me, Dr. Shafkath Karuthedath, Dr. Nandajan P.C.,

Gui Lin, Long Fei, Jun Qing, Andres Black, Sun Chen and Dr. Anna Isakova for adding colors to my PhD life by being good friends and colleges; Dr. Marije Villa, Rodolfo Miranda Soriano, Patricia López, Isabel Rodríguez, Juana Hermoso, Bonifacio Vega Garcia, Paloma Macua, Oscar Bodas Gómez for helping me on the administrative, Visa, financial reimbursement and technical matters. I am also very thankful to Dr. David Sayago for all his help for the last two years from welcoming me at the airport to handling all my official stuffs, and being so kind and friendly.

I would like to acknowledge and thank European Union Seventh Framework Network for funding my PhD study through the POCAONTAS project, and all project coordinators and principal investigators, who made the project possible and created the excellent research environment for us—the students. All POCAONTAS fellows being part of such an amazing PhD journey deserve considerable thanks too.

Finally, my deepest gratitude is to my parents, Abbas Sattar and Khamhan Amut, for being always supportive and enthusiastic about my studies and decisions, to my brother and sisters for taking care of mum and dad, to my wife, Ayjamal, for taking care of Wisal, putting up with my foul moods, complaints, personal transition from a cheerful musician to a silent researcher, and to my little angel, Wisal, for bearing with the little time I had for her. I also thank my relatives, neighbors, friends as well as the rest whom I forgot to mention.

Abstract

Following the fast economic and social development, the energy demand has increased drastically for decades almost at every single corner of the world from daily life to industry. Such demand has been fulfilled mainly by fossil fuels, which in return brought the world unbelievable environmental damages ranging from air quality to global warming, from soil to water. In addition to that, their limited source, predicted to last hardly 150 years, put a question mark on the direction of the social development and future of the humanity. One of the alternatives for the conventional energy resources is converting the free, clean and renewable energy—sunlight—to electrical energy using organic solar cells. Despite great efforts made, the power conversion efficiency of them is still low due to the slow charge carrier mobilities in organics. Single wall carbon nanotubes (SWNTs) can be one of the candidates to advance that with its high charge carrier mobility and tunable bandgap properties, but has not been succeeded yet. As its fundamental photophysics is not completely understood due to the challenges in preparing individual or pure single chirality samples, and controlling them on the nanoscale.

Goal of this dissertation is to understand the fundamental photophysical properties of SWNT/polymer blend especially with respect to their deployment in organic solar cells. First, very pure (6,5) and (7,5) SWNT chiralities are sorted by applying a series of purification techniques to overcome some known issues related to the mixing of chiralities in a sample. Then, the samples are studied by time dependent transient absorption spectroscopy from 100 femtoseconds to 50 microseconds focusing on identifying possible excited state species and their dynamics. By conducting global spectral simulation on the complex transient absorption spectra, the dynamics of biexciton, trion, charge and triplet states are traced qualitatively. A method is developed that allows for the first time the tracing of triplet exciton transfer separately for each chirality.

To get information about carrier mobility in the bulk SWNT network film, bottom-gate bottom-contact field effect transistors are built from the (6,5) and (7,5) chirality enriched SWNT/polymer blends, respectively, on commercially available pre-digitalized Si/SiO_2 substrates. Irrespective to the tube chirality, the effective field effect hole carrier mobility of the SWNT/polymer networks is found in the range of 0.4-0.8 $cm^2V^{-1}s^{-1}$. Surface characterization by atomic force microscopy

revealed that there is no preferential alignment on the distribution of spin-casted SWNTs on the substrate; instead, we found a random distribution and a high aggregation tendency. The random distribution of SWNTs led quite often to failure on building a successful device by either not covering the channel when a diluted SWNT dispersion is used, or creating shorts when a concentrated dispersion is used. The random distribution of the SWNTs is proposed as one of the main reasons for delivering a 10^4 times lower carrier mobility than the recently published value on similar but aligned SWNTs.

After studying the photophysics and carrier mobility of the SWNTs, P3HT:PCBM and OPV48:PCBM bulk hetero junction solar cells are fabricated by integrating the chirality sorted SWNTs in the active layer. The effect of SWNTs on the device performance is tested with standard electrical characterization. The J-V characteristics showed that the OSC devices with SWNTs perform worse in contrast to the devices without them. It is not surprising though, as many other groups have observed similar results, and the system is not yet optimized. To shed light on the main effect of SWNTs on the decisive factors limiting the electrical performance, a femtosecond transient absorption spectroscopy in combination with transient photovoltage, transient photocurrent and microsecond transient absorption spectroscopy is applied.

It is found that SWNTs, if used in low enough concentration to avoid shorting by metallic tubes, improves charge extraction only very little, but increase the bimolecular recombination coefficient by a factor of two. At low SWNT concentration, the devices thus do not benefit from the high charge carrier mobilities in the SWNTs. This finding is confirmed by reconstructing the measured J-V curves with the experimentally obtained device parameters. The small amount of SWNTs, incorporated in the active layer did not form a uniform network but isolated islands or aggregation sites, hence did not successfully transport the collected charge carriers to the electrodes but in opposite helped the carrier recombination.

Resumen

Tras el rápido desarrollo económico y social, la demanda de energía ha aumentado drásticamente durante décadas casi en cada rincón del mundo, tanto en la vida diaria como en la industria. Esta demanda se ha satisfecho principalmente con los combustibles fósiles, que a su vez produjeron inmensos daños ambientales que van desde afectar a la calidad del aire hasta el calentamiento global, desde el suelo hasta el agua. Además de eso, se trata de un recurso limitado, con una duración prevista de apenas 150 años, lo cual pone un signo de interrogación en la dirección del desarrollo social y el futuro de la humanidad. Una alternativa a los recursos energéticos convencionales es convertir una energía libre, limpia y renovable, como la luz solar, en energía eléctrica utilizando células solares orgánicas. A pesar de los grandes esfuerzos realizados, la eficiencia de conversión de potencia de los mismos sigue siendo baja debido a la lenta movilidad de carga en los materiales orgánicos. Los nanotubos de carbono de pared única (SWNTs) pueden ser uno de los candidatos para avanzar ya que poseen una alta movilidad de carga y un "bandgap" sintonizable, pero aún no se ha conseguido. Esto es debido a que su fotofísica fundamental no se entiende completamente a causa de la dificultad en la preparación individual o pura de las muestras de quiralidad única, y el control de las mismas en la nanoescala.

El objetivo de esta tesis es comprender las propiedades fotofísicas fundamentales de SWNT / mezcla de polímeros concretamente en su aplicación en células solares orgánicas. En primer lugar, las quiralidades muy puras (6,5) y SWNT (7,5) se separan aplicando una serie de técnicas de purificación para superar algunos problemas conocidos relacionados con la mezcla de quiralidades en una muestra. A continuación, se estudian las muestras mediante espectroscopia de absorción transitoria dependiente del tiempo, desde 100 femtosegundos hasta 50 microsegundos, centrándose en la identificación de posibles especies de estado excitado y su dinámica. Mediante la realización de la simulación espectral global sobre los espectros de absorción transitorios complejos, se rastrea cualitativamente la dinámica de los estados de biexcitón, trión, carga y triplete. Se desarrolla un método que permite por primera vez el rastreo de excitones triplete de transferencia por separado para cada quiralidad.

Para obtener información sobre la movilidad de cargas en la película de la red de SWNT de forma global, se construyeron transistores de efecto de campo a partir de las mezclas SWNT/polímero

enriquecidas en quiralidad (6,5) y (7,5) respectivamente, en sustratos comerciales de Si SiO2 pre-digitalizados. Independientemente de la quiralidad del tubo, el efecto de campo efectivo en la movilidad de cargas en las redes SWNT / polímero se encuentra en el intervalo de 0,4-0,8 $cm^2V^{-1}s^{-1}$. La caracterización de la superficie mediante microscopía de fuerza atómica reveló que no existe alineación preferencial en la distribución de los SWNTs sobre el sustrato. En cambio, encontramos una distribución aleatoria y una alta tendencia de agregación. La distribución aleatoria de SWNTs es la causa del fallo en la construcción del dispositivo, ya sea por no cubrir el canal cuando se utiliza una dispersión SWNT diluida, o por la creación de cortocircuitos cuando se utiliza una dispersión concentrada. La distribución aleatoria de los SWNTs se propone como una de las razones principales por las que se obtiene una movilidad 10^4 veces menor de carga que el valor publicado recientemente en SWNTs similares, pero alineados.

Después de estudiar la fotofísica y la movilidad de las cargas de los SWNTs, P3HT: PCBM y OPV48: las células solares de hetero-unión en masa de PCBM se fabricaron integrando los SWNTs clasificados por la quiralidad en la capa activa. El efecto de SWNT en el rendimiento del dispositivo se prueba con la caracterización eléctrica estándar. Las características J-V mostraron que los dispositivos OSC con SWNTs funcionan peor en comparación con los dispositivos sin ellos. Estono es sorprendente, ya que otros grupos han observado resultados similares, y el sistema aún no está optimizado. Para aclarar el efecto principal de los SWNT sobre los factores decisivos que limitan el rendimiento eléctrico, se aplica espectroscopia de absorción transitoria de femtosegundo en combinación con fotovoltaje transitorio, fotocorriente transitoria y espectroscopia de absorción transitoria de microsegundos.

Se observa que los SWNTs, si se usan en concentraciones suficientemente bajas para evitar el cortocircuito por tubos metálicos, mejoran la extracción de carga muy poco, pero aumentan el coeficiente de recombinación bimolecular por un factor de dos. A baja concentración de SWNT, los dispositivos no se benefician de las movilidades de de carga altas en los SWNT. Este hallazgo se confirma reconstruyendo las curvas J-V medidas con los parámetros del dispositivo obtenidos experimentalmente. La pequeña cantidad de SWNTs, incorporada en la capa activa no formó una red uniforme, sino islas aisladas o sitios de agregación, por lo tanto no transportó con éxito las cargas recogidas en los electrodos aunqueayudó a la recombinación de las misma.

Table of Contents

List of Figures

List of Tables

1 INTRODUCTION AND THEORY

1.1 Motivation

Figure 1-1. Fossil fuels use in (a) power plants, (b) industry related combustion, (c) shipping, (d) mining, (e) residential use and (f) city transport, adapted from [1-1--6]

As represented in the Figure 1-1, from daily life to running the industry we need energy. Energy sector plays a key role on economic growth and social development. For energy, almost all countries in the world have been relying heavily on fossil fuels such as oil, coal and natural gas.

None of these is renewable, and all will eventually be used off within the near future. Economically their production cost is already considerable, and is bound to increase in time [1-7]. Another important fact to mention is that none of them is environmental friendly. Some of the main air pollutants generated from energy production and uses are given in Figure 1-2.

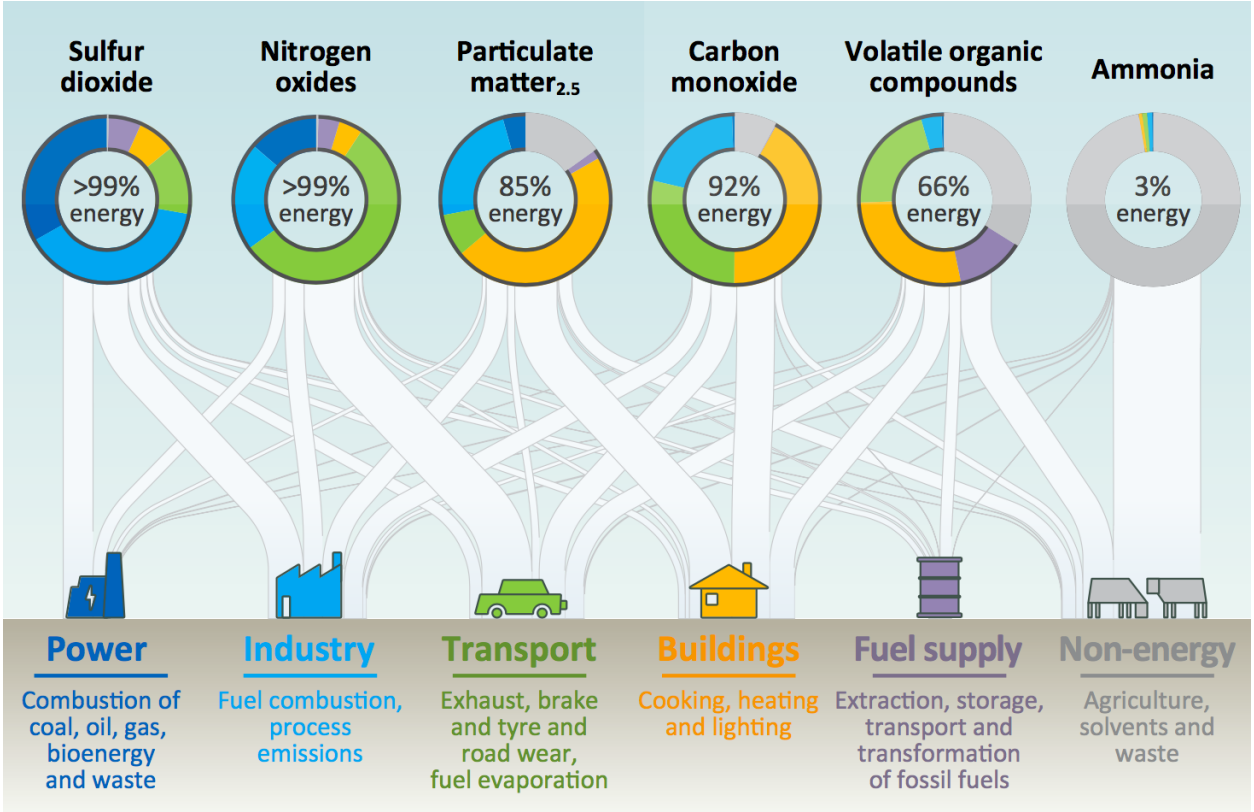

Figure 1-2. Some of the main air pollutants result from energy production and use, adapted from [1-9]

The damage caused by production and usage of the energies from those conventional sources is terrifying. For example, electrical power generation from those energy sources leads to the production of sulfur dioxide (SO_2), nitrogen oxides (NO_x), ozone (O_3), particulate matter, carbon dioxide (CO_2), radioactive waste and mercury etc. [1-8]. SO_2 is the reason for acid rain, and it could increase rate of cardiovascular diseases. NO_x produce smog and ozone, affects the lungs and decreases the immunity for infections. Particulate matter called soot is dangerous for people with lung and heart diseases. CO_2 is the main reason for global warming, which then facilitates infectious spreading. According to the WORLD Energy Outlook Special Report produced by the International Energy Agency in 2016, 6.5 million people have died due to the poor air quality

related sicknesses [1-9]. Standing just after the smoking, the air pollution made it to the top forth in the list of critical threats for human health.

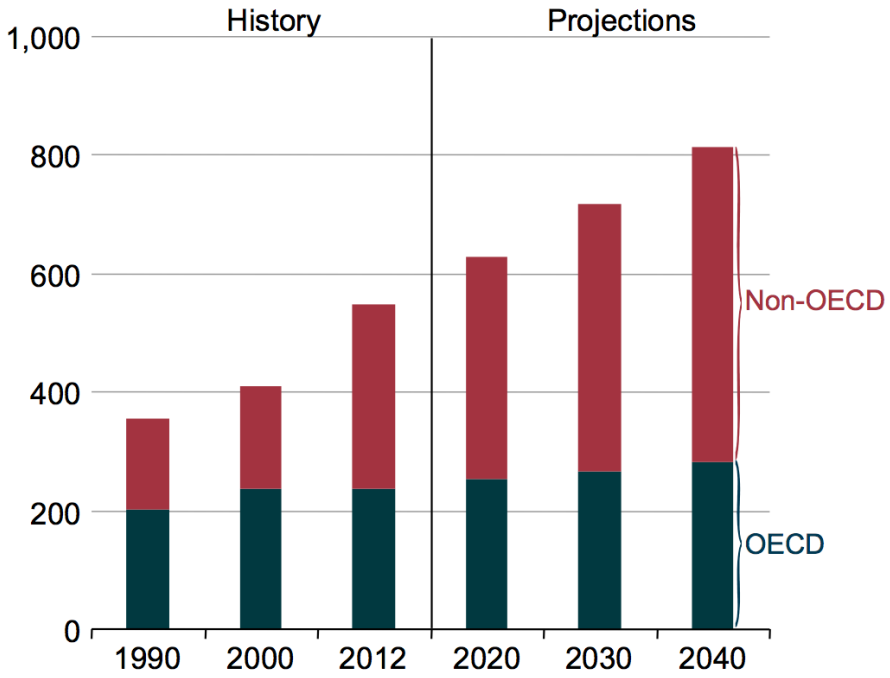

Figure 1-3. World energy consumption from 1990 to 2040 (quadrillion British thermal unit), adapted from [1-10]

Despite that, the demand of world's energy need has been climbing considerably in recent years, and is predicted to increase by 48% by 2040 in the International Energy Outlook in 2016 (see Figure 1-3). The net electricity demand alone rises by 1.9-2.5% per year on average from 2012 to 2040 (see Figure 1-4). Using those sources to generate power not only triggers air pollution but also the pollution of land and water creating an unimaginable manmade world, which will be left for our children or grandchildren. Recognizing these threats, governments and inter-governmental organizations have started developing and building renewable energy technologies and facilities worldwide to supply at least part of the world´s energy need. In 2016 Marrakech Summit, some of the top polluting countries in the world like US and China have stated that they will reduce emissions by investing more on renewable energy production and use [1-11]. For example, US set its roadmap on emissions to an 80% reduction by 2050, and China to installing 200 million kilowatts of wind power and 100 million kilowatts of photovoltaic power by 2020 [1-12].

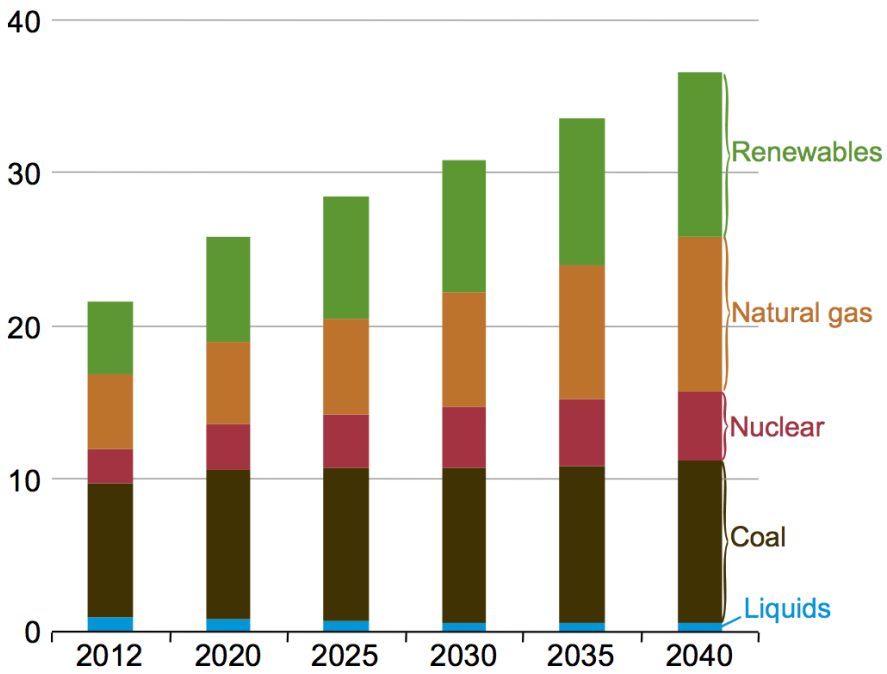

Figure 1-4. World electricity generation from 2012 to 2040 (trillion kilowatt hours), adapted from [10]

Renewable energy is the energy whose source recovers naturally in a short period. Sunlight, wind and waves are some of the examples. This work relates to improving power conversion efficiency (PCE) of organic solar cells (OSCs)—one of the most rapidly evolving sunlight-energy-converting technologies [1-13]. In an OSC, a mixture of organic materials is used to harvest and convert sunlight into electricity [1-14]. Expectations from OSCs are high due to their mechanical flexibility, low production cost and easy processability [1-15].

There is tremendous progress in research as well as in technology, but OSCs have not made it to market yet except for few examples [1-16], because they have been suffering from low PCE compared to their counterpart--inorganic solar cells [1-17]. However, due to their much lower energy payback time, OSCs soon could take over the market. The energy payback time is the amount of time that a solar cell takes to produce the same amount of energy that spent on fabricating it; typical values are about 0.3 years for OSCs and 1-2 years for inorganic solar cells [1-18]. One of the main reasons for the low PCE is the low charge carrier mobility or low carrier extraction efficiency in organic materials [1-19]. Single walled carbon nanotubes (SWNTs) have been reported to possess high carrier mobility and can be used as sunlight harvester, electron donor, acceptor, carrier transport agent and electrode in OSCs [1-20].

The motivation of this work is to understand the details of the photophysics in SWNT/polymer blends in OSC, with a special emphasis on long-lived photoexcitations such as triplet states and charged states. The results are supposed to yield design principles for more stable and more efficient OSC comprising SWNT/polymer blends.

Figure 1-5. Figure 1-5. Examples of OSC applications, adapted from [14]

1.2 Organic Solar Cells

1.2.1 Brief Introduction

Most common types of OCSs are single layer, bilayer and bulk heterojunction. Single layer, the first OSC [1-21], is the simplest one, in which only one single type of semiconductor (mainly a conjugated polymer or small molecule) is sandwiched between two electrodes with a certain offset in electron affinity. A conjugated polymer is a large system constituted from alternating single and double carbon bonds. Upon sunlight absorption by the polymer, excitons—Coulombically bound electron hole pairs, will be generated. Then, the electric field created by the work function difference between the two different metal electrodes splits the optically created excitons into free charge carriers and pushes them towards the electrodes. It was later realized that the electric field created by the work function difference of the electrodes is not sufficient to efficiently split the excitons, thus results in lower PCE. Then Tang *et. al.* pioneered the bilayer devices making a device with two active layers, constituted from copper phthalocyanine and perylene tetracarboxylic derivative [1-22]. The two materials with different electron affinity were chosen specifically to create a local electric field to split the excitons more efficiently. This type of structure is known as planar donor-acceptor heterojunction, as one of the layers made from low electron affinity material works as electron donor and the other made from high electron affinity material as electron acceptor. Bilayer OSCs performed better than single layer owing to the more efficient exciton splitting at the junction interface, but the performance was limited by the short exciton diffusion length in organic semiconductors (about 10nm), as the excitons created at sites further from the junction interface still could not participate in carrier generation. Later bulk hetero junction (BHJ) OSC was proposed [1-23], where the two layers were strongly intermixed to facilitate the exciton splitting everywhere in the active layer. This type of devices delivers higher PCE in contrast to the single layer and bilayer devices, due to the improved charge generation in the active layer, however, suffers from carrier extraction, if there are no efficient percolative pathways towards electrodes. Therefore, a compromise between the best carrier generation and best carrier extraction must be designed and kept during the lifetime of the device.

1.2.2 Basic Principles

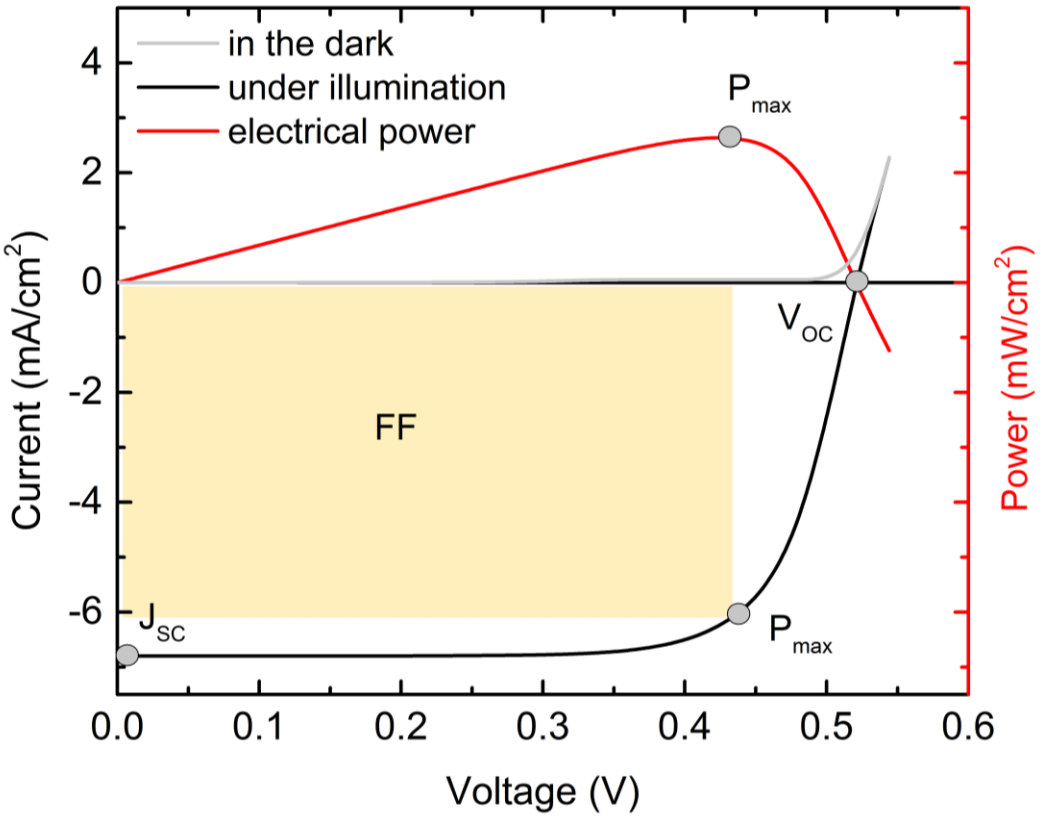

Figure 1-6. J-V characteristics of an exemplary OSC

PCE (η) is a term for indicating the performance of an OSC obtained from electrically measured J-V curve as illustrated in Figure 1-6. It is defined from the maximum electrical power output (P_{out}) and power of incident solar irradiance P_{in} (the standard is 1000W/m^2 with AM1.5G spectrum as shown in Figure 1-7). P_{out}, in its turn, is a product of open circuit voltage (V_{oc}), short circuit current density (J_{sc}) and fill factor (FF).

$$\eta = \frac{P_{out}}{P_{in}} \times 100\% = \frac{V_{oc} J_{sc} FF}{P_{in}} \times 100\% \quad (1\text{-}1)$$

FF is the shaded area in the Figure 1-6, defined by dividing the product of voltage and current at maximum power point (V_{mp} and J_{mp}) by the product of V_{oc} and J_{sc},

$$FF = \frac{V_{mp} J_{mp}}{V_{oc} J_{sc}} \quad (1\text{-}2)$$

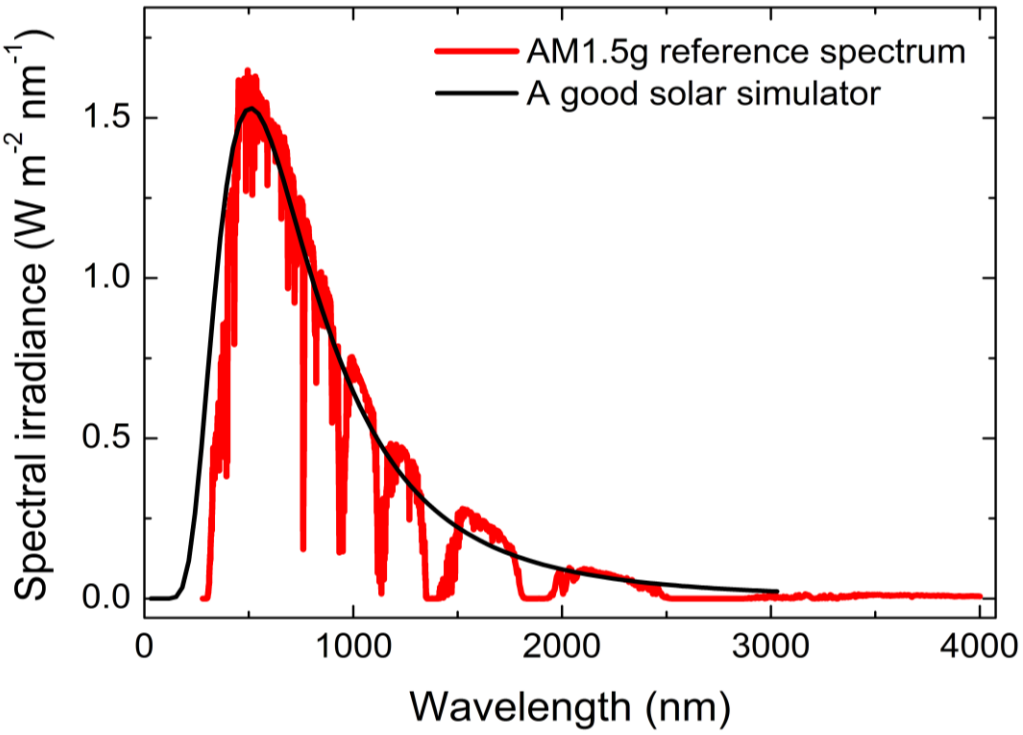

Figure 1-7. Spectral irradiance of the AM1.5g solar spectrum and of a good solar simulator, adapted from [1-24]

V_{oc} can be defined by the empirical relationship between HOMO and LUMO energy level of donor and acceptor materials, respectively,

$$V_{oc} = \frac{1}{e}(E_{HOMO}^{donor} - E_{LOMO}^{acceptor}) - 0.3V \quad (1\text{-}3)$$

where e is elementary charge, the 0.3V is empirical [1-25] and could vary depending on the material. The degree of Ohmic contacts between active layers and electrodes [1-26] as well as the morphology of the active layer are also known to affect its value [1-27]. Ohmic contact means a linear current-voltage characteristic (obeying the Ohm's law) at the junction formed by two materials.

J_{sc} is spectral response of the device, and expressed in terms of wavelength (λ) dependent external quantum efficiency ($EQE(\lambda)$), photon flux density ($\phi_{ph}(\lambda)$) [1-28],

$$J_{sc} = e \int \phi_{ph}(\lambda)\, EQE(\lambda) d\lambda \quad (1\text{-}4)$$

EQE is a product of individual quantum yields for photon absorption, charge carrier generation and extraction [1-29],

$$EQE = \phi_{abs.}\phi_{gen.}\phi_{etra.} \quad (1\text{-}5)$$

Experimentally it can be calculated as,

$$EQE(\lambda) = hv\frac{J_{sc}}{P_{in}} = \frac{1240\,J_{sc}}{\lambda\,P_{in}} \quad (1\text{-}6)$$

where h Planck's constant, v is is the frequency of the light, λ is in nm, J_{sc} is in $\mu A/cm^2$, P_{in} in W/m^2.

FF is governed by the charge density collected at the electrodes, the charge carrier mobility, morphology of the active layer and interfacial and bulk carrier recombination [1-30]. Both carrier density and carrier mobility affect the *FF*. However, it is difficult to separate the contribution of charge density from the charge mobility. As in organic materials, the more the charge density the higher the mobility gets, because the traps can be filled when more charges are generated. The mobility can also be increased by optimizing the morphology and crystallinity of the active layer. Reduction of FF can lead to EQE and PCE losses.

1.2.3 Elementary Processes

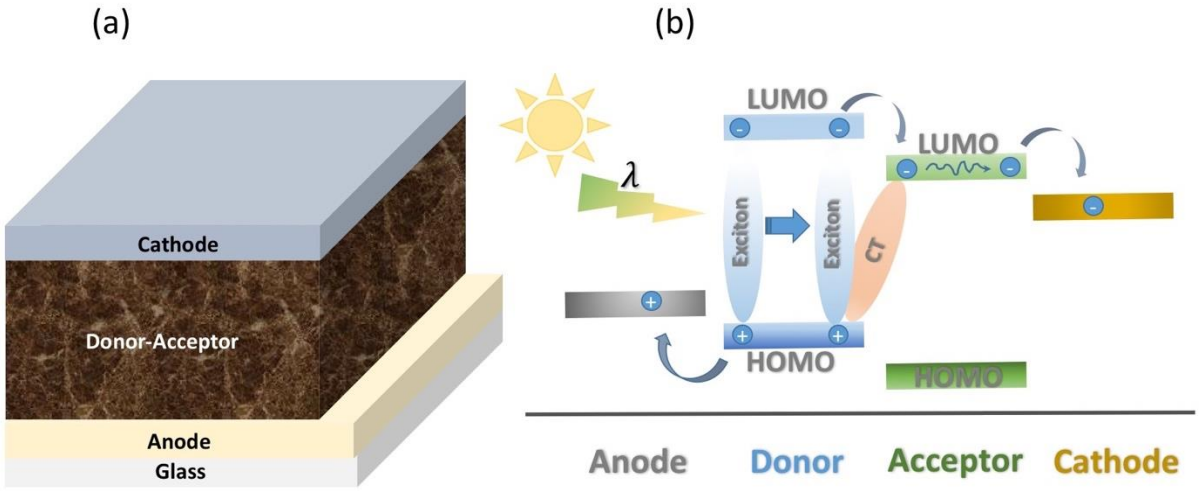

Figure 1-8. (a) Schematics of BHJ OSC, and (b) simple illustration of the physical processes

Converting sunlight into electrical power in an OSC takes a series of sequential physical processes after sunlight absorption by the active layer of the device, namely, exciton generation, exciton diffusion, exciton dissociation, carrier transport and carrier collection at the electrodes, as illustrated in Figure 1-8.

Exciton Generation. Upon absorption of photons (with an energy equal to or higher than the optical bandgap of one of the materials comprising the active layer) by the active layer, the electrons will be excited from the ground state to the excited state of the material leaving holes behind. Instead of forming free charge carriers as in an inorganic semiconductor, the excited electrons Coulombically bound with holes and form so-called excitons [1-31], because of the low dielectric constant, high electron correlation and geometrical relaxation effects in organic materials [1-32]. Different from inorganic semiconductors, the exciton binding energy in organic materials is typically far above kT (25mV) at room temperature. [1-33].

Exciton Diffusion. Excitons generated on the donor material at sites far from the heterojunction interface will diffuse towards the junction interface via a random hopping mechanism [1-34]. Exciton diffusion length has been reported to be about 10-20nm [1-35]. The short diffusion length is not an issue in BHJ OSCs, but one of the main issues in the bilayer devices, because the active layer must be at least 100nm thick to capture the incident sunlight efficiently.

Exciton Dissociation. At the donor-acceptor interface, excitons can dissociate into charge carriers due to the HOMO and LUMO level difference of the donor and accepter material, and the positive holes stay on donor while the electrons accommodate on the acceptor. Although the positive holes and negative electrons settle on two different phases, they will be still bound by a weak Coulombic force as they are close to each other, and form charge transfer (CT) states. Formation of CT can also occur in an ultrafast process by direct absorption if there is a certain amount of wavefunction overlap between ground state and CT state [1-36, 1-37]. The charges residing in the CT state can recombine and lead to PCE loss in the device. However, dissociation of such bound charge carriers at CT is known to be very efficient [1-38]. The reason is that although their binding energy exceeds the thermal energy, it is assumed that energetic or morphological disorder or delocalization of charges within the polymer chain could trigger their separation [1-39--41].

Carrier Transport and Collection. Under the action of the built-in field (electric field generated by the work function difference of the two electrodes), the dissociated charge carriers move towards the electrodes, electrons to the cathode and holes to the anode. Unlike the band transport in inorganic semiconductors, the charge transport in organic semiconductors takes place mainly through charges hopping from one energy site to the other due to the lack of long-range order.

However, the active layer of BHJ OSC is very intensively mixed such that if a free charge is not extracted fast enough the probability of the charge recombining with an opposite charge generated at a neighboring site can be high, which reduces the PCE.

Carrier Recombination. Charge carrier mobility in organic materials is low, typically ranging from 10^{-3} to $10^{-6}\, cm^2V^{-1}.s^{-1}$, and second order nongeminate (also called bimolecular) recombination mechanism dominates the free charge carrier recombination, described by Langevin theory [1-42, 1-43]:

$$\frac{dn}{dt} = \frac{dp}{dt} = R = k_b(n(t)p(t) - n_i^2) \tag{1-7}$$

where n, p, n_i and k_b are electron, hole, intrinsic carrier density and bimolecular recombination coefficient, respectively [1-44]. The k_b can be expressed as [1-42]:

$$k_b = \frac{f_{sub}\, e}{\varepsilon_r \varepsilon_0}(\mu_e + \mu_h) \tag{1-8}$$

where e is elementary charge, f_{sub} is sub-Langevin factor, ε_r and ε_0 are the dielectric constants of vacuum and semiconductor, and μ_e and μ_h are the mobilities of electrons and holes. Since in eq. (1-7), only the time dependence of n and p is considered but not the dependence on the spatial coordinates, the solar cell is considered as a homogeneous medium. In reality, there are various factors spatially separating negative from positive charges, e.g. due to the different donor and acceptor phases, due to the extraction field, or due to energetic disorder being different in the bulk or at the D-A interface. Therefore, it is usually found that R in eq. (1-7) in BHJ solar cells is significantly less than expected in a homogeneous medium [1-42, 1-45, 1-46]. These observations are accounted for by introducing the Sub-Langevin factor f_{sub} in eq. (1-2). Nonetheless, free carrier loss due to the recombination can be reduced by choosing donor-acceptor materials with higher carrier mobilities, better morphology. Finally, the two electrodes must be chosen carefully in a way that their work functions should match the HOMO of donor and LUMO of acceptor materials to efficiently collect the charge carriers at electrodes. Choosing proper electrode materials could also reduce the sub-Langevin factor.

1.3 SWNTs and Their Electronic Properties

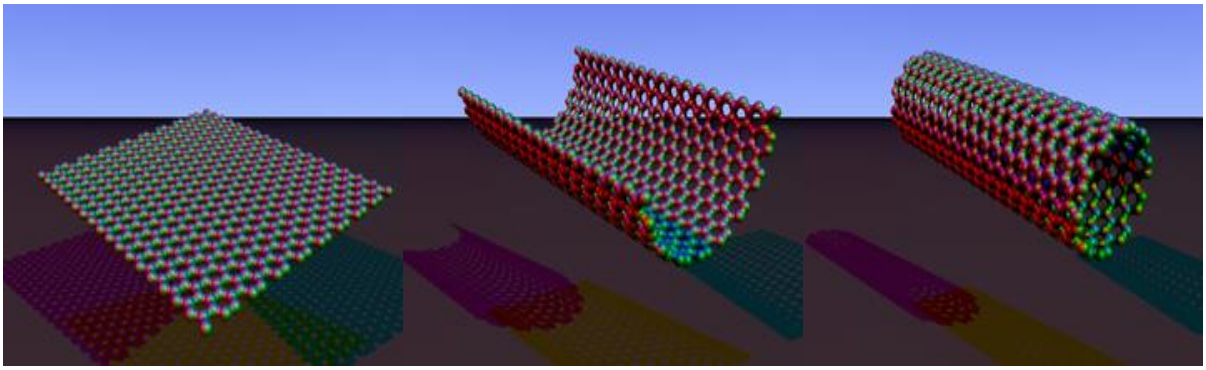

Figure 1-9. Transforming a single layer graphene sheet into a SWNT, adapted from [1-47]

A single walled carbon nanotube (SWNT) can be simply thought of as a long but thin cylinder like structure made by rolling up a single layer graphene sheet in a certain way (Figure 1-9). To classify SWNT, a roll-up vector is defined by a pair of chiral indices (n, m) as shown in Figure 1-10. These chiral indices can vary the electrical and optical properties of the nanotubes quite significantly.

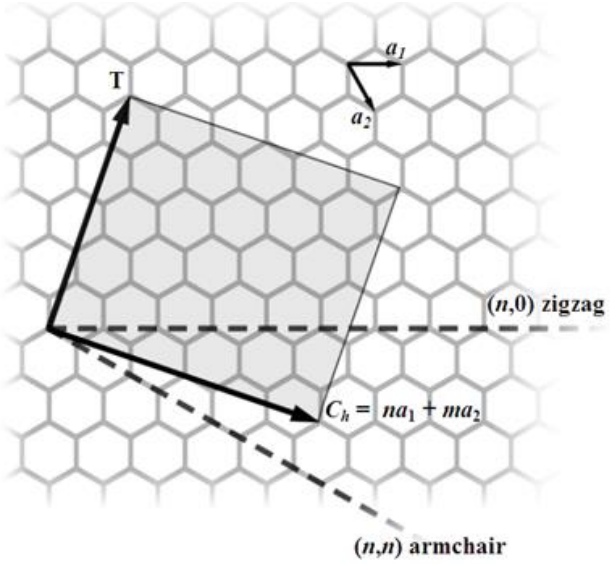

Figure 1-10. SWNTs defined by the rolling direction of a graphene sheet, adapted from [1-48]

Figure 1-10 is an example of possible ways for wrapping a graphene sheet into a nanotube, where C_h is the chiral vector or circumference vector, defined by integer numbers (n, m) of hexagonal graphene unit vectors (a_1, a_2), indicates the rolling direction, and T denotes the tube axis. Depending on the values of n and m, nanotubes usually are grouped into three main categories, namely zigzag $(n, 0)$, armchair (n, n) and chiral (n, m). The diameter of a tube can be calculated from the graphene unit vector and the chiral indices through the following relation:

$$d = \frac{a}{\pi}\sqrt{(n^2 + nm + m^2)} \quad (1\text{-}9)$$

where $a = a_1 = a_2 = 0.246$nm.

Since nanotubes are made from graphene sheets, the band structure of graphene defines the electronic structure of nanotubes. Armchair tubes are always metallic. Under the condition of n-m=3q (q is integer), chiral and zigzag tubes in most cases show metallic properties, while the others which do not meet that condition exhibit semiconducting properties [1-49]. This rule has some exceptions though due to the strong effect of tube curvature on the electrical properties of small diameter tubes [1-50]. It is also known that the electronical properties of nanotubes can vary with their diameter, and an inverse radius dependence of bandgaps has been reported for semiconducting nanotubes [1-51]. Metallic tubes conduct in one dimension owing to their small diameter, and being capable of caring a thousand times ($4 \times 10^9 A/cm^2$) more current density than copper [1-52], they can be a great candidate for electronic applications. The semiconducting properties of the SWNTs can also be tuned by modifying the chiral indices or diameter.

1.3.1 Optical Properties of SWNTs

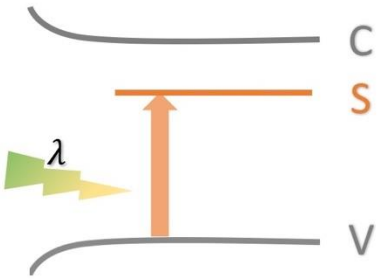

Figure 1-11. Density of States of semiconducting SWNT. V, C and S represents valance band, conduction band and excitonic band, respectively

Because of the high aspect ratio, the SWNTs are often considered as one-dimensional systems. Their density of electronic states (DOS) is described by non-continuous functions of energy—sharp peaks, so-called van Hove singularities, as depicted in Figure 1-11. The optical transitions in semiconducting SWNTs mainly arise from their excitonic bands that lie several hundred meV below the band gap [1-53]. Due to the van Hove singularity of the band structure and the strong excitonic feature, the optical transitions in SWNTs occur to be quite sharp, see the absorption spectra of (6, 5) rich sample displayed in Figure 1-12.

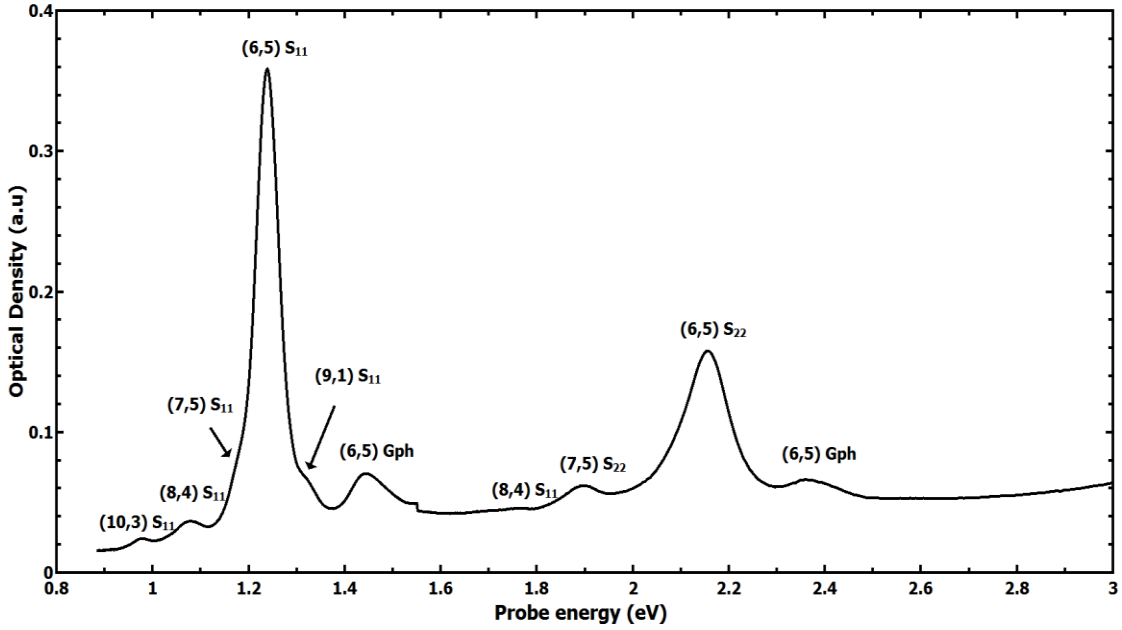

Figure 1-12. Absorption spectra of a (6,5) rich SWNT film

Since the electronic structure is defined by the chiral indices, the optical properties of SWNTs can also be tuned by varying them. Such a relationship between the chiral indices and optical properties can be predicted from the Kataura plot [1-54]. Figure 1-13 shows the dependence of optical transitions on the tube diameter. Increasing the tube diameter decreases the optical transition energy.

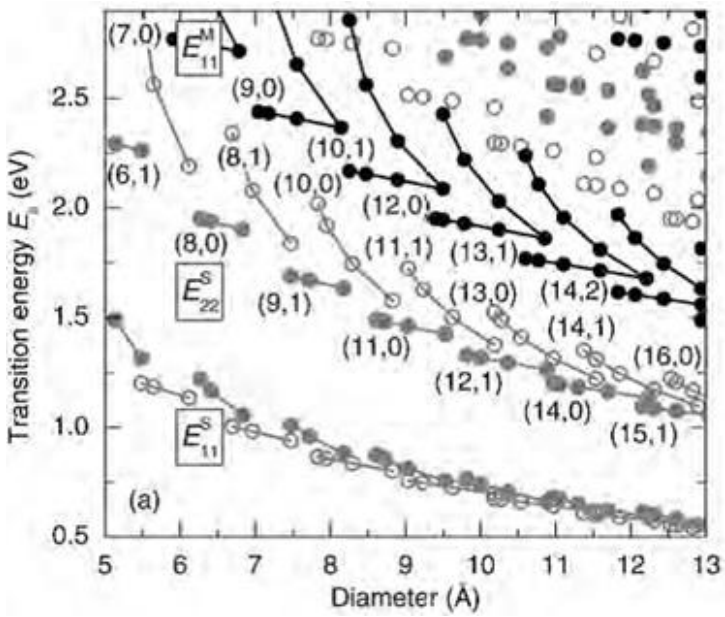

Figure 1-13*. A Kataura plot, adapted from [1-55]. The grey open and closed circles represent E_{11} and E_{22} transitions in semiconducting SWNTs, while the black filled circles represent the E_{11} transitions in metallic SWNTs*

REFERENCES

[1-1]. https://www.rt.com/business/208539-germany-cut-coal-power/
[1-2]. http://mediterranean.panda.org/?213311/Permanent-removal-of-toxic-pollution-permits-must-follow-EU-carbon-market-fix#
[1-3]. http://worldmaritimenews.com/archives/170940/clia-nabu-cruise-ranking-not-scientifically-accurate/
[1-4]. http://www.brisbanetimes.com.au/queensland/queensland-failing-to-regulate-air-pollution-environment-lawyers-20160421-goc7dc.html
[1-5]. http://thecityfix.com/blog/choking-on-smog/
[1-6]. http://www.bbc.com/news/world-asia-china-35351597
[1-7]. http://www.renewableenergyworld.com/index/tech.1.leftinheritedbottom_standard.html
[1-8]. http://www.green-e.org/learn_re_why.shtml
[1-9]. www.iea.org/t&c/
[1-10]. www.eia.gov/forecasts/ieo
[1-11]. https://www.carbonbrief.org/cop22-key-outcomes-agreed-at-un-climate-talks-in-marrakech
[1-12]. http://unfccc.int/meetings/marrakech_nov_2016/items/10045.php
[1-13]. "Solar Energy Perspectives: Executive Summary". International Energy Agency. 2011. Archived from the original (PDF) on 3 December 2011
[1-14]. https://en.wikipedia.org/wiki/Organic_solar_cell
[1-15]. https://www.sciencedaily.com/releases/2009/04/090409151444.htm
[1-16]. http://solarte.de/en/
[1-17]. Green M. A., Emery K., Hishikawa Y., Warta W., and Dunlop E. D. (2014) Solar cell efficiency tables (Version 45), Prog. Photovolt: Res. Appl., 23, 1–9.
[1-18]. Espinosa, Nieves, et al. "A life cycle analysis of polymer solar cell modules prepared using roll-to-roll methods under ambient conditions." Solar Energy Materials and Solar Cells 95.5 (2011): 1293-1302.
[1-19]. Askari Mohammad Bagher. Comparison of Organic Solar Cells and Inorganic Solar Cells. International Journal of Renewable and Sustainable Energy. Vol. 3, No. 3, 2014, pp. 53-58.
[1-20]. Zaumseil, Jana. "Single-walled carbon nanotube networks for flexible and printed electronics." Semiconductor Science and Technology 30.7 (2015): 074001.
[1-21]. Kearns D.; Calvin M. (1958). "Photovoltaic Effect and Photoconductivity in Laminated Organic Systems". J. Chem. Phys. 29 (4): 950–951.
[1-22]. Tang C.W. (1986). "Two-layer organic photovoltaic cell". Appl. Phys. Lett. 48 (2): 183–185.
[1-23]. S.E. Shaheen, C.J. Brabec, N.S. Sariciftci 2.5% Efficient organic plastic solar cells, Appl Phys Lett, 78 (2001), pp. 841–843.
[1-24]. https://thetuzaro.wordpress.com/2015/04/25/on-the-importance-of-spectral-match-when-characterising-organic-solar-cells/
[1-25]. Scharber, Markus Clark, and Niyazi Serdar Sariciftci. "Efficiency of bulk-heterojunction organic solar cells." Progress in polymer science 38.12 (2013): 1929-1940.
[1-26]. Liu L, Shi Y, Yang Y, (2001) SolvationInduced Morphology Effects on the Performance of PolymerBased Photovoltaic Devices Adv Funct Mater 11:420–424.

[1-27]. Shrotriya V, Li G, Yao Y, Moriarty T, Emery K, Yang Y, (2006) Accurate Measurement and Characterization of Organic Solar Cells Adv Funct Mter 16(15): 2016–2023.
[1-28]. Zhou, Nanjia, and Antonio Facchetti. "Charge Transport and Recombination in Organic Solar Cells (OSCs)." Organic and Hybrid Solar Cells. Springer International Publishing, 2014. 19-52.
[1-29]. Fraga Domínguez, Isabel, Andreas Distler, and Larry Lüer. "Stability of Organic Solar Cells: The Influence of Nanostructured Carbon Materials." Advanced Energy Materials (2016).
[1-30]. Mihailetchi, Valentin D., et al. "Charge transport and photocurrent generation in poly (3-hexylthiophene): methanofullerene bulk-heterojunction solar cells." Advanced Functional Materials 16.5 (2006): 699-708.
[1-31]. Miranda PB, Moses D, Heeger AJ, (2001) Ultrafast Photogeneration of Charged Polarons in Conjugated Polymers Phys Rev B 64: 81201.
[1-32]. Mayer AC, Scully SR, Hardin BE, Rowell MW, McGehee MD, (2007) PolymerBased Solar Cells Mater Today 10: 28–33.
[1-33]. Deibel, Carsten, et al. "Energetics of excited states in the conjugated polymer poly (3-hexylthiophene)." Physical Review B 81.8 (2010): 085202.
[1-34]. Clarke TM, Durrant J, (2010) Charge Photogeneration in Organic Solar Cells Chem. Rev. 110:6736–6767.
[1-35]. Nunzi JM, (2002) Organic Photovoltaic Materials and Devices C R Physique 3: 523.
[1-36]. H. Huang, J. Huang (eds.), Organic and Hybrid Solar Cells, Springer International Publishing Switzerland 2014, p5.
[1-37]. Laquai, Frédéric, et al. "Charge carrier transport and photogeneration in P3HT: PCBM photovoltaic blends." Macromolecular rapid communications 36.11 (2015): 1001-1025.
[1-38]. Arkhipov VI, Heremans P, Bassler B, (2003) Why Is Exciton Dissociation So Efficient at the Interface Between a Conjugated Polymer and an Electron Acceptor Appl Phys Lett 82: 4605.
[1-39]. Deibel, Carsten, Thomas Strobel, and Vladimir Dyakonov. "Origin of the efficient polaron-pair dissociation in polymer-fullerene blends." Physical review letters 103.3 (2009): 036402.
[1-40]. Groves, Chris. "Suppression of geminate charge recombination in organic photovoltaic devices with a cascaded energy heterojunction." Energy & Environmental Science 6.5 (2013): 1546-1551.
[1-41]. Groves, Chris. "Developing understanding of organic photovoltaic devices: kinetic Monte Carlo models of geminate and non-geminate recombination, charge transport and charge extraction." Energy & Environmental Science 6.11 (2013): 3202-3217.
[1-42]. Deibel, Carsten, and Vladimir Dyakonov. "Polymer-fullerene bulk heterojunction solar cells." Reports on Progress in Physics 73.9 (2010): 096401.
[1-43]. Langevin, Paul. "Recombinaison et mobilites des ions dans les gaz." Ann. Chim. Phys 28.433 (1903): 122.
[1-44]. Brabec, Christoph J., et al. "Origin of the open circuit voltage of plastic solar cells." Advanced Functional Materials 11.5 (2001): 374-380.
[1-45]. Wetzelaer, Gert-Jan AH, et al. "Quantifying bimolecular recombination in organic solar cells in steady state." Advanced Energy Materials 3.9 (2013): 1130-1134.

[1-46]. Karuthedath, Safakath, et al. "The effect of oxygen induced degradation on charge carrier dynamics in P3HT: PCBM and Si-PCPDTBT: PCBM thin films and solar cells." Journal of Materials Chemistry A 3.7 (2015): 3399-3408.
[1-47]. https://en.wikipedia.org/wiki/Carbon_nanotube#cite_note-65
[1-48]. M. S. Dresselhaus; et al. (1995). "Physics of Carbon Nanotubes". Carbon. 33 (7): 883–891.
[1-49]. Zamolo, Valeria Anna, Ester Vazquez, and Maurizio Prato. "Carbon Nanotubes: Synthesis, Structure, Functionalization, and Characterization." Polyarenes II. Springer International Publishing, 2013. 65-109.
[1-50]. Lu, X.; Chen, Z. (2005). "Curved Pi-Conjugation, Aromaticity, and the Related Chemistry of Small Fullerenes (C60) and Single-Walled Carbon Nanotubes". Chemical Reviews. 105 (10): 3643–3696.
[1-51]. Dresselhaus, M. S., et al. "Electronic, thermal and mechanical properties of carbon nanotubes." Philosophical Transactions of the Royal Society of London A: Mathematical, Physical and Engineering Sciences 362.1823 (2004): 2065-2098.
[1-52]. Hong, Seunghun, and Sung Myung. "A flexible approach to mobility." Nature Nanotech 2 (2007): 207-208.
[1-53]. Wang, Feng, et al. "The optical resonances in carbon nanotubes arise from excitons." Science 308.5723 (2005): 838-841.
[1-54]. H. Kataura; et al. (1999). "Optical Properties of Single-Wall Carbon Nanotubes" (PDF). Synthetic Metals. 103 (1–3): 2555–2558.
[1-55]. Maultzsch, Janina, and Christian Thomsen. "Characterization of carbon nanotubes by optical spectroscopy." Carbon Nanotube Devices: Properties, Modeling, Integration and Applications (2008): 125-180.

2 SAMPLE PREPARATION AND CHARACTERIZATION

2.1 Synthesis of Chirality Sorted SWNTs

For studying the excited state dynamics of SWNTs, samples enriched in (6,5) and (7,5) chiralities, respectively, are prepared. The sample preparation procedure partially based on ref. [2-1--3], where certain chiralities are extracted from the chirality mixed source material by wrapping specific tubes with polyfluorenes. CoMoCAT SG-65, the source material, is bought from SouthWest Nanotechnologies. To achieve (6,5) rich samples, 15mg poly[(9,9-di-n- octylfluorenyl-2,7-diyl)-alt-co-(6,6′-{2,2′-bipyridine})] abbreviated as PFO- BPy (from American Dye Source) mixed with 7.5mg nanotube source material and diluted in 15mL toluene in a vial. The mixture then is sonicated for eight continuous hours in an ultrasonic disrupter equipped with a microtip (Branson Sonifier II W-450). The microtip has a diameter of 5mm. The vial containing the mixture is always surrounded with ice to keep the temperature low in order not to lose the mixture by means of evaporation, also not to destroy the microtip. The setup is presented in Figure 2-1a, b. Settings for the sonicator for this specific step are always: duty cycle at 50% and output control at four. Output control is the power settings, which determines the amplitude of the tip movement and degree of the ultrasonic activity in the liquid. After that, eight small vials are filled with certain amount of the mixture, and loaded into a benchtop centrifuge (Heraeus Biofuge 15), which is run for three minutes at 140000 rpm. The resulting supernatants then is passed through an ester membrane filter with pore size of 0.01μm (Millipore VCWP02500) under vacuum (Figure 2-1c). Afterwards the nanotube contained filter is cut into four pieces and dissolved in acetone filled Petri dishes, which brought the SWNT films to float on the surface and the dissolved membrane to sink to the bottom. Next, the SWNT films are taken out from the Petri dishes by thin glass rods and placed into other ones with fresh acetones. 10 minutes later, the SWNT films are transferred into a fresh acetone contained small glass vial. After 5 minutes, the acetone is sucked out by pipettes, and the remaining acetone is dried out with nitrogen gas. In the last step, 200μL chlorobenzene is added into the SWNT film collected glass vial, and sonicated in a cup sonicator for two hours at a duty cycle of 100% and output control of 4, to redistribute the SWNTs (Figure 2-1d). The three-minute centrifuging step is repeated if solid materials are observed after sonication in the ultrasonic bath.

All the procedures above are the same for the preparation of the (7,5) rich sample, except that

27mg poly(9,9-di-n-octylfluorenyl-2,7-diyl) abbreviated as PFO from Sigma-Aldrich is used instead of PFO-BPy. The final films for our spectroscopic study purpose are made by drop casting a 100μL fraction of the suspensions (Figure 2-1e) on cleaned glasses (in ultrasonic bath with acetone, isopropanol and distilled water in sequential order, 10 minutes each). The optical densities of the films are found to be 0.7 and 0.8 for (6,5) and (7,5) films, respectively.

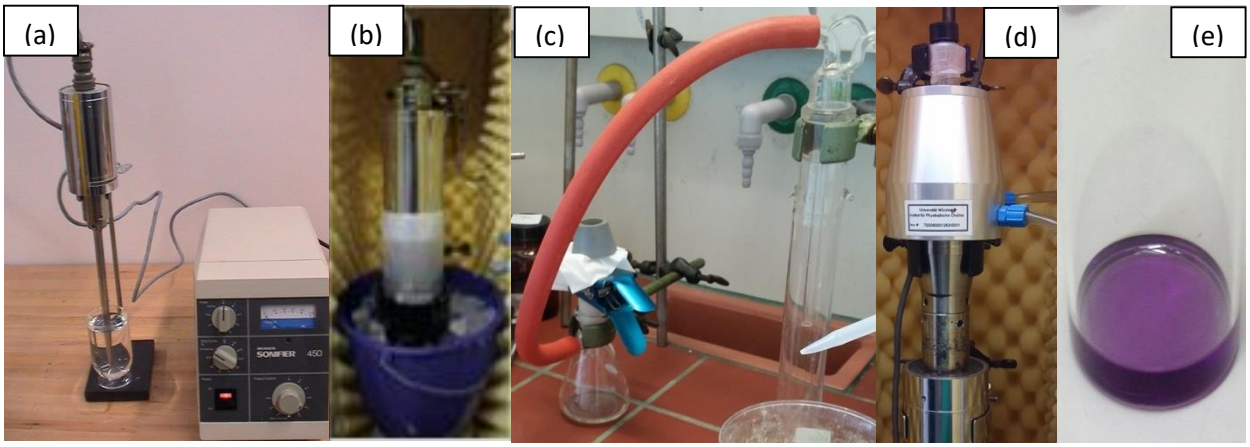

Figure 2-1. Chirality sorted SWNT sample preparation. (a) Branson Sonifier II W-450-- Ultrasonic disrupter with a microtip. (b) Polymer/nanotube mixture under sonication in an ice bath; (c) Filtering setup; (d) Cup sonicator; (e) Final product

2.2 Transient Absorption Spectroscopy

2.2.1 Experimental Setup

Femtosecond Transient Absorption (TA) Spectroscopy. TA spectroscopy is also called pump-probe spectroscopy, and requires two pulsed laser sources, one for pumping (exciting) the sample and the other for probing the excited sample. A picture of our TA spectroscopy setup and its simplified schematics is shown in Figure 2-2. A 775nm pulsed beam provided by a Clark-MXR (CPA-2101) system (driven at 1 kHz by a regenerative amplifier) is doubled by a beam splitter. One of them is transformed into a white light (477-1600nm) via a super continuum generator (SCG—a sapphire plate) to form probe beam, and is focused onto the sample with a spot size of about 130μm. The other beam is transformed into pump beam centred at 387nm via a second harmonic generator (SHG). The probe beam is directed to a prism spectrometer (Entwicklungsbüro Stresing GmbH) equipped with a double channel CCD array (2 X 256 pixels, VIS-enhanced

InGaAs, Hamamatsu Photonics Inc.) after passing through the sample. A reference signal is also made by taking part of the probe beam directly to the spectrometer before it reaching the sample, which is to reduce the noise induced by the laser fluctuation. The pump beam, after being chopped at 500Hz with a mechanical chopper, is guided to the sample to coincide with the probe beam with a spot size of 260um, and is blocked afterwards. A mechanical translation stage constructed in the pathway of the pump beam controls the optical delay between pump and probe up to 500ps with a 150fs time resolution. A notch filter removes the residual fundamental 775 nm beam. In the system, neutral density filters adjust the intensities of both pump and probe beams, and 2/λ plates adjust their polarization angles. A custom-built Python program based on open source packages (Matplotlib, PyQt4, Scipy, Pyserial etc.) handles the data acquisition and data analysis, including global spectral modelling of the TA spectra.

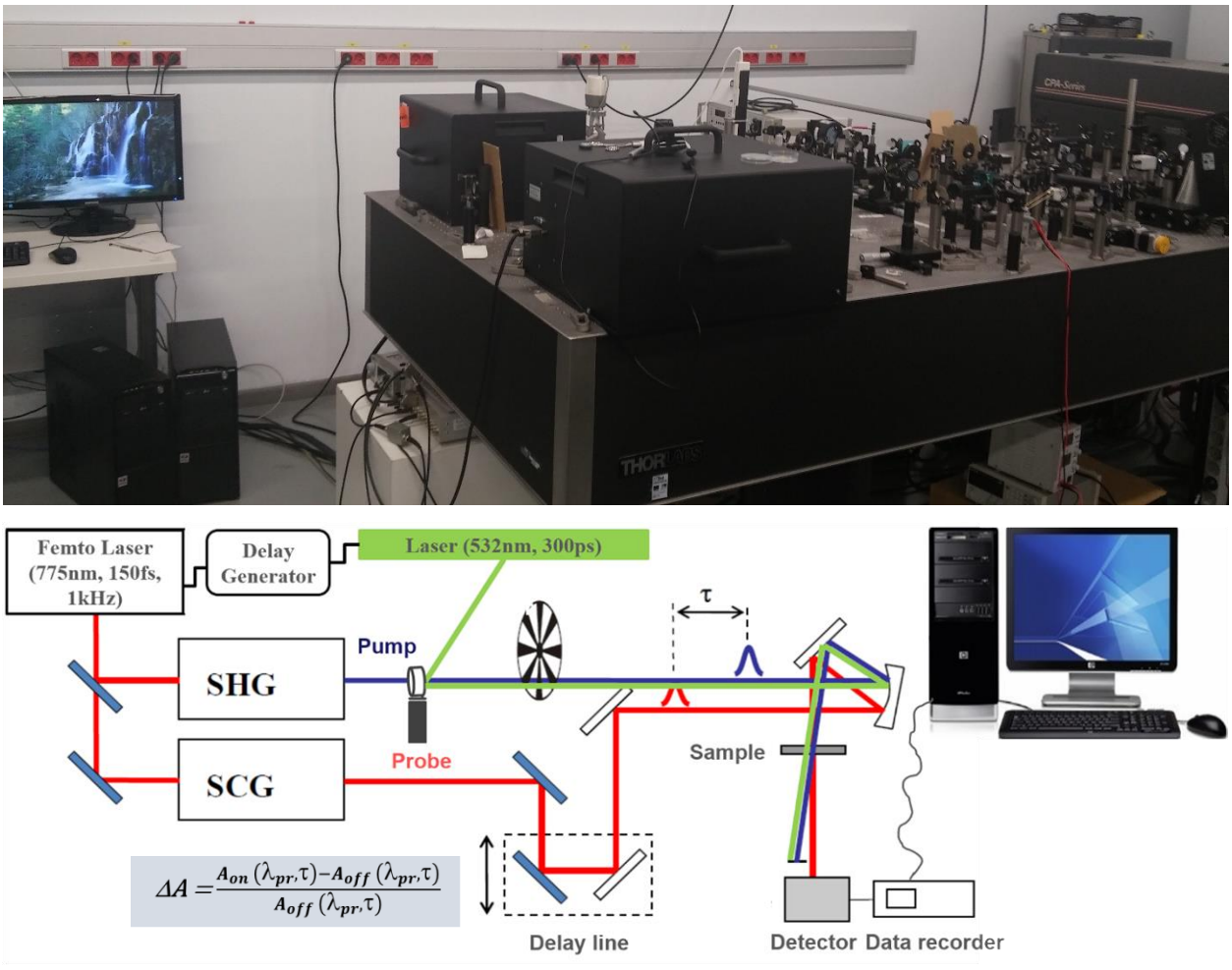

Figure 2-2. Picture of our femtosecond TA spectroscopy setup (upper), and its simple schematics (lower)

2.2.2 Fundamentals of TA Spectroscopy

In TA spectroscopy, a chopped pump beam with a single wavelength/photon energy excites the sample from ground state to its excited state. After a variable delay time τ, a weak broadband probe beam probes the excited sample (e.g. Figure 2-3a). The transmittance of the probe beam T is defined as

$$T = \frac{I_{tr}(\lambda)}{I_0(\lambda)} = [I_0(\lambda) - I_A(\lambda) - I_R(\lambda)]/I_0(\lambda) \quad (2\text{-}1)$$

where I_0 is the intensity before the sample, I_{tr} is the intensity after the sample, I_R is the intensity lost by reflection at the sample and I_A is the intensity absorbed by the sample. All these quantities depend on the probing wavelength λ. In order to isolate the small changes on T introduced by the pump beam, the differential transmission is measured as

$$\Delta T/T = \frac{\mathrm{T}(pump\ on) - \mathrm{T}(pump\ off)}{\mathrm{T}(pump\ off)} \quad (2\text{-}2)$$

$$\Delta \mathrm{A} = -\ln\left(\frac{\Delta T}{T} + 1\right) \quad (2\text{-}3)$$

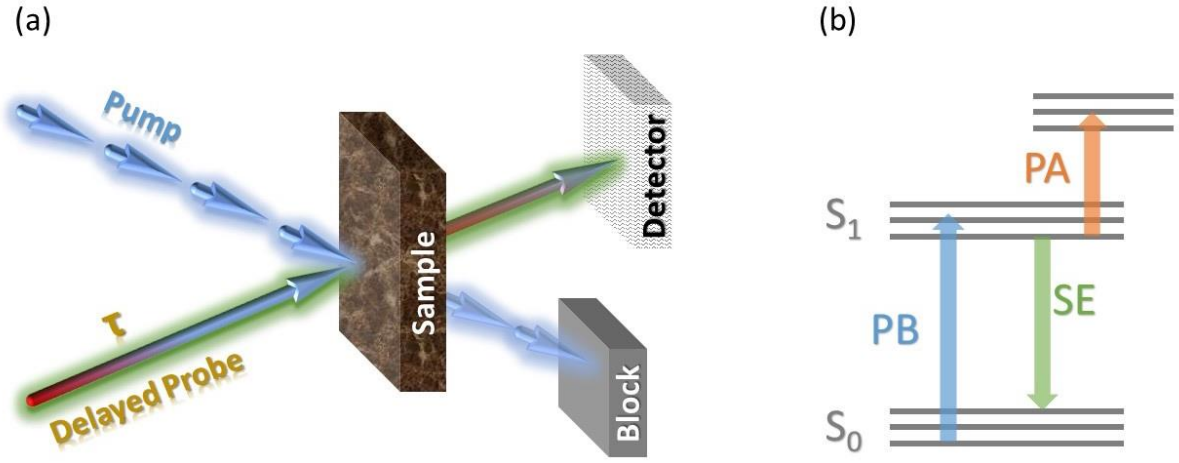

Figure 2-3. (a) Fundamentals of the TA spectroscopy: pump beam excites the sample at one single wavelength and after a delay time (τ) a broadband probe beam probes the sample. (b) A simple level scheme of an organic material: ground state (S_0), excited state (S_1), and observable TA signals: photobleach (PB), photoinduced absorption (PA) and stimulated emission (SE)

The sign of the $\Delta T/T$ signal gives important first insight into photophysical processes. A positive $\Delta T/T$ band means that at the respective probing wavelength, the pump pulse causes increased transmission. This can either be due to stimulated emission (SE), a clear optical probe for states that are strongly optically coupled to the ground state, or it can be caused by a reduction of ground state absorption, the so-called transient photobleach (PB), an important general indicator of the

presence of excited states in a certain absorber. The assignment of a positive band to either PB or SE can be done by comparison with the absorption spectrum and the fluorescence spectrum, respectively. Negative $\Delta T/T$ bands, on the other hand, are caused by photoinduced absorption (PA) due to an optical transition from an excited state, created by the pump pulse, to a higher energetic state. Even such excited states that are not coupled to the ground state, e.g. triplet states, can have strong PA bands. TA spectroscopy is therefore a powerful tool to study "bright" and "dark" photoexcited states in the same measurement. A simple level scheme of an organic semiconductor and the observable TA signals are exampled in Figure 2-3b. Each $\Delta T/T$ can be converted into differential absorption (ΔA) signal via eq. (2-3), which then can be expressed as a product of wavelength dependent absorption cross section ($\sigma(\lambda)$), time dependent absorbance concentration ($c(t)$) and sample thickness (d), according to Lambert-Beer's law:

$$\Delta A = \sigma(\lambda) \cdot c(t) \cdot d \tag{2-4}$$

A typical three-dimensional TA spectroscopy data obtained in our setup is illustrated in Figure 2-4, where vertical axis represents the probe energies, horizontal axis indicates the pump-probe delays and the direction perpendicular to those two axes denotes the intensity of the ΔA signal.

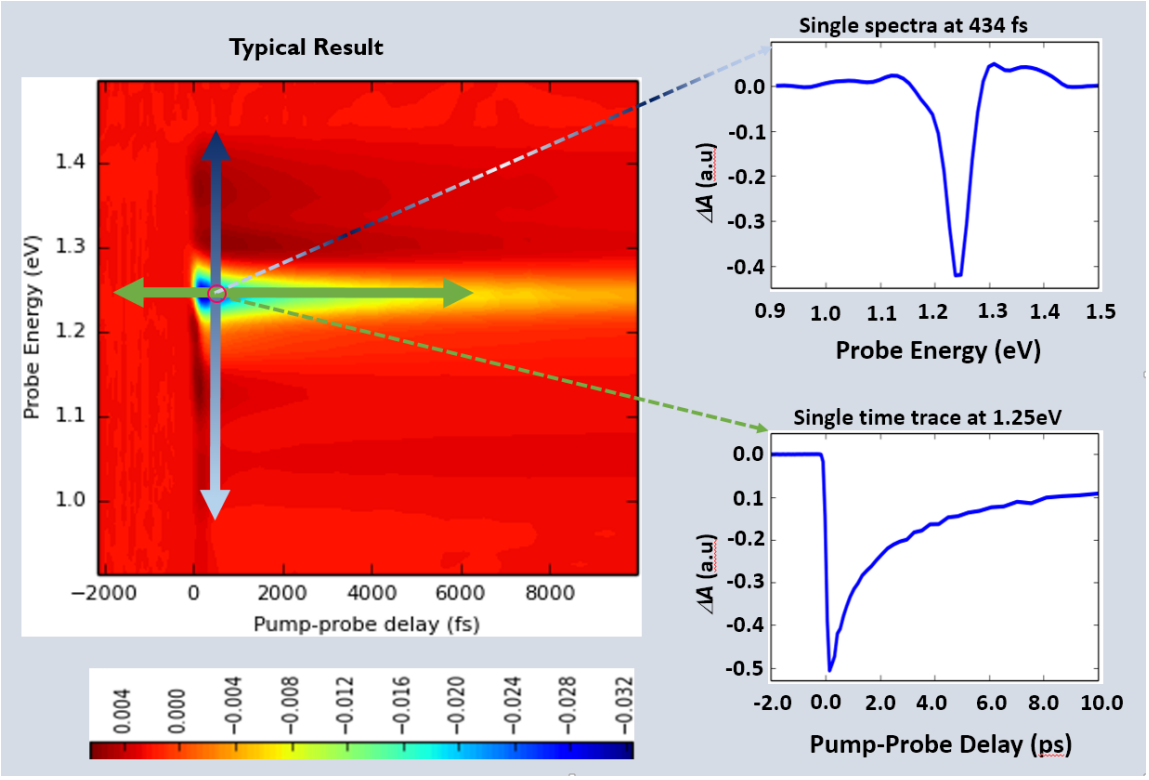

Figure 2-4. A typical TA spectra of (6,5) rich SWNT sample. The colors represent strength of the TA signal as indicated in the scale bar at the bottom. The two subplots on the right are a single spectrum and a single time trace extracted from a single point on the right

2.2.3 Global Spectral Modelling

Spectral shapes of the ΔA bands arisen from different species are usually strongly superposed in organic materials, which makes it difficult to label the various excited states and identify the corresponding dynamics of each individual species as well as the interactions among them. As an example, the TA spectra of a (6,5) rich SWNT sample recorded at various pump-probe delays is given in Figure 2-5. The spectral region from 0.9eV to 1.25eV is a superposition of several PA and PB bands from (6,5), (8,4), (10,3) and (7,5) tubes.

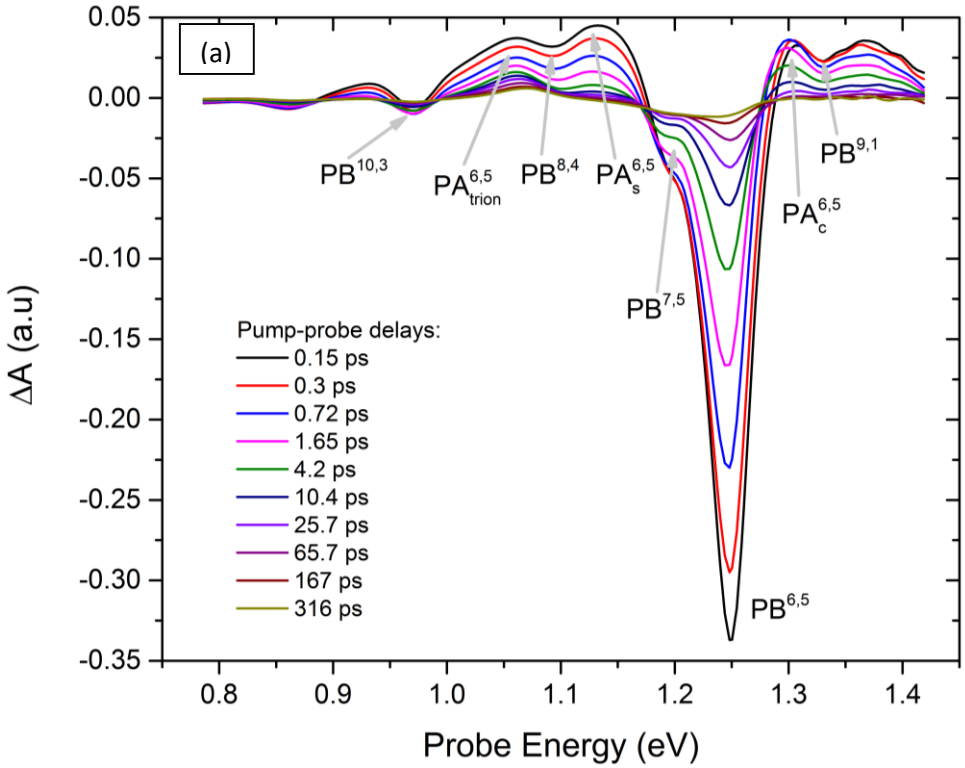

Figure 2-5. Absolute TA spectra of a (6,5) rich SWNT sample recorded at pump-probe delays from 150 femtoseconds to 316 microseconds

To this end, we need to perform matrix decomposition technique--global spectral modelling—directly on the measured TA spectra, to separate the congested spectral shapes and achieve more precise excited state concentration dynamics.

In the global spectral modelling, the measured TA spectra at all pump-probe delays can be expressed as the sum of i superposed PA (ΔA) and PB ($-\Delta A$) bands based on Lambert-Beer law,

$$\Delta A(t,\lambda) = \sum_i \sigma(\lambda)_i \cdot c(t)_i \cdot d \qquad (2\text{-}5)$$

By applying eq. (2-5) the measured TA spectra is reproduced by selecting appropriate spectral

shape functions for $\sigma(\lambda)_i$ and obtaining the time-resolved concentrations $c(t)_i$ by non-linear optimization. The sample thickness d is constant, and σ is usually a Gaussian or Lorentzian function. The main features of the bands like their center position, spectral width and spectral weight ratios will be clarified from other techniques such as ground state absorption spectroscopy, steady state and time dependent photoluminescence (PL) spectroscopy etc. If there are excited states that are not possible to pin down through our available experimental techniques, values from literature will be taken. Once the fit parameters are gathered, the probe energy and time dependent model will be set to run on the whole TA spectra under nonlinear optimization. If the simulation successfully reproduces the measured TA spectra, time dependent concentrations for all excited states (included in the model) will be obtained. Being applied directly to the measured data without any decay rate assumption, this method can be superior compared to the conventional global kinetic modelling [2-4, 2-5]; because in the latter, the TA spectra is simulated with sequential rate constants, which is not always applicable for the data measured on organic materials, since forward and backward parallel transitions are very common.

2.3 OSC Fabrication and J-V Characterization

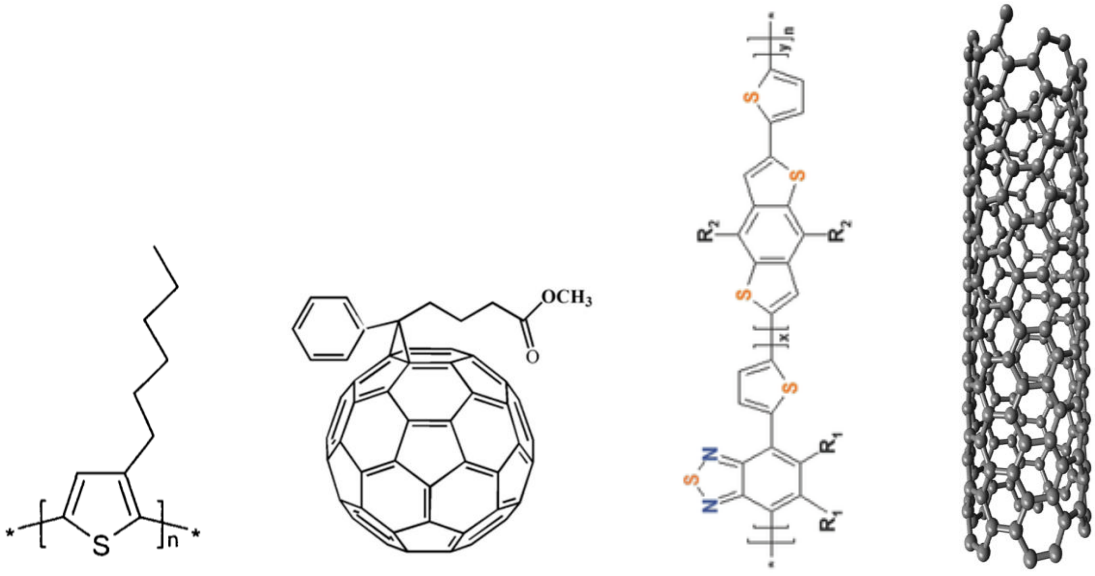

Figure 2-6. Chemical structure of P3HT, PCBM, OPV48 and SWNT, respectively

Materials. OSC device fabrication is done at Belectric OPV GmbH in Nurnberg, Germany, and all necessary materials (except the SWNTs) together with the device making recipes are provided. The materials namely are: regioregular poly (3-hexyl thiophene) [RR-P3HT]—the donor material; PBTZT-stat-BDTT-8 (OPV48)—a more efficient donor material [2-6], to see whether the SWNTs behave the same; [6,6]-phenyl-C61-butyric acid methyl ester (PCBM)—the acceptor material; poly ethylene imine (PEI)—the hole blocking material; polystyrene sulfonate (PEDOT:PSS)—the electron blocking material; methylnaphthalene—the additive for morphological improvement, and ITO/Glass—the substrate. For the nanotube, the (6,5) chirality enriched SWNTs produced at Prof. Tobias Hertel's lab is used. Chamical structures of the active layer materials are given in Figure 2-6.

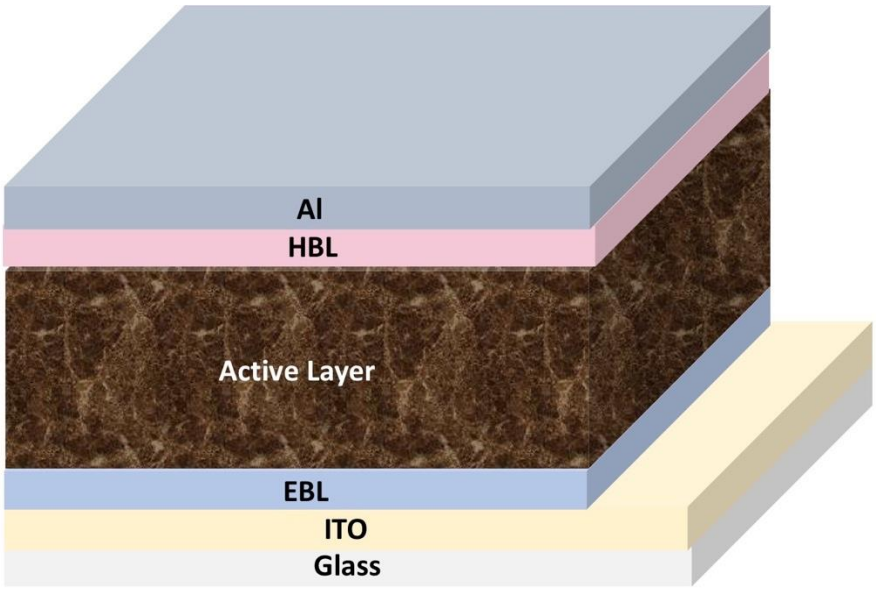

Figure 2-7. Device Configuration

OSC Devices Fabrication. The device configuration is shown in Figure 2-7. The preparation procedure starts from preparing several ITO coated glass substrates. The ITO/Glass substrates are first patterned via an intensive ultraviolet laser light as shown in Figure 2-8a. Second, the patterned ITO substrates are cleaned in acetone, isopropyl alcohol (IPA) and distilled water in sequential order in an ultrasonic bath, each for 10 minutes, and dried up in compressed nitrogen flow. The solution for the active layer of P3HT:PCBM devices is prepared by sonicating the suspension of (6, 5) chirality enriched SWNTs (dispersed in chlorobenzene, 0.03mg/mL) for 45 minutes at 80 °C, and adding 225μL of it plus 25μL methylnaphthalene to a 250uL P3HT:PCBM (1:08) solution

(prepared in xylene with a concentration of 30mg/mL). On the other hand, the solutions for the OPV48:PCBM devices are made by adding 250uL of the SWNTs dispersion to a 250 μL OPV48:PCBM (1:1.5) solution (prepared in chlorobenzene with a concentration of 50mg/mL). All solutions are sonicated for 15 minutes prior to coating.

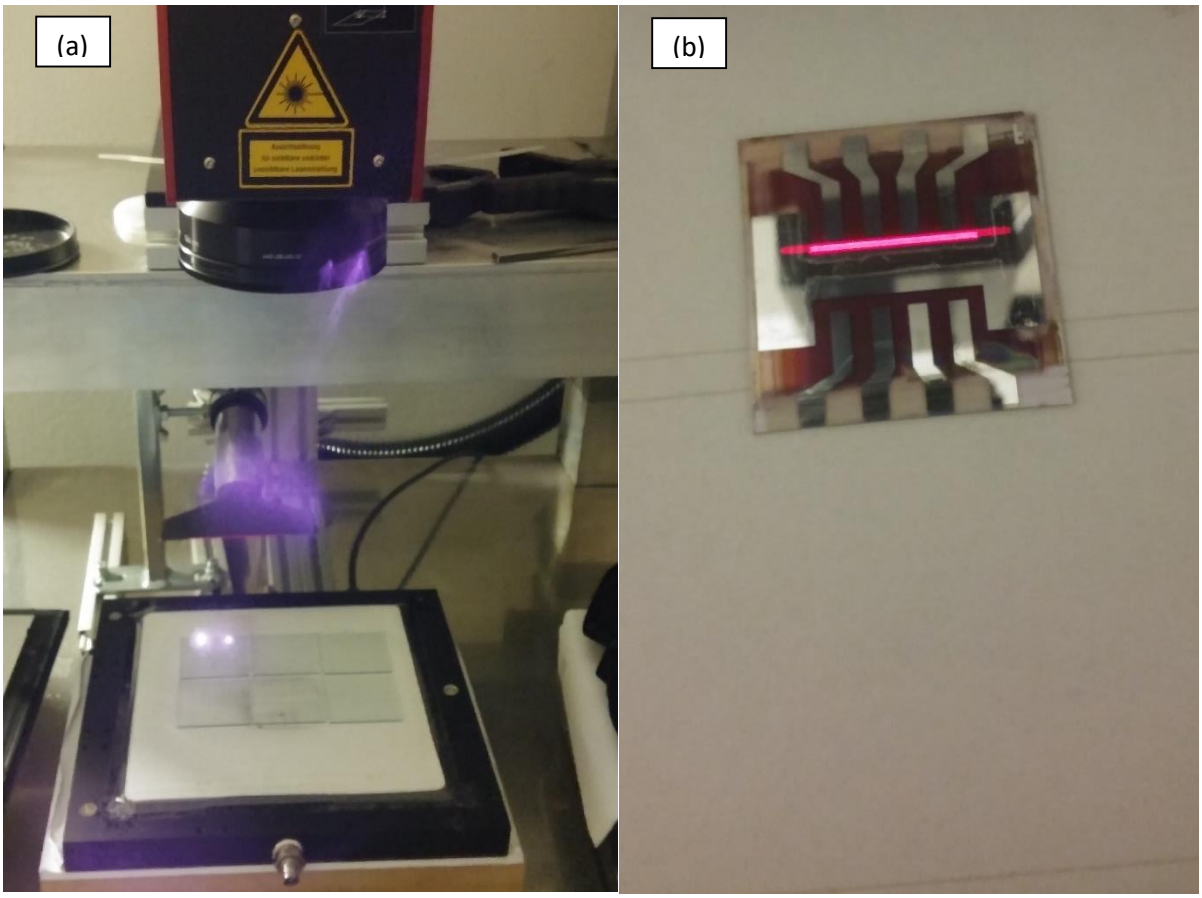

Figure 2-8. (a) Patterning the ITO/Glass substrates with an ultraviolet laser light. (b) Patterning the actual device area by removing the electrodes with laser light

Once the substrates and solutions are ready, the hole blocking layer (EBL, to prevent electrons to cost holes at anode), active layer, and electron blocking layer (HBL, to prevent holes to cost electrons at cathode) are coated subsequently onto the ITO substrate by the doctor blading technique. In doctor blading, a blade, set on top of the substrate with certain vertical offset, moves in a constant speed spreading the solution to form a thin sheet; the offset and the speed of the blade decides the thickness of the film. After coating, the absorption spectra of the active layer is recorded with an Ocean Optics USB2000+, to verify the thickness using Lambert-Beer's law (eq.

1-3). The Measurement of the actual film thickness is conducted by a mechanical profilometry using Dektak Alpha-Setup 500.

Before evaporating the top electrode in the next step with a predesigned finger-like mask, the samples are annealed on a hotplate for five minutes at 140°C in a glovebox. The top electrode, Ag, has a final thickness of 300nm for all devices. To make sure the charges that are collected at the electrodes are primarily the charge carriers generated from a known area under the electrodes, the edges of the electrodes are removed by the laser ablation, see figure 2-8b, and the cell areas for most of the devices are 7.5mm^2. Finally, the devices are encapsulated with a commercial glue to avoid degradation. The reference devices are made from the same P3HT:PCBM and OPV48:PCBM solutions (without SWNTs) with the exact same fabrication processes.

Standard J-V Characterization. The standard current-voltage (J-V) characterization is taken place (at BELECTRIC OPV, Nuremburg, Germany) in a glove box equipped with a solar simulator (Newport 91160) and a Keithley 2400 source measure unit integrated with a Keithley 7001 Multiplexer system in the dark and under simulated 1 sun condition. Eight devices each with eight cells are measured at once. The J-V characteristics of the encapsulated devices chosen for further characterization by TA spectroscopy and transient optoelectronic techniques are measured again in our setup at IMDEA Nanoscience (Madrid, Spain); where a white light LED is used as illumination source, and a Keithley 6487 Picoammeter/Voltage source unit controlled by a custom-built Python program is used for recording the J-V characteristics. Of course, the white LED can't produce the complete AM 1.5G like sunlight spectrum, but, the light intensity is adjusted so that a similar V_{oc} is obtained in the P3HT:PCBM reference device as measured under simulated 1 sun condition at BELECTRIC OPV; and any significant differences on the fill factor, short circuit current, open circuit current is observed.

2.4 Transient Optoelectronic Measurements

2.4.1 Transient Photovoltage (TPV)

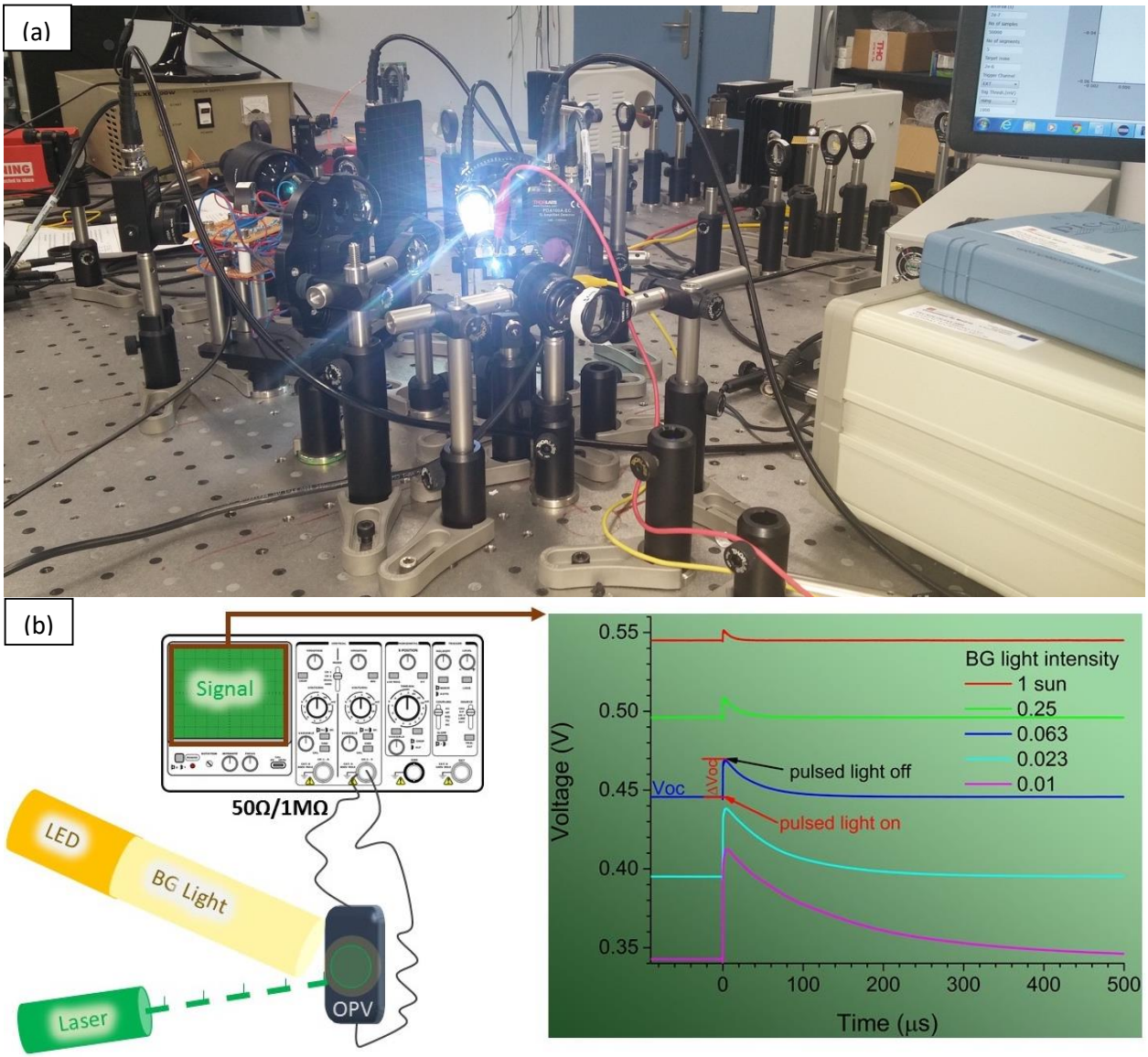

Figure 2-9. (a) Picture of our TPV/TPC setup; (b) its simple schematics with the exemplified TPV signal

TPV is a technique that monitors the decay kinetics of the open circuit voltage following a light pulse, and can provide information about the recombination dynamics of the charge carriers in a working device. The advantage of this technique compared to the other techniques such as charge-extraction-by-linearly-increasing-voltage (CELIV) and microsecond TA spectroscopy is that it can extract electrical parameters from a complete device in real working conditions under various

sunlight intensities. In contrast, CELIV uses a high-power laser to obtain such information which is far away from the working condition of a normal OSC device. The signal in microsecond TA spectroscopy is very noisy (the signal is in the range of 10-4 -10-7 OD). Signal averaging for noise reduction is very time consuming, and the long continues BG illumination could also damage or degrade the device when high light intensity is implemented.

Basic principle of the TPV technique is that the device stays at open circuit condition by being connected to the high impedance input of an Oscilloscope (1MΩ in our case). Thereafter, a continuous background (BG) white light illuminates the device's active area to generate steady state charge carrier density creating an open circuit voltage (Voc). Weak light pulses shines on top of the BG white light to generate a small amount of additional charge carriers (causing an increase of the open circuit voltage, ΔVoc), which will decay in time after the light pulse. An oscilloscope records both the constant Voc and the time dependent ΔVoc. In our setup, a white LED for the BG light source and a 532nm laser for the pulsed light is applied. A picture of our actual experimental setup and its simple schematics as well as the schematics of the corresponding signal are illustrated in Figure 2-9.

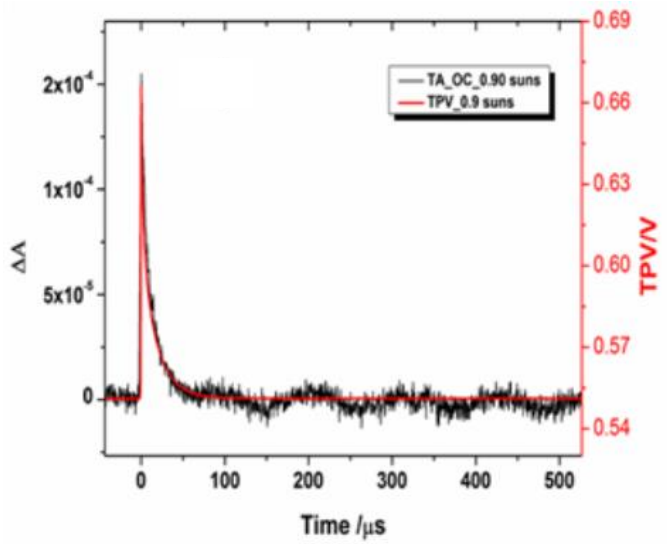

Figure 2-10. Comparison of charge dynamics obtained with TPV and TA Spectroscopy, adapted from ref. [2-5]

It has been proven that the decay kinetics of ΔVoc signal measured with TPV matches perfectly with the decay kinetics of charge density obtained with microsecond TA spectroscopy [2-6], which was also confirmed in our group (Figure 2-10) [2-5]. Note, care must be taken ($\Delta Voc << Voc$) so

that the dynamics of ΔVoc should exhibit a mono-exponential decay. Therefore, the dynamics of the ΔVoc reveals the dynamics of the perturbed charge density (Δn), which can then be used to obtain the Langevin recombination rate described in eq. (1-7), after acquiring the total charge density,

$$\frac{d\Delta V_{oc}}{dt} \propto \frac{d\Delta n}{dt} = -k_{\Delta n}\,\Delta n = -\frac{\Delta n}{\tau_{\Delta n}} \tag{2-6}$$

where ΔVoc is the voltage perturbed by the pulsed light, t is the time, Δn is the photogenerated charge carrier density created by the pulsed light, $k_{\Delta n}$ and $\tau_{\Delta n}$ are the decay rate the lifetime of the Δn, respectively. Charge density dependence of the $\tau_{\Delta n}$ can be determined by conducting the TPV measurement at various BG light intensities. Such dependence has been reported to be exponential with the Voc,

$$\tau_{\Delta V_{oc}} = \tau_{\Delta V_{oc}(0)} \exp(-\beta V_{oc}) \tag{2-7}$$

where $\tau_{\Delta V_{oc}(0)}$ is the lifetime of the perturbed charge carrier density at $Voc = 0$, and β is a constant.

2.4.2 Transient Photocurrent (TPC)

TPC is a technique that can provide information about carrier extraction in the device at short circuit—a complimentary technique to TPV. All the experimental conditions, even the setup, are the same as for TPV, except the device will be connected to the oscilloscope's 50Ω input channel instead of 1MΩ. Assuming that the inner resistance of the device is much higher than the input resistance R_I of the oscilloscope, the measured voltage drop U_{osc} is proportional to the electrical current I and can be obtained by Ohm's Law, $I = U_{osc}/R_I$. TPC, thus, traces the extraction dynamics of the charge carriers induced by the pulsed light at the two electrodes at short circuit condition. Combining the results from TPV and TPC, one can quantify the bimolecular charge recombination purely from these electrical studies.

Figure 2-11 shows a typical TPC signal. According to the general rate equation,

$$\frac{dn}{dt} = k_b(n)n(t)^2 \tag{2-8}$$

The bimolecular charge recombination is characterized by the time-resolved charge density in the device, $n(t)$, and the bimolecular recombination coefficient, $k_b(n)$. The stationary charge density in the device can be obtained by finding the proportionality constant between the differential

change in photovoltage (TPV), dV_{oc}, and the change in the total charge dQ_{tot}, namely, the capacitance:

$$C(V_{oc}) = dQ_{tot}/dV_{oc} \tag{2-9}$$

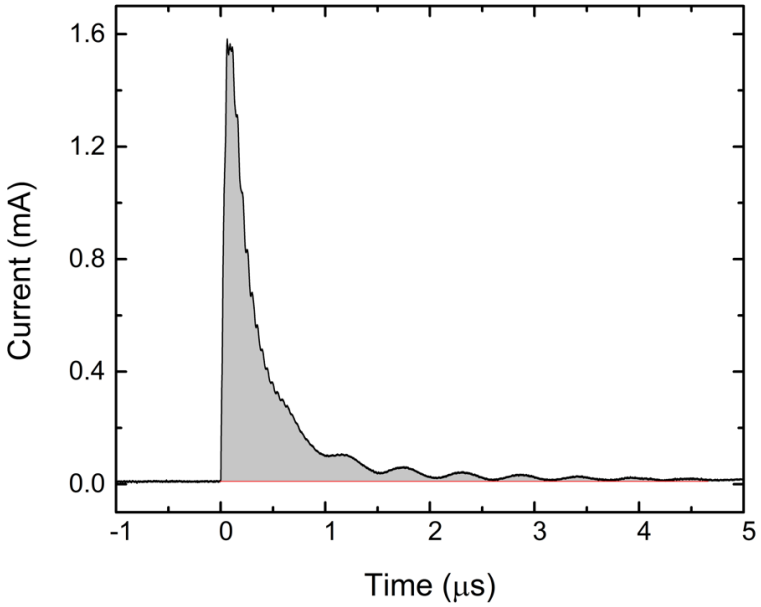

Figure 2-11. TPC signal. The grey area gives the total moving charges (ΔQ) generated by the pulsed light impinging at time zero

In the case of bulk capacitance of a semiconductor, C is dependent on the voltage. If recombination can be neglected under short circuit condition, then the extracted charge ΔQ_{extr} in the TPC experiment will be equal to the additional charge in the bulk of the semiconductor ΔQ_{bulk} in the TPV experiment. Thus, by performing TPV and TPC experiments at a set of BG illumination intensities, the $C(V_{oc})$ can be found. Then, the eq. (2-9) can be restated as,

$$C(V_{oc}) \approx \Delta Q_{bulk}/\Delta V_{oc} \approx \Delta Q_{extr}/\Delta V_{oc} \tag{2-10}$$

Integrating the $C(V_{oc})$ versus the measured V_{oc} yields the total photoinduced charge inside the bulk,

$$Q_{bulk} = \int_0^{V_{oc}} C(V)\, dV = n_0 \exp(\gamma V_{oc}) \tag{2-11}$$

The stationary charge density n as a function of V_{oc} can be obtained by inserting the device active area A, its thickness d, and the elementary charge e:

$$n = Q_{bulk}/Aed \tag{2-12}$$

The n is reported to be exponentially dependent on V_{oc} [2-6],

$$n = n_0 \exp(\gamma V_{oc}) \tag{2-13}$$

where n_0 is the charge density at $Voc = 0$ and γ is a constant. Then the total carrier lifetime (τ) and bimolecular recombination coefficient (k_b) can be calculated [2-7, 2-8] as,

$$\tau = \tau_{\Delta V_{oc}}(-S + 1) \quad (2\text{-}14)$$

$$k_b = (\tau n)^{-1} \quad (2\text{-}15)$$

where $S = \beta/\lambda$, which can be directly obtained from a $\tau_{\Delta V_{oc}}$ vs. n plot.

2.4.3 Microsecond TA Spectroscopy

Measuring the charge carrier density in a working device is crucial to do a full device characterization. It can be attained from the TPV/TPC measurements as already discussed; yet, they have some limitations depending on the device. Unlike TA spectroscopy, TPV/TPC is sensitive to only the mobile charge carriers irrespective of their location but insensitive to the trapped ones. TA spectroscopy can detect both mobile and trapped carrier at specific phases. Moreover, the carrier loss in the device at short circuit due to recombination should be very small, and the carrier generation in the device must be independent of electric field. Some devices can meet such requirements but others do not. Therefore, we have also integrated a microsecond TA spectroscopy setup into our TPV/TPC experimental system to be able to study any types of devices. In this case, we do not use the TPC to obtain the stationary charge density n, but use the Lambert-Beer's law in differential form,

$$\Delta A(\lambda) = A(\lambda)^{ST} - A(\lambda)^{BG} = \sigma(\lambda).n.d \quad (2\text{-}16)$$

Where $A(\lambda)^{ST}$ and $A(\lambda)^{BG}$ are the absorbance at probe wavelength λ by the stationary state and background carriers (dark), respectively, and the $\sigma(\lambda)$ is the absorption cross-section for the charged states at this probe wavelength. In practice, these two states are attained by placing a slowly rotating chopper in the BG light path and assuring that towards the end of the on/off periods, constant absorption values are obtained. In our case, a chopper frequency of 20Hz is found to be adequate. Since we only subtract absorbance values for the two conditions, stationary and background, a much higher sensitivity is reached in contrast to measuring the TA dynamics.

Figure 2-12 shows the TPV/TPC setup combined with microsecond TA spectroscopy, where the same BG white light but chopped at 41Hz excites the sample continuously for 24.3ms and switches of for another 24.3ms. A steady 970nm weak probe light monitors the difference in absorption of the charge band of the sample when the BG light goes off and on. Then we calculate the steady

state charge density of the devices through the Beer-Lambert law as described in previous subsection. All the experimental conditions are same for TPV/TPC and TA Spectroscopy. Both BG and pulsed light intensities are controlled by the neutral density filters.

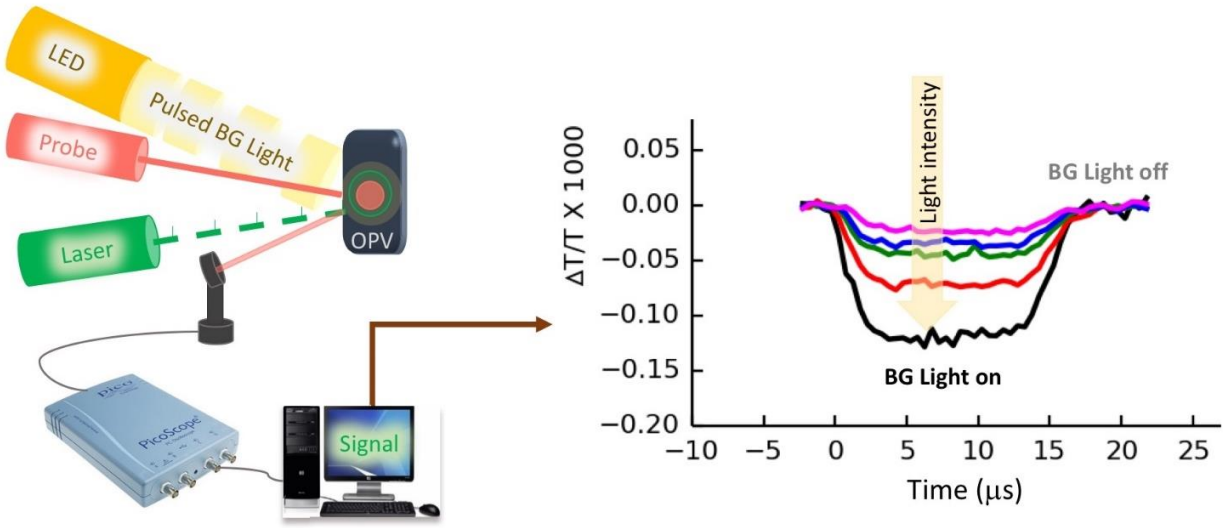

Figure 2-12. Basic Schematics of the microsecond TA spectroscopy integrated into the TPV/TPC setup, and the corresponding TA signal

In our measurement, the TPV/TPC signals are recorded with a fast oscilloscope (LeCroy, waveSurfer, 44MXs-B, 400MHz). The microsecond TA signal is detected via an amplified InGaAs photodiode (Thorlabs PDA20CS-ES) and recorded with a Picoscope 6424 controlled by a custom-built Python program.

2.5 Field Effect Transistor

2.5.1 Basic Principles

FET is a device, constructed by placing a thin layer of dielectric, semiconducting and metallic materials on a supporting substrate, that controls the shape and electrical conductivity of a channel formed between the dielectric and the semiconductor. It consists of three main terminals namely source, drain and gate regardless of the device type. Based on the location of the terminals, the FET devices can be categorized as top-gate, bottom-gate, top-contact (drain and source) or bottom-contact. Depending on the type of the semiconducting material (hole or electron rich), the devices can also be identified as p-type (hole conducting) or n-type (electron conducting) or bipolar (both

hole and electron conducting).When the device is biased at drain-source, charge carriers flow from the source to drain through an electrical channel formed between the semiconducting and dielectric materials. The electrical channel cannot be formed if there are not enough free charge carriers or they are very randomly distributed. In the latter case, the gate with applied voltage comes into play in building the channel by attracting the free charge carriers towards the dielectric. The sign and the amplitude of the voltage applied on the gate modulates the width of the channel, and thereby also the magnitude of the electrical flow.

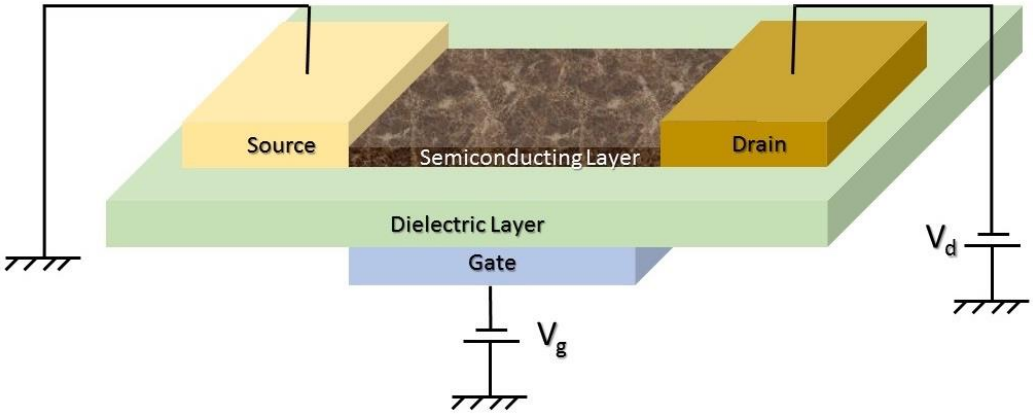

Figure 2-13. Schematic representation of a bottom-gate FET

In a standard FET device characterization procedure, the voltage between drain-source and between gate-source will be modulated, and the current will be measured at all three terminals. The current at the drain can be can be described by square-law model [2-10],

$$I_d = \frac{\mu W_{ch} C_g}{L}\left[(V_g - V_T)V_d - \frac{V_d^2}{2}\right] \tag{5-1}$$

When V_d exceeds $(V_g - V_T)$, the drain current saturates and can be calculated as

$$I_d = \frac{\mu W_{ch} C_g}{2L}(V_g - V_T)^2 \tag{5-6}$$

Then, the carrier mobility can be calculated at linear regime as

$$\mu_{lin} = \frac{\partial \mathrm{I}_{d,lin}}{\partial V_g}\frac{\mathrm{L}}{W_{ch} C_g V_d} \tag{5-7}$$

At saturation regime, the threshold voltage VT can be obtained from $\sqrt{\mathrm{I}_{d,sat}}$ vs. V_g plot [2-11], then the mobility can be expressed as

$$\mu_{sat} = \left(\frac{\partial\sqrt{\mathrm{I}_{d,sat}}}{\partial V_g}\right)^2 \frac{2\mathrm{L}}{W_{ch} C_g} \tag{5-8}$$

All the important information mentioned above can be extracted from two measurement curves so-called output and transfer characteristic.

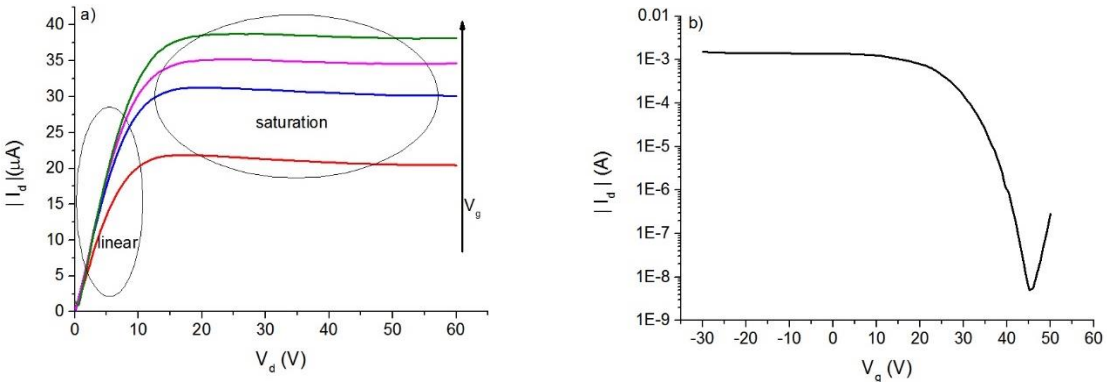

Figure 2-14. Examples of FET output (a) and transfer (b) curves.

2.5.2 FET Fabrication and Characterization

Fabrication. Many pre-patterned commercial (Fraunhofer) substrates, made from n-doped silicon (gate), 100nm SiO_2 (dielectric) and 30nm gold (drain and source electrodes) with different channel width and length as displayed in Figure 2-13, are cleaned with acetone, isopropanol and distilled water in a sequential order in an ultrasonic bath each for 10 minutes, and dried in a stream of N_2 afterwards. Thereafter they are cleaned in UV ozone for 20 minutes. After that, the semiconducting SWNT suspension is spin-coated on the cleaned substrate at a rotating speed of 1000 rpm for 30 seconds in glove box. Covering the whole substrate surface is ensured for each device. The devices are then annealed at 90 C for 15 minutes as a final step to remove the excess solvent. Note, the fabricated devices have either (6,5) or (7,5) rich SWNTs with various concentrations as their semiconducting layer, which is due to the aim of studying the concentration and chirality dependent charge carrier mobility in the SWNT bundles.

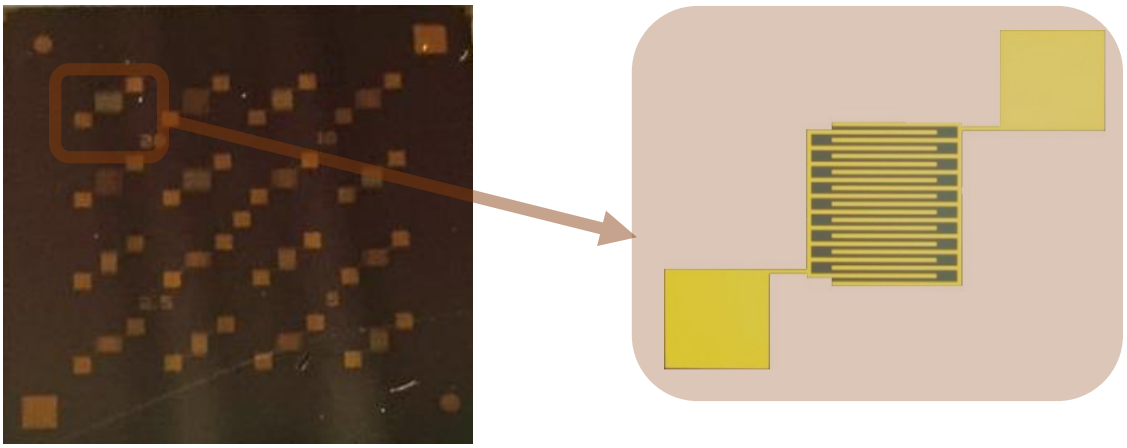

Figure 2-15. Picture of a pre-patterned Si/SiO_2 Fraunhofer substrate. The figure on the right is a 200 times magnification of the indicated part on the left

Characterization. For characterization of SWNTs, a standard absorption spectroscopy is performed on the nanotube suspension contained cuvette with 1mm light path, via Varian Cary 5000 UV-VIS-NIR spectrometer. X-ray photoelectron spectroscopy (XPS) is applied to measure the density of states (DOS) of the SWNTs. Surface characterization of the FETs is carried out with an Agilent 5500 SPM atomic force microscopy (AFM) in tapping-mode by taking topography images. Electrical characterization of devices is conducted with an Agilent B2902A semiconductor parameter analyzer combined with Keithley 4200 and a probe station in a glove box filled with nitrogen at room temperature, keeping the humidity and oxygen level below 2.5ppm and 0.5ppm, respectively. Connection of devices with the source measure units is made at the probe station by moving the needle-like three micro-positioners (Figure 2-14). Then, the current at drain electrode is measured as a function of drain and gate voltage to construct the output and transfer curves of the FETs. Afterwards, the carrier mobility and threshold voltage of the devices are extracted from those two curves.

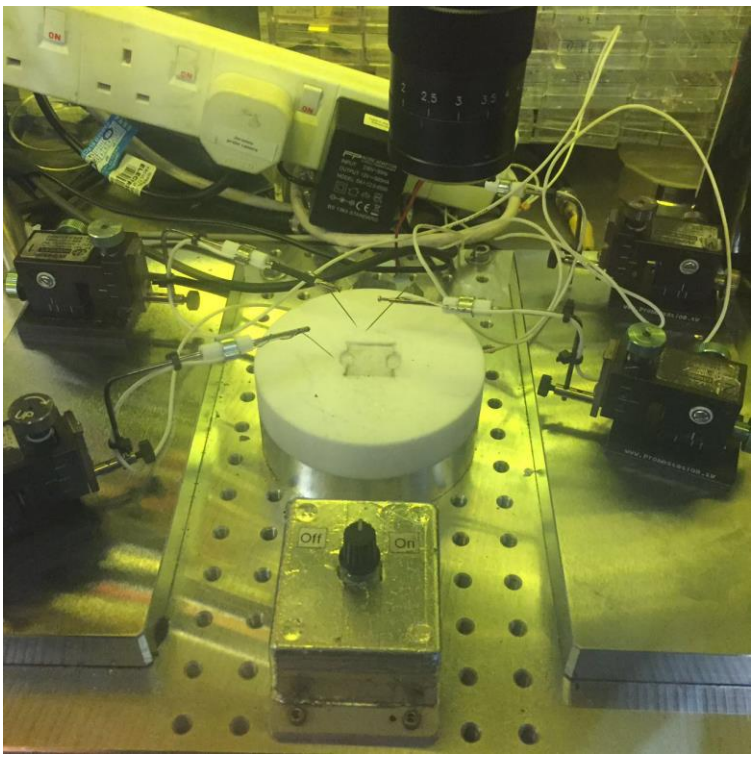

Figure 2-16. *Probe station equipped with three magnetic-base micro-positioners. Each positioner has a needle-like contact connected directly to the source measure unit. The connection between the needle and FET terminal is always monitored with an optical microscope, and once the position of the needle on the electrode is confirmed, the connection between them is secured by tightening the mechanically with the nub located on top of the micro-positioner*

REFERENCES

[2-1]. Nish, A.; Hwang, J.-Y.; Doig, J.; Nicholas, R. J. Highly Selective Dispersion of Single-Walled Carbon Nanotubes Using Aromatic Polymers. Nat. Nanotechnol. 2007, 2, 640−646.

[2-2]. Chen, F.; Wang, B.; Chen, Y.; Li, L.-J. Toward the Extraction of Single Species of Single-Walled Carbon Nanotubes Using Fluorene- Based Polymers. Nano Lett. 2007, 7, 3013−3017.

[2-3]. Ozawa, H.; Ide, N.; Fujigaya, T.; Niidome, Y.; Nakashima, N. One-Pot Separation of Highly Enriched (6, 5)-Single-Walled Carbon Nanotubes Using a Fluorene-Based Copolymer. Chem. Lett. 2011, 40, 239−241.

[2-4]. Karuthedath, Safakath. "Tracing degradation effects in organic solar cells." (2015).

[2-5]. van Stokkum, Ivo HM, Delmar S. Larsen, and Rienk van Grondelle. "Global and target analysis of time-resolved spectra." Biochimica et Biophysica Acta (BBA)-Bioenergetics 1657.2 (2004): 82-104.

[2-6]. Berny, Stephane, et al. "Solar Trees: First Large-Scale Demonstration of Fully Solution Coated, Semitransparent, Flexible Organic Photovoltaic Modules." Advanced Science (2015).

[2-7]. Shuttle, C. G., et al. "Experimental determination of the rate law for charge carrier decay in a polythiophene: Fullerene solar cell." Applied Physics Letters 92.9 (2008): 3311.

[2-8]. Shuttle, C. G., et al. "Experimental determination of the rate law for charge carrier decay in a polythiophene: Fullerene solar cell." Applied Physics Letters 92.9 (2008): 3311.

[2-9]. Maurano, Andrea, et al. "Transient optoelectronic analysis of charge carrier losses in a selenophene/fullerene blend solar cell." The Journal of Physical Chemistry C 115.13 (2011): 5947-5957.

[2-10]. Hong, D., et al. "Electrical modeling of thin-film transistors." *Critical Reviews in Solid State and Materials Sciences* 33.2 (2008): 101-132.

[2-11]. Kymissis, Ioannis. "Modeling and Characterization." *Organic Field Effect Transistors: Theory, Fabrication and Characterization*. Boston, MA: Springer US, 2009. 1-28.

3 CHIRALITY DEPENDENT EXCITED STATE DYNAMICS OF SWNTS

(This part has been published on The Journal of Physical Chemistry C)

Abudulimu, Abasi, et al. "Chirality Specific Triplet Exciton Dynamics in Highly Enriched (6, 5) and (7, 5) Carbon Nanotube Networks." The Journal of Physical Chemistry C 120.35 (2016): 19778-19784.

3.1 Introduction

Excitons of SWNTs, formed by coulomb interactions, are very stable even at room temperature, owing to their large binding energies ranging from 200meV to nearly 1eV [3-1--3] and govern the optical properties of the SWNTs [3-4]. Possessing the strong excitonic properties and fast charge transport features [3-5, 3-6], SWNTs have become one of the most attractive class of materials in the field of research due to the interest on their use in a wide range of potential applications such as field-effect transistors [3-7], biosensors [3-8], light-emitting diodes (LED) [3-9] and solar cells [3-10]. Maximizing the advantage of SWNTs in any of the devices and realizing new possible applications requires a better understanding of their unique optical and electronic properties. Huge progress has been made in the last two decades from measuring the exciton size [3-11], exciton binding energies [3-1--3] and addressing various non-radiative relaxation pathways of excited states [3-12--16]. Great efforts in sample preparation have also been made to solve some of the fundamental problems like separating metallic tubes from semiconducting ones [3-17--19]. As the presence of metallic SWNTs could otherwise could have detrimental effect on performance of a photovoltaic device [3-20], leading to fast exciton quenching and increased shunting pathways [3-21]. Thanks to the impressive development in the recent sorting techniques that allowed to study exciton photophysics in SWNTs without excessive spectral congestion [3-22--25], and overcome the one of the obstacles to better understand the intrinsic properties of SWNTs.

Raman scattering [3-26--29], absorption [3-30--37], fluorescence [3-38-- 44] and transient absorption spectroscopies [3-12, 3-45--59] have provided insight into various aspects of the electronic structure of various SWNT species. A number of great work have been done to answer the low photoluminescence quantum yield in SWNTs [3-60--62]. Magnetic field applied photoluminescence [3-12--15] and absorption spectroscopy [3-16] studies showed the existence of structure and excitonic level dependent dark states in SWNTs lying 8.5-130meV lower than the bright excitons in the E11 region and 9.0meV higher in E22 region, for instance, claiming them to be the photoluminescence quantum yield limiting factors in SWNTs. Transient absorption spectroscopy studies, on the other hand, have attributed a great value on identifying the various photoexcited states in SWNTs. Luer et. al. measured the exciton size of around 2 nm [3-17] and reported direct evidence for ultrafast energy transfer between aggregated tubes of different chirality in the lowest excitonic states with an upper limit of 10 fs following the ultrafast relaxation

of the higher excited states [3-57]. Yuma et. al. [3-63] and others [3-49, 3-64] reported the signatures of biexcitons, four particle excitations, on SWNTs locating 50-130meV below the E11 transition, which could be initiated through excitation of two closely spaced excitons or/and collision of the two [3-49, 3-63, 3-65]. Photo-generation of free charge carriers and trions (charged excitons) in neutral as well as in doped SWNTs samples have been reported number of times [3-45, 3-56, 3-63, 3-66--84]. The former causes a spectral shift of the main photo bleach due to the Stark effect and gives rise to a photoinduced absorption band on the higher energy side of the bleach [3-67, 3-74, 3-85, 3-86]; while the latter produces a photoinduced absorption band which is usually about 180meV lower than the E11 transition [3-63, 3-73, 3-74, 3-81, 3-84]. In addition to those, the existence of another dark state, triplet has also been addressed in SWNTs [3-15, 3-87--89]. Stich et. al. [3-90], recently, reported a possible triplet formation yield of 5-32% with a life time of 30 microseconds via spin sensitive fluorescence spectroscopy. However, the precise location of triplet states on the electronic structure of the SWNTs is still unknown.

Although great efforts have been made on investigating the optical and electronic properties, a comprehensive description about the generation of all possible photoexcited states following the excitation, their respective yields, the possible relaxation pathways as well as the corresponding life times is still elusive. Since such a description is crucial to fully understand the optical properties of SWNT and so is to their potential applications. Here we report, along with the calculation of chirality concentration, the ultrafast transient absorption spectroscopy study results on two SWNT films enriched in (6,5) and (7,5) chiralities, respectively, probing from 850 nm to 1600 nm at different excitation intensities. In addition to the qualitative probes of various photo-excited states, we analyze their concentration dynamics by performing a global spectral modelling on complete TA spectra.

3.2 Determination of Chirality Concentration

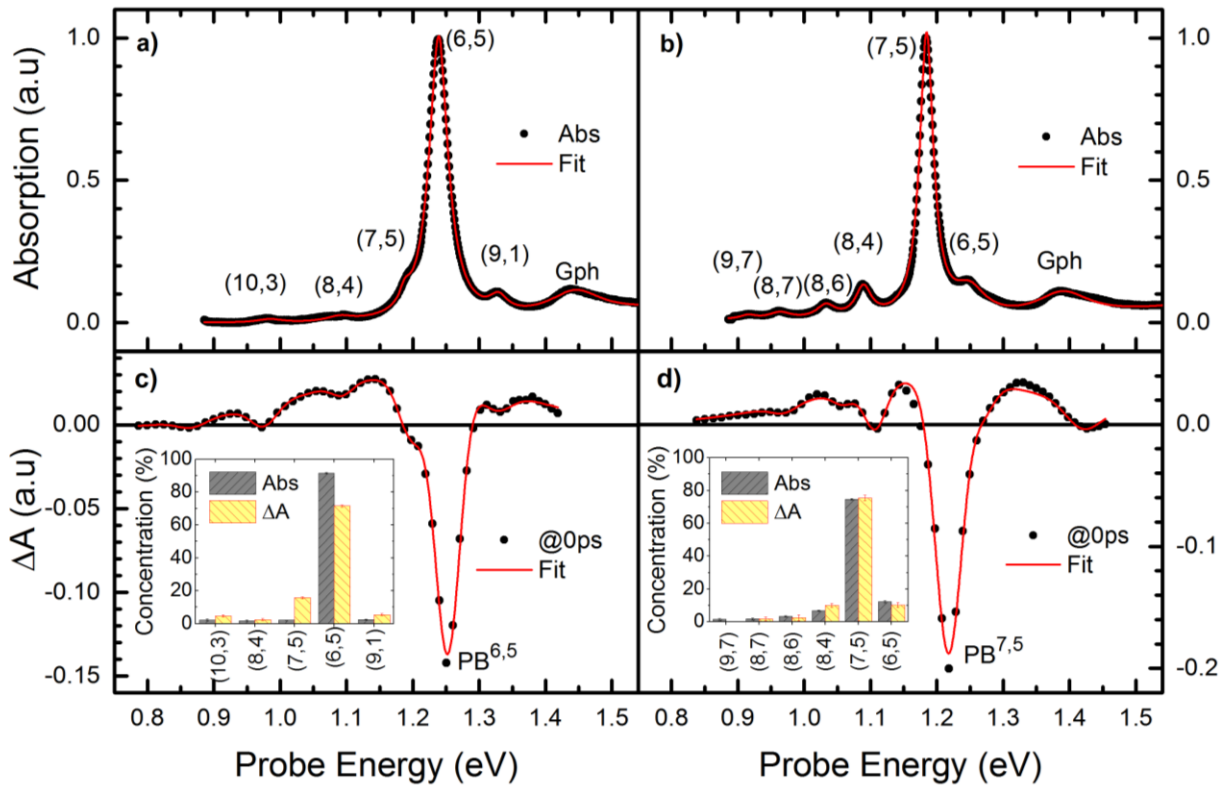

Figure 3-1. Ground state absorption (upper panel) and TA spectra (lower panel) of (6,5) (left column) and (7,5) (right column) rich SWNT samples. The insets in c) and d) are the SWNT chirality distributions in the respective samples, where Abs refers to ground state absorption spectra, ΔA refers to transient absorption spectra and the numbers with brackets in the horizontal axes refer to chirality indices.

Figure 3-1 shows ground state absorption ("abs", upper row) for the (6,5) rich and the (7,5) rich sample (left and right column, respectively). The absorption spectra are dominated by intense bands at 1.24 and 1.19 eV referring to the E11 excitonic transition of the (6,5) and (7,5) tubes (dots in Fig. 1a and b, respectively). Weaker maxima are associated with the presence of other chiralities. We have calculated the relative spectral weights of SWNT chiralities in our samples by fitting the ground state absorption spectra by a superposition of Gaussians and taking the area under each individual absorption peak to represent the relative nanotube chirality concentration in the sample [3-91]. In order to properly fit the absorption spectra (red curves), we had to include several chiralities, as indicated in the figure. The linewidths of (6,5) and (7,5) E11 excitonic bands were determined from (6,5) and (7,5) rich samples (which are 34meV and 24meV, respectively), and fixed in the model, while the other linewidths are limited between 20meV and 40meV. Figure 3-1

(red curves in upper row) shows the fit results of ground state absorption spectra, as well as the corresponding relative chirality concentration in both (6,5) and (7,5) rich samples (gray bars in panel c and d). Assuming a chirality-independent absorption cross section, we found that the (6,5) rich sample contains about 92% of (6,5) tubes and about 2% of (7,5) tubes, while the (7,5) rich sample contains about 78% (7,5) tubes and about 7% of (6,5) tubes. Most of the remaining tubes are on the lower energy side in both samples, so that it is in principle possible to observe energy and charge transfer processes.

The wavelength of the pump pulse in these experiments was 387 nm (3.204 eV). It essentially excites the free carrier background of all chiralities leading to a chirality unspecific generation of electron-hole pairs. Within the duration of the pump pulse, the electron hole pairs are expected to be localized to form bound excitons [3-58, 3-64, 3-92--94] causing a transient photobleach (PB) of the corresponding absorption features. To see whether the excited states remain in the most abundant chirality soon after the pump pulse is off, we conducted the spectral fit procedure also on transient absorption spectra of both (6,5) and (7,5) rich samples recorded at 0ps (the time resolution in our system is approximately 150fs). Figure 3-1 (c and d), shows the transient absorption (TA) spectra (dots) and the fit results (lines), as well as the corresponding relative spectral weights of chiralities (yellow bars) in both (6,5) and (7,5) rich samples. Comparing the early time TA spectra with the ground state absorption spectra, we found for both samples that the lower energetic PB features are relatively stronger than the corresponding ground state absorption features, which is rendered in the bar graphs as well, compare yellow shaded and grey shaded bars, respectively. This can either be caused by ultrafast downhill energy transfer in hexagonal aggregates, which has been shown to occur on a 10fs time scale [3-58] and thus during our 150fs pump pulse, or it can be caused by a relatively stronger oscillator strength of the free carrier continuum of the lower energetic tubes compared to the (6,5) tube. In any case, we note that at the end of the 150fs pump pulse, most of the excited states reside on the dominant tubes (on (6,5) tubes in the (6,5) rich sample, and on (7,5) tubes in the (7,5) rich sample). We discard any high-intensity effects as a reason for the observed over-representation of low energy tubes in the TA spectra. Since the pump intensity dependence of that effect is weak and in the opposite direction (see table 3-1 and3- 2). In the TA spectra, the lower energetic PB bands are superposed with a large photoinduced absorption band of opposite sign, which has been assigned to excited state

absorption of the (6,5) or (7,5) singlet excitons, $PA_E^{6,5}$ or $PA_E^{7,5}$ [7-8]. Therefore, we consider the start of our experiment as the photoexcited states of SWNTs characterized by a large excess of singlet excitons on (6,5) or (7,5) tubes in the respective samples.

Table 3-1. Pump intensity dependence of relative spectral weights in the (6,5) rich sample

33 μJ/cm²			**99 μJ/cm²**		**198 μJ/cm²**	
Chirality	**Spectral weight, %**	**Error**	**Spectral weight, %**	**Error**	**Spectral weight, %**	**Error**
(10,3)	4.74E+00	5.69E-01	3.77E+00	9.35E-01	2.99E+00	4.51E-01
(8,4)	2.47E+00	5.79E-01	1.58E+00	5.70E-01	8.46E-01	4.63E-01
(7,5)	1.57E+01	6.60E-01	1.54E+01	7.53E-01	1.55E+01	5.37E-01
(6,5)	7.15E+01	6.82E-01	7.46E+01	1.33E+00	7.72E+01	5.52E-01
(9,1)	5.52E+00	6.69E-01	4.65E+00	6.58E-01	3.54E+00	5.35E-01

Table 3-2. Pump intensity dependence of relative spectral weights in (7,5) rich sample

33 μJ/cm²			**99 μJ/cm²**		**198 μJ/cm²**	
Chirality	**Spectral weight, %**	**Error**	**Spectral weight, %**	**Error**	**Spectral weight, %**	**Error**
(10,3)	1.77E+00	1.28E+00	1.56E+00	1.27E+00	1.14E+00	1.25E+00
(8,4)	2.52E+00	1.84E+00	2.46E+00	1.88E+00	2.26E+00	1.73E+00
(7,5)	9.92E+00	1.23E+00	8.47E+00	1.28E+00	7.41E+00	1.18E+00
(6,5)	7.55E+01	1.59E+00	7.78E+01	3.95E+00	7.83E+01	1.55E+00
(9,1)	1.03E+01	1.60E+00	9.74E+00	2.47E+00	1.09E+01	1.56E+00

3.3 TA Spectroscopy of Chirality Enriched SWNTs

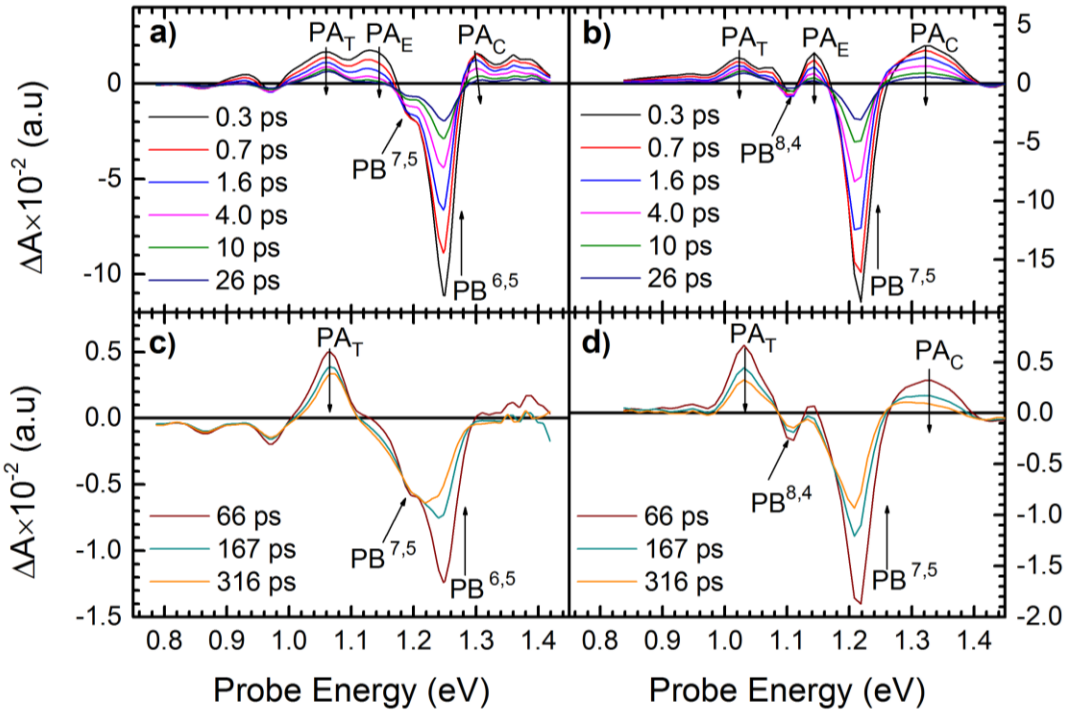

Figure 3-2. Transient absorption spectra of (6,5) rich and (7,5) rich sample (left and right column, respectively) on short and long picosecond time scale (upper and lower row, respectively). Arrows next to PA and PB bands indicate the direction of evolution with increasing pump-probe delay. PB, PA_T, PA_E and PA_C represent the photobleach, photoinduced absorption (PA) of trions, PA of singlet excitons and PA of charges, respectively

In Figure 3-2, we show differential absorption (ΔA) spectra for the (6,5) rich and (7,5) rich samples (left and right columns, respectively) at various pump-probe delay times t, as given in the legend. The dominant spectral features in Figure 3-2 are well-known [3-11, 3-59--60]. Negative ΔA bands are caused by the transient photobleach (PB) of the E11 excitonic transitions of the most abundant chiralities in the sample, as can be shown by the spectral coincidence of the PB bands with the respective ground state absorption bands (see Figure 3-1). Broad positive ΔA bands on the low and high energy side of the main PB are caused by the photoinduced absorption (PA) of singlet excitons and charged states, here referred to as PA_E and PA_C, respectively [109,120]. A relatively sharp PA_T band at 1.065 (Figure 3-2a, c) and at 1.03 eV (Figure 3-2b, d) has been assigned to PA from the trion states in (6,5) and (7,5) tubes, respectively, which can essentially be described as a

charged exciton transitions [3-63, 3-73, 3-76--84]. During the first 25ps (Figure 3-2a, b), the photoexcitation dynamics are characterized by a strong reduction of the (6,5) and (7,5) PB and of PA_E, caused by rapid disappearance of singlet excitons on this time scale, probably mediated by exciton-excitotn annihilation or trap-assisted recombination [3-52].

For pump-probe delays of t > 66ps, (Figure 3-2c and d), most singlet excitons have decayed, as shown by the lack of red-shifted PA_E. The remaining PB should therefore be attributed to excited states other than the singlet excitons. According to the phase space-filling picture [3-95], the photobleach can be interpreted as non-specific probe for the presence of excited states. Given the presence of specific optical probes for charged states (PA_T and PA_C dominating the positive side of the ΔA spectra in Figure 3-2c, d), we can assign at least part of the PB to charged states. Importantly, in Fig 3-2c we find an absolute increase of PB of the (7,5) chirality at a probe energy of 1.2 eV after long times, showing the delayed creation of excited states on this chirality. Since we do not observe the concomitant (7,5) trion band at 1.03 eV (compare with Figure 3-2d where this band is clearly displayed), we conclude that this delayed PB(7,5) is not caused by charged states. It is also confirmed at microsecond time scale, see Figure 3-3. Note that the positive sharp peak on the higher energy side of the main PB at microsecond TA spectra is not clearly seen in the late picosecond TA spectra of both samples, despite there is a broad peak in the case of (7,5) rich sample (compare with Figure 3-2c and d).

We attribute that to charge band of the main tube, which is covered with its own PB, at least partially, in the picosecond time scale. Then reappeared in the longer pump-probe delays when the other excited states decayed and reduced the overall PB, or also the PB shifted from its primary location. It should also be mentioned that in the case of (6,5) rich sample, we also have (9,1) tube. Its PB sits right on top of the charge band of (6,5) tube (see the absorption spectra of (6,5) rich sample, Figure 1a). Whereas, the charge band of (7,5) tubes is free from such an overlap in the (7,5) rich sample. That is one reason that we don't see charge band of (7,5) tubes in (7,5) rich sample, but not of (6,5) tube's in (6,5) rich sample at the end of picosecond TA spectra (see again Figure 3-2a, b). That sharp peak could also be created by stark effect caused from charges around tube. Such an effect produces a first order derivative like shape. Another important fact to note from microsecond TA spectra is that the line width of PB in (6,5) rich sample is much broader

compare to that of (7,5) rich sample. It clearly implies that we have more than one species or interactions to induce the broad PB in (6,5) rich sample.

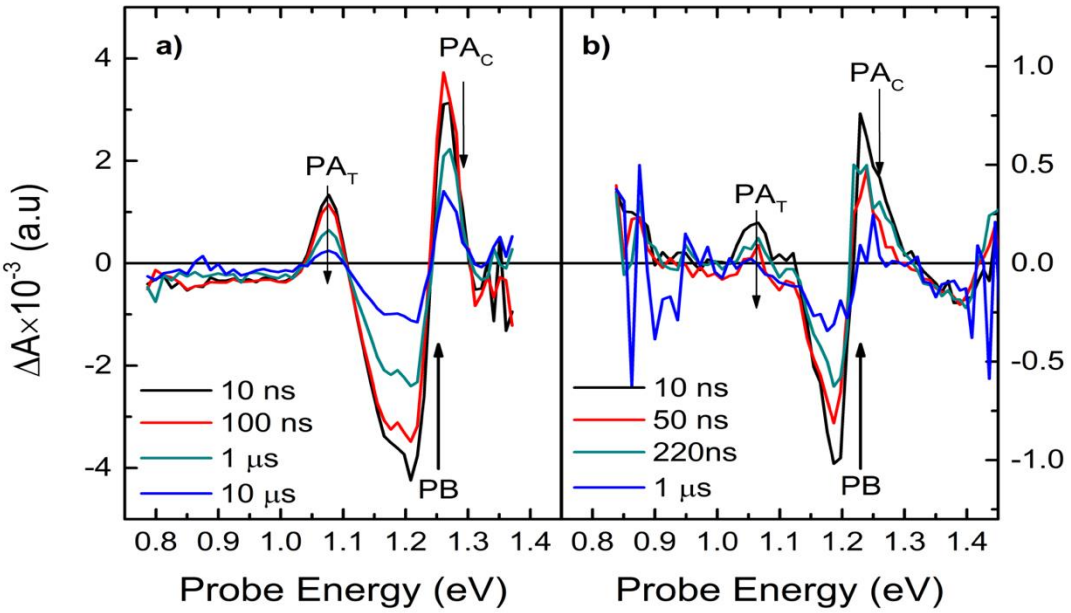

Figure 3-3. Transient absorption spectra of (6,5) rich and (7,5) rich sample (left and right column, respectively) in pump-probe delays from nanoseconds to microseconds. Arrows next to PA and PB bands indicate the direction of evolution with increasing pump-probe delay. PB, PA_T and PA_C represent the photobleach, photoinduced trion band and photoinduced charge band

3.4 Contribution of Photoinduced Excited States to the Total Photobleach

To find out whether further excitations are contributing to the PB bands in Figure 3-2c and d, we take advantage of a recent spectroelectrochemical study in a similar set of samples [3-16]. There, it was found that electrochemical doping of (6,5)-rich samples gives rise to specific absorption bands at 1.06 and 1.27 eV (two photoinduced absorption bands (6,5) chirality, PA_C and PA_T, respectively), and to a concomitant reduction of the E_{11} excitonic resonance of the neutral (6,5) tube at 1.24 eV, such that the overall spectral weight remains unchanged, at least for doping levels below about 0.5 e^- per nm [3-16].

$$PB = E_{11}(neutral) - E_{11}(charged) = PA_C + PA_T \quad (3\text{-}1)$$

Transferring these results to our pump-probe experiment, we expect that the spectral weight of PB should match the sum of the spectral weights of PA_T and PA_C, if PB is exclusively due to charged

states. In other words, the mathematical integral of TA spectra, at least, at late picosecond time scales should be zero.

$$a_C^{6,5} = \int_\omega (\Delta A)_C^{6,5} d\omega = a(PA_C^{6,5}) + a(PA_T^{6,5}) + a(PB_C^{6,5}) = 0 \quad (3\text{-}2)$$

Herein, $a(X) = \int_\omega X d\omega$ is the spectral integral of a photoinduced band X, ω is probe energy, $a_C^{6,5}$ is the contribution of charged states to the TA spectra. Assuming the validity of eq. 3-2 can be extended to all chiralities, we find

$$a_C^{tot} = \sum_{n,m} \int_\omega (\Delta A)_C^{n,m} d\omega = 0 \quad (3\text{-}3)$$

This particular property of the optical probes of charged states (for probe energies around the E11 exciton resonance) allows us to ascribe any non-zero spectral integral to the presence of neutral photoexcitations of either singlet or triplet character:

$$a_n^{tot} = \int_\omega \Delta A d\omega \quad (3\text{-}4)$$

Assuming now that the one-dimensional correlation lengths of neutral and charged excitations along the SWNTs are comparable, we can find the time-resolved ratio of neutral photoexcitations by comparing the excess (uncompensated) photobleach to the total photobleach:

$$r_N^{tot} = a_N^{tot} / \sum_{n,m} PB_{tot}^{n,m} \quad (3\text{-}5)$$

The total photobleach can be approximated by integrating over the negative parts of the TA spectra only:

$$\sum_{n,m} PB_{tot}^{n,m} \geq \int_\omega 1/2 \cdot (\Delta A - |\Delta A|) d\omega \quad , \quad (3\text{-}6)$$

Hereby, we assume that pump-induced photo-doping causes the same kind of charged states as those obtained by electrochemical doping. Based on this reasoning, we can obtain a first estimate for the relative contribution of neutral photoexcitations r_N(t) to the total photoexcitation density, by comparing the total spectral integral with respect to the probe energy ω, to the spectral weight of the bleach signals:

$$r_N(t) \leq \int_\omega \Delta A(t,\omega) d\omega \,/\, \int_\omega 1/2 \cdot (\Delta A(t,\omega) - |\Delta A(t,\omega)|) d\omega, \quad (3\text{-}7)$$

The equal sign in eq.3-7 holds for negligible spectral overlap between negative and positive photoinduced bands. We note that this formalism does so far not allow to obtain quantitative

information on absolute triplet concentrations and yields; to this end the one-dimensional correlation length of the triplet state must be known. Nonetheless, due to the fact that this unknown quantity is not supposed to change on a long picosecond time scale, we can still use the formalism to describe the kinetics of transfer phenomena with relatively high precision.

In Figure 3-4, we show the relative contribution of neutral excited states r_N(t), calculated according to eq.3-7, for the (6,5) rich and the (7,5) rich samples (panels a and b, respectively) at three different intensities. In both samples, r_N(t) is positive over all time scales, evidencing a significant amount of neutral photoexcitations. Two time scales of different time evolutions can be distinguished. For t < 10ps, r_N(t) is intensity dependent, and for the highest intensities, r_N(t) decreases until a minimum is reached at around 10ps (in panel b, this behavior is found for all intensities). For t > 10ps, r_N(t) becomes intensity independent, and monotonously rises until approximately 400ps, reaching a stationary value between 60 and 75%.

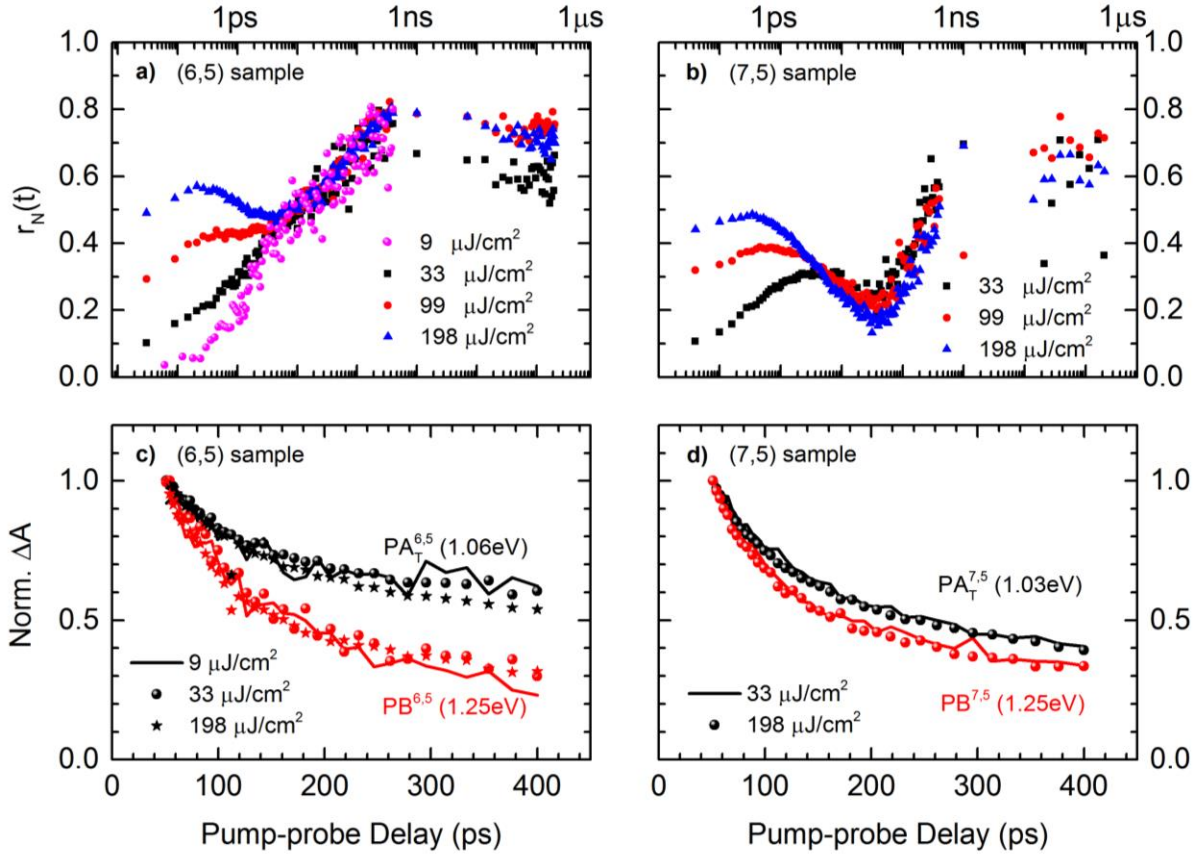

Figure 3-4. Relative contribution of neutral excited states to the total PB signals, calculated per eq.3-7, for (6,5) rich (a) and (7,5) rich (b) samples, respectively. Lower row, (c) and (d), shows the dynamics of main PB and PA_T for the respective sample, at different pump beam intensities.

After pumping at high photon energies, the presence of both singlet excitons and charged states has been shown [3-57]. It is indeed expected that quasi one-dimensional singlet excitons show a net negative TA spectrum, due to the presence of stimulated emission superposing with the bleach [3-96]; therefore, we associate the positive r_N(t) values on the early time scale with singlet excitons. The reduction of r_N(t) at high intensities on the sub-10ps time scale is then explained by rapid bimolecular annihilation of singlet excitons, a commonly observed process in SWNTs [3-52]. On the other hand, the high r_N(t) values on the long timescale cannot be explained by singlet excitons. As Figure 3-4 shows r_N(t) is stable for at least 500 ns, which means that the lifetime of the associated neutral excited state must be at least in the microsecond range. Such a long lifetime strongly argues against a spin allowed relaxation pathway, and therefore excludes singlet excitons. Since it has recently been shown in similar samples that triplet excitons are generated with up to 32 % yield [3-97], we tentatively assign the excess bleach (causing positive r_N(t) values) on the time scale t > 50ps to triplet excitons (see the original TA spectra on the microsecond time scale in Figure 3-3).

To confirm our notion that the overall photobleach after long times contains contributions from two different photoexcited states, we present, in Figure 3-4c and d, the decay traces at fixed probe energies corresponding to the main bleach and the trion absorption, both normalized to their value at t=50ps. For the (6,5) rich sample, we find that the signal in the trion band is reduced by 40% between 50 and 400ps, while the signal in the main photobleach is reduced by 70% in the same time interval. It follows that there must be a second contribution to the photobleach which decays much faster than the charged states. In the next section, we show that this decay is caused by triplet transfer to a different chirality. In the (7,5) rich sample, there is still a difference in the normalized trion and bleach kinetics, but not as pronounced as in the (6,5) rich sample. Below, we show that in this sample, no inter-tube triplet transfer can be observed. The different kinetics, therefore, reflect different intratube triplet and charge relaxation times. Importantly, these findings are the same for pump intensities ranging over more than an order of magnitude (see different symbols in Figure 3-4c), from which we conclude that the observed processes are valid also for low-level irradiation under solar conditions. We note that other authors do not find signatures of charged states at low pump intensities [3-98], which seems to be in contrast with our findings. As Yuma et al. show [3-63], maximum singlet concentration and maximum trion absorption are proportional

across a range of pump intensities, which agrees with a picture of charge generation by exciton annihilation under certain conditions. Further studies, e.g. showing a deviation of this linear relationship at very low intensities where exciton annihilation yield is limited by the natural exciton lifetime, are necessary to conclusively resolve this issue.

Determination of r_N(t) based on eq.3-7 is the most direct way to show the presence of any negative TA signal that is not compensated by either PA_C or PA_T and hence is caused by a neutral photoexcitation. However, PA_C, PA_T, and PB occur at well-known probe energies that are specific for the respective chirality. Consequently, at pump-probe delays long enough to neglect singlet excitons, the excess bleach becomes a chirality specific optical probe for triplets, giving us the opportunity to trace inter-tube triplet transfer. To this end we define a chirality specific excess bleach:

$$PB_{exc}^{n,m} = a(PB^{n,m}) - [a(PA_C^{n,m}) + a(PA_T^{n,m})] \tag{3-8}$$

where $a(X)(t) = \int_{\omega=-\infty}^{\infty} X(t)d\omega$ is the time-dependent spectral area of a photoinduced band X. After long times where singlet excitons do not significantly contribute to the excess bleach, the excess bleach becomes proportional to the time-resolved triplet concentration $T^{n,m}$ on a specific chirality (n,m) by Lambert-Beer's law:

$$PB_{exc}^{nm}(t) = d \cdot \sigma_T^{n,m} \cdot T^{n,m}(t) \tag{3-9}$$

Here, $\sigma_T^{n,m}$ is the absorption cross-section of triplet states on (n,m) tubes, which is caused by phase space filling and related to the triplet exciton size, a quantity which is unknown so far, and d is the film thickness. Since $\sigma_T^{n,m}$ does not significantly depend on time, we can use eq.3-9 to trace triplet exciton dynamics in the time domain by evaluating the excess bleach for different chiralities, in order to find evidence for population transfer kinetics. For that, we need to find the total spectral weights a(X) in eq.3-8 for each chirality, which due to strong spectral congestion requires a global analysis.

3.5 Global Spectral Modelling

Global spectral modeling of the TA spectra is performed with a custom-built software written by my supervisor, in which a python script wraps around open source packages for matrix algebra (numpy) and nonlinear optimization (scipy). TA spectra after 50ps pump-probe delay are chosen

for the modelling to avoid strong contributions from singlet excitons (see Figure 3-2). We include only the (6,5) and (7,5) chiralities in the spectral model for the (6,5) rich sample, while (6,5), (7,5) and (8,4) are included for (7,5) rich sample. The main reasons for including those certain chiralities in the model but not all are: i) those are the main contributors in both ground state absorption and TA spectra (see Figure 3-1); ii) except (9,1) in (6,5) rich samples, the E11 transition bands of all other chiralities in both samples lie below those of (8,4), and their respective trion (PAT) bands might reside outside of our measurement window, which adds difficulties on quantifying the excess PB we needed for further analysis of the TA spectra. In the model, only the main chirality ((6,5) in the (6,5) rich sample, and (7,5) in the (7,5) rich sample) produces a PB, a PA_T and a blue shifted photoinduced charge (PA_C) band, whereas each other chirality produces just a PB, as we do not see any signature of rising $PA_T^{7,5}$ in the TA spectra of (6,5) rich sample, although the $PB^{7,5}$ increases a lot in time. Then we apply a Gaussian line shape with specific parameters for all bands, and combine them to reproduce the complete TA spectra.

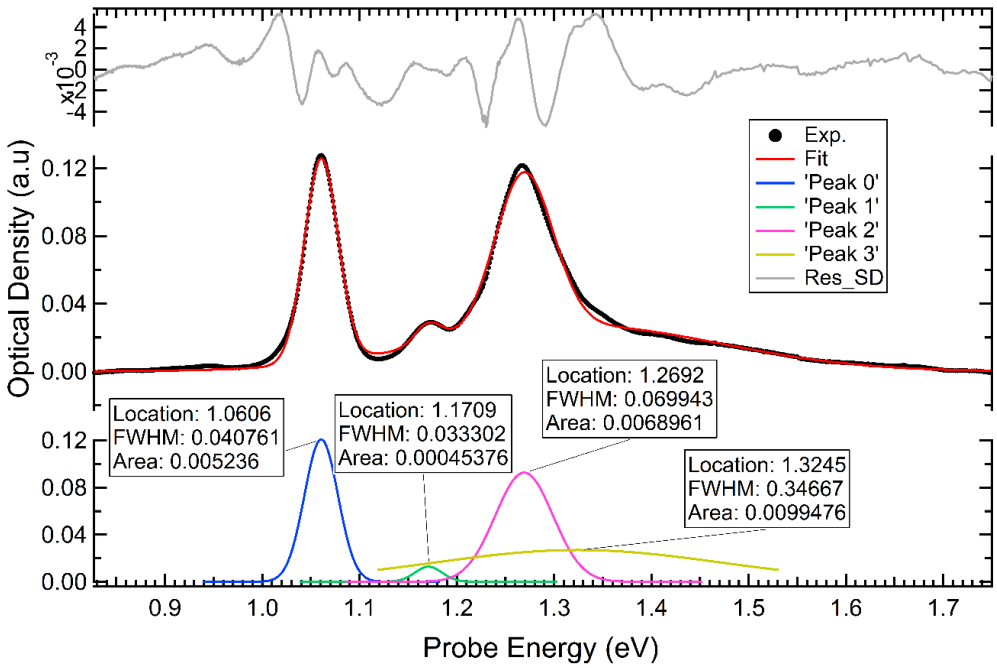

Figure 3-5. Ground state absorption spectra of (6,5) rich SWNTs recorded at Moderate electrochemical doping [3-16]. Gaussian line shapes are applied for all four bands, and parameters of only the 'Peak 0' and 'Peak 2' are used for $PA_T^{6,5}$ and $PA_C^{6,5}$ in spectral modeling, as the other two peaks are originated from different chiralities

The parameters for PB can be determined directly from the ground state absorption spectra, or from the actual TA spectra at early times, as they usually coincide very well. The necessary

parameters for $PA_T^{6,5}$ and $PA_C^{6,5}$ have been taken from the global fit result of ground state absorption spectra of an electrochemically doped, similarly prepared, SWNT sample [3-16]. In that study, a set of ground state spectra, recorded at various doping levels, are reproduced quite well just with three spectral components namely undoped, moderately doped and heavily doped spectra. For our purpose of spectral modeling here, we only use the moderately doped one (see Figure 3-5), because it exhibits a $PA_T^{6,5}$ band around 1.06eV and a $PA_C^{6,5}$ around 1.27eV. We assume that spectral doping of SWNTs with the pump pulse in the pump-probe experiment may induce a similar effect. To avoid inconsistency, we fit a set of TA spectroscopy data taken at different pump intensities with a whole range of pump-probe delays after 50ps at once, with just a single model. We kept the number of free parameters low by fixing the spectral shapes and relative area ratios of the PA_C and PA_T bands to the corresponding bands in the electrochemical data. Neither line width nor band center are allowed to change with pump intensities, so that any pump intensity dependent spectral features could be observed directly.

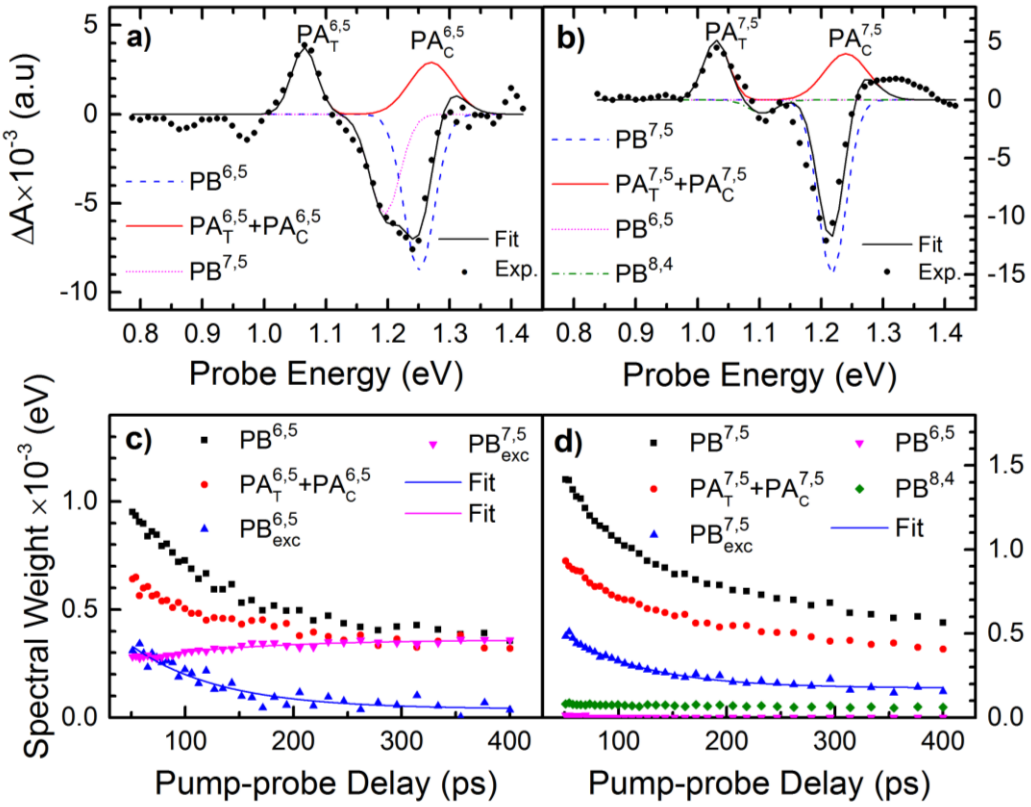

Figure 3-6. *Global analysis of TA spectra from Figure 2 for the (6,5) rich and (7,5) rich sample (panel a and b, respectively) at t = 167ps (black curves). The other curves show single contributions to the global fit, as indicated in the legend. The resulting spectral weights are shown in panel c and d*

Table 3-3. Best spectral fit parameters obtained for (7,5) rich sample. In the table, rel.sp.wt stands for relative spectral weights, and is dimensionless, the rest are in (eV)

$PB^{6,5}$ center	$PB^{6,5}$ width	$PA_C^{6,5}$ center	$PA_C^{6,5}$ width	$PA_C^{6,5}$ rel.sp.wt	$PA_T^{6,5}$ center	$PA_T^{6,5}$ width	$PA_T^{6,5}$ rel.sp.wt	$PB^{7,5}$ center
1.25	0.05	1.274	0.07	0.57	0.065	0.041	0.43	1.195

For the (6,5) rich sample, the model gave satisfactory fits, see curves in Figure 3-6a, except the PA signal around 1.33eV, which possibly because of the neglected (9,1) chirality in our spectral model. Obtained best fit parameters are given in Table 3-3. Outcome of the global spectral modeling would be then the contribution of different excited state species on the TA spectra at certain times. In other words, it gives information about the population dynamics of diverse excited states, as depicted in Figure 3-6c.

In the case of (7,5) rich sample, we don't have similar electrochemical data as for (6,5). But we assume the parameters to be not very different from those of (6,5) rich sample's, except the locations of the bands. Then we take the offsets between $PB^{6,5}$ and $PA_c^{6,5}$, $PB^{6,5}$ and $PA_T^{6,5}$ from the (6,5) rich sample to determine the band centers of the $PA_C^{7,5}$ and $PA_T^{7,5}$ in the (7,5) rich sample. The rest of the parameters are set to the same values as for the (6,5) rich sample. Figure 3-6b and Figure 3-6d show the results of global spectral modeling and the corresponding population dynamics, respectively. This procedure leads to a good agreement between experiment and simulation, except the PA signal around 1.33eV, which possibly because of the neglected (9,1) chirality in our spectral model.

3.6 Intertube Triplet Transfer

Figure 3-6c and d shows spectral weights a(X)(t) resulting from fits like those displayed in Figure 3-6a and b, for pump-probe delays between 50 and 400ps, for the (6,5) rich and (7,5) rich samples, respectively. In the (6,5) rich sample in Figure 3-6c, we find that $a(PB^{6,5})(t) > [a(PA_C^{6,5})(t) + a(PA_T^{6,5})(t)]$ for all times but the difference between the total bleach of the (6,5) tubes and the respective charge-induced PA bands is diminishing after long times, compare black and red symbols, respectively. Consequently, $PB_{exc}^{6,5} \rightarrow 0$ on a 200 ps time scale, see blue symbols, showing that the remaining $PB^{6,5}$ for t > 400ps is nearly exclusively due to charged states. The

decay of $PB_{exc}^{6,5}$ is corroborated with an absolute increase of $PB_{exc}^{7,5}$ (magenta symbols in Figure 3-6c) with the same dynamics, from which we conclude that triplet excitons are transferred from (6,5) to (7,5) tubes on a 70ps time scale. The transfer dynamics can be well described by simple monoexponential functions (see lines in Figure 6c) which might indicate that triplet energy transfer is not diffusion limited. Diffusion control would normally entail dispersive kinetics, which we do not observe. In table 3-4, we show that the monoexponential times for $PB_{exc}^{6,5}$ decay and $PB_{exc}^{7,5}$ rise match very well, supporting our picture of triplet exciton transfer. In the last column of table 3-4, we compare the excess bleach at t=50ps with the total bleach immediately after the pump pulse. Since the latter is expected to sum up over all pump-induced excited states, we can get an order of magnitude guess of the triplet yield. We find values between 4-5 %. The fact that the values decrease with increasing pump intensity is an indication that exciton annihilation is not the reason for the generation of triplet states. However, in analogy to eq.3-8 we must highlight that the sizes (longitudinal correlation lengths) of singlets, charges and triplets, all of which are contributing to the total bleach at t=0, might substantially differ from each other, given the large differences in Coulomb and exchange interactions of these species in a 1D system [3-99].

In the (7,5) rich sample (Figure 3-6b), we find a high $PB_{exc}^{7,5}$ which does not decay to zero on a 400ps time scale. Moreover, the excess bleach $PB_{exc}^{8,4}$ of the (8,4) tube remains very low and almost constant over this time scale, not showing any sign of triplet exciton transfer into this chirality. This is especially surprising as the relative density of (8,4) as possible acceptor tubes for triplet transfer in the (7,5) rich sample is higher than that of (7,5) acceptor tubes in the (6,5) rich sample (see Figure 3-1). In the case of singlet exciton transfer, such a dependence on chirality could be easily explained by the lack of spectral overlap between donor and acceptor. This picture is however not applicable to triplet energy transfer, being usually discussed in a Dexter-type transfer model, formally requiring two electron transfer steps to conserve the total spin throughout the transfer process [3-100]. As the electrochemical bandgaps are diameter dependent [3-101], our result seems to suggest a higher triplet transfer rate from higher towards lower bandgap tubes, than between tubes of similar diameter. However, this notion needs to be confirmed in a broader range of chiralities.

From Table 3-4 and 3-2, we get additional insight into the triplet generation mechanism. The approximate triplet yield η_{tot}^{tri} is clearly reduced at higher pump intensities. As explained in the previous section, the absolute values are error prone because the triplet exciton length is not known. This does however not affect the evolution of the triplet yield with pump intensity, as the triplet size is not expected to depend on pump intensity. We can thus trace the intensity dependence of the triplet yield with a much higher precision than the absolute triplet yield. Thus, the reduction of the triplet yield at higher pump intensity is an indication that triplets are not generated by high-intensity effects such as exciton - exciton annihilation or bimolecular charge recombination; in this case the triplet yield should increase with intensity. The reduction of the triplet yield rather shows that at high pump intensity, the *precursor* for triplet generation is removed, pointing to relaxed singlet excitons as precursors for triplet generation.

*Table 3-4. Exponential fit result of $PB_{exc}^{6,5}$ and $PB_{exc}^{7,5}$ and corresponding triplet yield in (6,5) rich sample. y = A*exp(-x/τ) + y0 is used as fit model, where A is amplitude, x is pump probe delay time, y0 is offset, τ is life time, and η_{tot}^{tri} is the total triplet yield at 50ps, which was obtained by dividing the spectral weight of excess bleach at 50ps by the spectral weight of total bleach at 0ps*

Pump Power	$A_{PB}^{7,5}$	$\tau_{PB}^{7,5}$(ps)	$A_{exc}^{6,5}$	$\tau_{exc}^{6,5}$(ps)	η_{tot}^{tri} (%, at 50ps)
33 uJ/cm^2	-1.65E-04	110	5.49E-04	82	4.5 ± 0.5
99 uJ/cm^2	-3.15E-04	80	1.16E-03	76	4.2 ± 0.5
198 uJ/cm^2	-6.34E-04	64	2.17E-03	65	3.8 ± 0.1

*Table 3-5. Exponential fit result of $PB_{exc}^{7,5}$ and corresponding triplet yield in (7,5) rich sample. y = A*exp(-x/τ) + y0 is used as fit model, where A is amplitude, x is pump probe delay time, y0 is offset, τ is life time, and η_{tot}^{tri} is the total triplet yield at 50ps which was obtained by dividing the spectral weight of excess bleach at 50ps by the spectral weight of total bleach at 0ps*

Pump Power	$A_{PB}^{8,4}$	$\tau_{PB}^{8,4}$(ps)	$A_{exc}^{7,5}$	$\tau_{exc}^{7,5}$(ps)	η_{tot}^{tri} (%, at 50ps)
33 uJ/cm^2	0	-	3.64E-04	1.48E+02	8.4 ± 0.2
99 uJ/cm^2	0	-	6.62E-04	1.40E+02	7.1 ± 0.2
198 uJ/cm^2	0	-	6.48E-04	2.10E+02	5.5 ± 0.2

3.7 Conclusions

We have performed transient absorption spectroscopy on a time scale from femtoseconds to microseconds on chirality sorted single-walled carbon nanotube samples, rich in either (6,5) or (7,5) tubes. By comparing the TA spectra with the results from spectroelectrochemical measurements, specific contributions of charged states and triplet excitons to the transient photobleach of each chirality have been quantified. This allowed us to trace, for the first time, the inter-tube transfer of triplet excitons. We found a complete transfer of triplet excitons from the (6,5) to the (7,5) chirality in 70ps with first order kinetics, showing that the transfer process is not diffusion limited. In contrast, we observed no transfer of triplets from the (7,5) to the (8,4) tubes. From intensity-dependent measurements, we found relaxed singlet states to be precursors for triplet formation.

REFERENCES

[3-1]. F. Wang, G. Dukovic, L. E. Brus, and T. F. Heinz, Science 308, 838 (2005).

[3-2]. J. Maultzsch et al., Physical Review B 72, 241402 (2005).

[3-3]. J. Lefebvre and P. Finnie, Nano letters 8, 1890 (2008).

[3-4]. T. Ogawa and T. Takagahara, Physical Review B 44, 8138 (1991).

[3-5]. T. Dürkop, S. Getty, E. Cobas, and M. Fuhrer, Nano letters 4, 35 (2004).

[3-6]. Y. Miyata, K. Shiozawa, Y. Asada, Y. Ohno, R. Kitaura, T. Mizutani, and H. Shinohara, Nano Research 4, 963 (2011).

[3-7]. F. Bottacchi, L. Petti, F. Späth, I. Namal, G. Tröster, T. Hertel, and T. D. Anthopoulos, Applied Physics Letters 106, 193302 (2015).

[3-8]. H. R. Byon and H. C. Choi, Journal of the American Chemical Society 128, 2188 (2006).

[3-9]. Singh et al., Journal of luminescence 130, 2157 (2010).

[3-10]. W. L. Abeygunasekara, P. Hiralal, L. Samaranayake, C.-T. Chien, A. Kumar, A. J. Flewitt, V. Karunaratne, and G. A. Amaratunga, Applied Physics Letters 106, 123305 (2015).

[3-11]. L. Lüer, S. Hoseinkhani, D. Polli, J. Crochet, T. Hertel, and G. Lanzani, Nature Physics 5, 54 (2008).

[3-12]. H. Harutyunyan, T. Gokus, A. A. Green, M. C. Hersam, M. Allegrini, and A. Hartschuh, Nano letters 9, 2010 (2009).

[3-13]. R. Matsunaga, Y. Miyauchi, K. Matsuda, and Y. Kanemitsu, Physical Review B 80 (2009).

[3-14]. R. Matsunaga, K. Matsuda, and Y. Kanemitsu, Journal of Luminescence 129, 1702 (2009).

[3-15]. K. Nagatsu, S. Chiashi, S. Konabe, and Y. Homma, Physical Review Letters 105 (2010).

[3-16]. H. Hartleb, F. Späth, and T. Hertel, ACS nano 9, 10461 (2015).

[3-17]. W. Zhou, D. Nakamura, H. Liu, H. Kataura, and S. Takeyama, Sci Rep 4, 6999 (2014).

[3-18]. Y. Chen et al., Advanced Materials 26, 5898 (2014).

[3-19]. C. Wang, K. Takei, T. Takahashi, and A. Javey, Chemical Society Reviews 42, 2592 (2013).

[3-20]. D. Jariwala, V. K. Sangwan, L. J. Lauhon, T. J. Marks, and M. C. Hersam, Chemical Society Reviews 42, 2824 (2013).

[3-21]. L. Liu, W. E. Stanchina, and G. Li, Applied Physics Letters 94, 233309 (2009).

[3-22]. J. M. Holt, A. J. Ferguson, N. Kopidakis, B. A. Larsen, J. Bult, G. Rumbles, and J. L. Blackburn, Nano letters 10, 4627 (2010).

[3-23]. M. Zheng et al., Science 302, 1545 (2003).

[3-24]. M. S. Arnold, A. A. Green, J. F. Hulvat, S. I. Stupp, and M. C. Hersam, Nature nanotechnology 1, 60 (2006).

[3-25]. E. H. Hároz, W. D. Rice, B. Y. Lu, S. Ghosh, R. H. Hauge, R. B. Weisman, S. K. Doorn, and J. Kono, ACS nano 4, 1955 (2010).

[3-26]. J. G. Duque, H. Chen, A. K. Swan, A. P. Shreve, S. Kilina, S. Tretiak, X. Tu, M. Zheng, and S. K. Doorn, ACS nano 5, 5233 (2011).

[3-27]. S. Bonhommeau et al., Journal of Physical Chemistry C 117, 14840 (2013).

[3-28]. Kaplan-Ashiri, E. J. Titus, and K. A. Willets, ACS nano 5, 1033 (2011).

[3-29]. F. Hennrich, R. Krupke, S. Lebedkin, K. Arnold, R. Fischer, D. E. Resasco, and M. M. Kappes, The Journal of Physical Chemistry B 109, 10567 (2005).

[3-30]. C. Fantini, A. Jorio, M. Souza, M. S. Strano, M. S. Dresselhaus, and M. A. Pimenta, Phys Rev Lett 93, 147406 (2004).

[3-31]. K. Liu et al., Proceedings of the National Academy of Sciences 111, 7564 (2014).

[3-32]. H. Pathangi, P. M. Vereecken, A. Klekachev, G. Groeseneken, and A. Witvrouw, Journal of Nanoscience 2014 (2014).

[3-33]. F. Vialla, E. Malic, B. Langlois, Y. Chassagneux, C. Diederichs, E. Deleporte, P. Roussignol, J.-S. Lauret, and C. Voisin, Physical Review B 90, 155401 (2014).

[3-34]. J. C. Blancon et al., Nat Commun 4, 2542 (2013).

[3-35]. S. Mouri and K. Matsuda, Journal of Applied Physics 111, 094309 (2012).

[3-36]. S. Ohmori, T. Saito, M. Tange, B. Shukla, T. Okazaki, M. Yumura, and S. Iijima, The Journal of Physical Chemistry C 114, 10077 (2010).

[3-37]. N. Nair, M. L. Usrey, W. J. Kim, R. D. Braatz, and M. S. Strano, Anal Chem 78, 7689 (2006).

[3-38]. S. Maruyama, Y. Murakami, E. Einarsson, and T. Edamura, Carbon 43, 2664 (2005).

[3-39]. L. J. Nogaj, J. A. Smyder, K. E. Leach, X. Tu, M. Zheng, and T. D. Krauss, J Phys Chem Lett 6, 2816 (2015).

[3-40]. F. F. Bergler, F. Schoeppler, F. K. Brunecker, M. Hailman, and T. Hertel, Journal of Physical Chemistry C 117, 13318 (2013).

[3-41]. M. Rujun, M. M. Menamparambath, P. Nikolaev, and B. Seunghyun, Advanced Materials 25, 2548 (2013).

[3-42]. T. K. Cherukuri, D. A. Tsyboulski, and R. B. Weisman, ACS nano 6, 843 (2011).

[3-43]. D. A. Tsyboulski, J.-D. R. Rocha, S. M. Bachilo, L. Cognet, and R. B. Weisman, Nano Letters 8, 1270 (2008).

[3-44]. L. J. Carlson, S. E. Maccagnano, M. Zheng, J. Silcox, and T. D. Krauss, Nano letters 7, 3698 (2007).

[3-45]. D. A. Tsyboulski, J.-D. R. Rocha, S. M. Bachilo, L. Cognet, and R. B. Weisman, Nano letters 7, 3080 (2007).

[3-46]. P. Deria, J. H. Olivier, J. Park, and M. J. Therien, Journal of the American Chemical Society 136, 14193 (2014).

[3-47]. T. Koyama, S. Yoshimitsu, Y. Miyata, H. Shinohara, H. Kishida, and A. Nakamura, Journal of Physical Chemistry C 117, 20289 (2013).

[3-48]. B. A. Ruzicka, R. Wang, J. Lohrman, S. Ren, and H. Zhao, Physical Review B 86, 205417 (2012).

[3-49]. J. Yookyung, M. N. Slipchenko, L. Chang Hua, A. E. Ribbe, Z. Zhaohui, Y. Chen, and C. Ji-Xin, Physical Review Letters 105, 217401 (4 pp.) (2010).

[3-50]. D. J. Styers-Barnett, S. P. Ellison, B. P. Mehl, B. C. Westlake, R. L. House, C. Park, K. E. Wise, and J. M. Papanikolas, Journal of Physical Chemistry C 112, 4507 (2008).

[3-51]. J. Yang, M. M. Kappes, H. Hippler, and A. Unterreiner, Diffusion and Defect Data Part B (Solid State Phenomena) 121-123, 905 (2007).

[3-52]. M. Ying-Zhong, L. Valkunas, S. M. Bachiloc, and G. R. Fleming, Physical Chemistry Chemical Physics 8, 5689 (2006).

[3-53]. R. J. Ellingson, C. Engtrakul, M. Jones, M. Samec, G. Rumbles, A. J. Nozik, and M. J. Heben, Physical Review B 71, 8, 115444 (2005).

[3-54]. J. P. Yang, M. M. Kappes, H. Hippler, and A. N. Unterreiner, Physical Chemistry Chemical Physics 7, 512 (2005).

[3-55]. V. A. Nadtochenko, A. S. Lobach, F. E. Gostev, D. O. Tcherbinin, A. Sobennikov, and O. M. Sarkisov, AIP Conference Proceedings, 146 (2005).

[3-56]. M. S. Arnold, S. Lan, S. C. Cruz, J. E. Sharping, S. I. Stupp, P. Kumar, and M. C. Hersam, in Quantum Sensing and Nanophotonic Devices, edited by M. Razeghi, and G. J. Brown2004), pp. 376.

[3-57]. J. J. Crochet, S. Hoseinkhani, L. Luer, T. Hertel, S. K. Doorn, and G. Lanzani, Phys Rev Lett 107, 257402 (2011).

[3-58]. L. Lüer, J. Crochet, T. Hertel, G. Cerullo, and G. Lanzani, ACS nano 4, 4265 (2010).

[3-59]. L. Lüer, G. Lanzani, J. Crochet, T. Hertel, J. Holt, and Z. V. Vardeny, Physical Review B 80 (2009).

[3-60]. Schilling, Daniel, et al. "Ultrafast Spectral Exciton Diffusion in Single-Wall Carbon Nanotubes Studied by Time-Resolved Hole Burning." The Journal of Physical Chemistry C 119.42 (2015): 24116-24123.

[3-61]. M. J. O'connell et al., Science 297, 593 (2002).

[3-62]. L. Huang and T. D. Krauss, Physical review letters 96, 057407 (2006).

[3-63]. B. Yuma et al., Physical Review B 87, 205412 (2013).

[3-64]. J. Park, P. Deria, J.-H. Olivier, and M. J. Therien, Nano Letters 14, 504 (2014).

[3-65]. R. Levy, B. Hönerlage, and J. Grun, Physical Review B 19, 2326 (1979).

[3-66]. J.-H. Olivier, J. Park, P. Deria, J. Rawson, Y. Bai, A. S. Kumbhar, and M. J. Therien, Angewandte Chemie (International ed. in English) 54, 8133 (2015).

[3-67]. G. Soavi, F. Scotognella, D. Viola, T. Hefner, T. Hertel, G. Cerullo, and G. Lanzani, Sci Rep 5, 9681 (2015).

[3-68]. J. Park, O. G. Reid, J. L. Blackburn, and G. Rumbles, Nat Commun 6, 8809 (2015).

[3-69]. L. Adamska, G. V. Nazin, S. K. Doorn, and S. Tretiak, The Journal of Physical Chemistry Letters 6, 3873 (2015).

[3-70]. S. Schaefer, N. M. B. Cogan, and T. D. Krauss, Nano Letters 14, 3138 (2014).

[3-71]. D. R. Barbero, N. Boulanger, M. Ramstedt, and J. Yu, Adv Mater 26, 3111 (2014).

[3-72]. G. Soavi, F. Scotognella, D. Brida, T. Hefner, F. Späth, M. R. Antognazza, T. Hertel, G. Lanzani, and G. Cerullo, The Journal of Physical Chemistry C 117, 10849 (2013).

[3-73]. R. Matsunaga, K. Matsuda, and Y. Kanemitsu, Phys Rev Lett 106, 037404 (2011).

[3-74]. C. Sciascia, J. Crochet, T. Hertel, and G. Lanzani, European Physical Journal B 75, 115 (2010).

[3-75]. C. Gadermaier, E. Menna, M. Meneghetti, W. J. Kennedy, Z. V. Vardeny, and G. Lanzani, Nano Lett 6, 301 (2006).

[3-76]. F. Jakubka, S. B. Grimm, Y. Zakharko, F. Gannott, and J. Zaumseil, Acs Nano 8, 8477 (2014).

[3-77]. N. Akizuki et al., Physical Review B 89 (2014).

[3-78]. T. Koyama, S. Shimizu, Y. Miyata, H. Shinohara, and A. Nakamura, Physical Review B 87, 165430 (2013).

[3-79]. M. Okano, T. Nishihara, Y. Yamada, and Y. Kanemitsu, Ultrafast Phenomena and Nanophotonics Xvii 8623, 86231f (2013).

[3-80]. T. Nishihara, Y. Yamada, M. Okano, and Y. Kanemitsu, Applied Physics Letters 103, 023101 (2013).

[3-81]. S. Mouri, Y. Miyauchi, M. Iwamura, and K. Matsuda, Physical Review B 87 (2013).

[3-82]. J. S. Park, Y. Hirana, S. Mouri, Y. Miyauchi, N. Nakashima, and K. Matsuda, Journal of the American Chemical Society 134, 14461 (2012).

[3-83]. K. Watanabe and K. Asano, Physical Review B 85, 035416 (2012).

[3-84]. S. M. Santos, B. Yuma, S. Berciaud, J. Shaver, M. Gallart, P. Gilliot, L. Cognet, and B. Lounis, Physical Review Letters 107, 187401 (2011).

[3-85]. D. Song, F. Wang, G. Dukovic, M. Zheng, E. D. Semke, L. E. Brus, and T. F. Heinz, Applied Physics a-Materials Science & Processing 96, 283 (2009).

[3-86]. S. Matsumoto, H. Matsui, A. Maeda, T. Takenobu, Y. Iwasa, Y. Miyata, H. Kataura, Y. Maniwa, and H. Okamoto, Japanese Journal of Applied Physics Part 2-Letters & Express Letters 45, L513 (2006).

[3-87]. J. Park, P. Deria, and M. J. Therien, Journal of the American Chemical Society 133, 17156 (2011).

[3-88]. R. Matsunaga, K. Matsuda, and Y. Kanemitsu, Physical Review B 81 (2010).

[3-89]. D. Mohite, T. S. Santos, J. S. Moodera, and B. W. Alphenaar, Nat Nanotechnol 4, 425 (2009).

[3-90]. D. Stich, F. Spaeth, H. Kraus, A. Sperlich, V. Dyakonov, and T. Hertel, Nature Photonics 8, 139 (2014).

[3-91]. Kim, Woo-Jae, et al. "Connecting single molecule electrical measurements to ensemble spectroscopic properties for quantification of single-walled carbon nanotube separation." *Journal of the American Chemical Society* 131.9 (2009): 3128-3129.

[3-92]. Grechko, Maksim, et al. "Diffusion-assisted photoexcitation transfer in coupled semiconducting carbon nanotube thin films." *ACS nano* 8.6 (2014): 5383-5394.

[3-93]. Koyama, Takeshi, et al. "Ultrafast energy transfer of one-dimensional excitons between carbon nanotubes: a femtosecond time-resolved luminescence study." *Physical Chemistry Chemical Physics* 14.3 (2012): 1070-1084.

[3-94]. Koyama, Takeshi, et al. "Bright luminescence and exciton energy transfer in polymer-wrapped single-walled carbon nanotube bundles." *The Journal of Physical Chemistry Letters* 1.21 (2010): 3243-3248.

[3-95]. Cruz, CH Brito, et al. "Dynamics of spectral hole burning." *IEEE journal of quantum electronics* 24.2 (1988): 261-269.

[3-96]. van Burgel, Mirjam, Douwe A. Wiersma, and Koos Duppen. "The dynamics of one-dimensional excitons in liquids." *The Journal of chemical physics* 102.1 (1995): 20-33.

[3-97]. Florian Leonhard Späth. "Preparation and Characterization of Single-Wall Carbon Nanotube-Polyfluorene-Complexes." *Doctoral Thesis, Universität Würzburg, Fakultät für Chemie und Pharmazie* (2015).

[3-98]. Dowgiallo, Anne-Marie, et al. "Ultrafast spectroscopic signature of charge transfer between single-walled carbon nanotubes and C60." *ACS nano* 8.8 (2014): 8573-8581.

[3-99]. Perebeinos, Vasili, J. Tersoff, and Phaedon Avouris. "Scaling of excitons in carbon nanotubes." *Physical review letters* 92.25 (2004): 257402.

[3-100]. Monguzzi, A., R. Tubino, and F. Meinardi. "Upconversion-induced delayed fluorescence in multicomponent organic systems: Role of Dexter energy transfer." *Physical Review B* 77.15 (2008): 155122.

[3-101]. Paolucci, Demis, et al. "Singling out the electrochemistry of individual single-walled carbon nanotubes in solution." *Journal of the American Chemical Society* 130.23 (2008): 7393-7399.

4 EFFECT OF SWNTS ON THE PERFORMANCE OF THE OSC DEVICES

4.1 Introduction

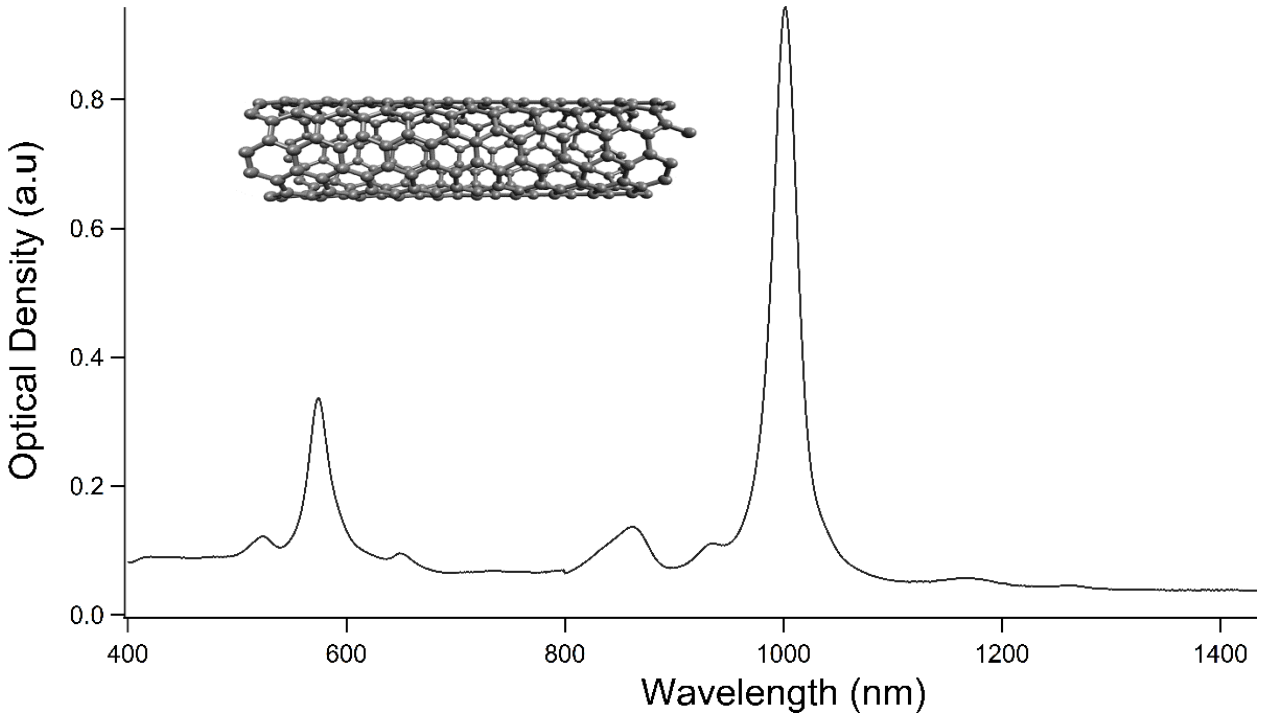

Figure 4-1. Absorption spectra of pristine (6,5) rich SWNT film. The peaks at 1000nm, 850nm and 575nm are the E_{11}, E_{11}, phonon side and E_{22} transition bands, respectively

Possessing high thermal and chemical stability, high charge carrier mobility as well as tunable bandgap, single wall carbon nanotubes (SWNTs) can be promising candidates for organic solar cells (OSC) to improve the charge extraction and consequently the power conversion efficiency (PCE). However, the record PCE of OSCs containing SWNTs remain far below the SWNT free ones [4-1], which has been ascribed to a lack of knowledge and control of the nanostructure [4-2]. Efficient charge transfer from smaller diameter tubes to the larger ones has been reported [4-3]. These larger tubes could act as traps for the free charge carriers in OSCs when a mixture of chiralities is used, if their band gap does not match that of the donor-acceptor. To resolve these issues, a very pure (6,5) SWNT dispersion (see Figure 4-1) is prepared by the polymer wrapping method followed by ultracentrifugation and filtering. The excited state dynamics of the SWNTs is studied via femtosecond transient absorption (TA) spectroscopy. Besides the intrinsic photoinduced neutral (singlet and triplet [4-4]) and charged (charge and trion) states, no intertube excited state transfer phenomenon is observed. The long-lived triplet excitons could be a disadvantage in OSCs if could not be converted into free charge carriers, while the generation of

free charge carriers in SWNTs itself could be an advantage, although the main charge generation process in OSCs takes place at the donor-acceptor interface. Then, BHJ devices are fabricated by mixing a small amount of the nanotube dispersion (0.1% mass ratio) into the active layer solutions P3HT:PCBM and OPV48:PCBM, respectively. OPV48 is a representative name for the donor polymer PBTZT-stat-BDTT-8. Its absorption maximum stands around 620nm, and it has a HOMO of -5.4eV and a LUMO of -3.7eV and bandgap of 1.7eV [4-5].

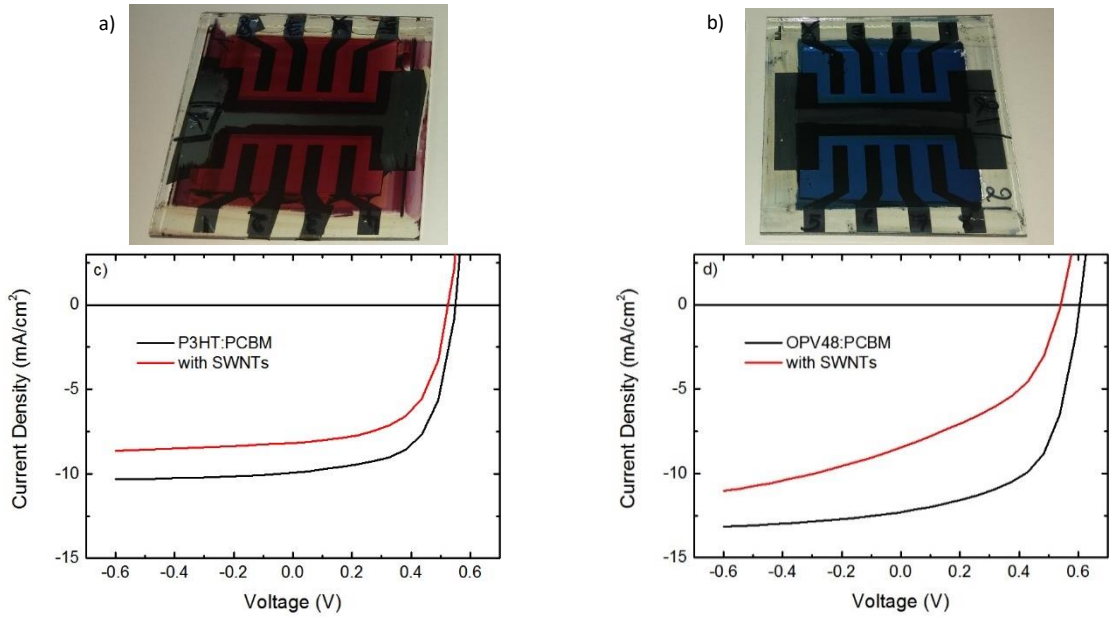

Figure 4-2. Picture of actual P3HT:PCBM (a) and OPV48:PCBM (b) devices, respectively; (c) and (d) are their corresponding J-V characteristics with and without SWNTs under one sun illumination

The electrical characterization under 1sun illumination (solar simulator) showed significant PCE losses in both P3HT:PCBM and OPV48:PCBM devices with SWNTs with significant short circuit current density (J_{sc}) and fill factor (FF) losses (see Figure 4-2). Reduction of J_{sc} implies either a carrier generation problem (under the condition that all the photogenerated charge carriers are extracted at short circuit), or a non-geminate recombination problem during the carrier extraction, which in its turn could also cause an open circuit voltage (V_{oc}) loss [4-6]. An increase in non-geminate recombination can be revealed much clearly in the FF factor loss [4-7]. Nevertheless, the non-geminate recombination is again a function of carrier lifetime (τ) and carrier density (n), and both generation and recombination could be electric field dependent [4-8]. In that regard, the J-V characteristics alone is not enough to locate the key issue for the performance loss. To pinpoint the main effect of SWNTs on the device parameters, we applied experimental techniques that

specifically address charge generation and recombination, namely femtosecond TA spectroscopy and microsecond transient absorption (mTA) spectroscopy, transient photovoltage (TPV) and transient photocurrent (TPC). We found that enhanced bimolecular recombination and trap-limited extraction are the key factors for the PCE losses, respectively, in P3HT:PCBM and OPV48:PCBM devices. The validity of the conclusions is verified by reproducing the measured J-V curves from the experimentally determined device parameters.

4.2 Effect of SWNTs on Charge Generation

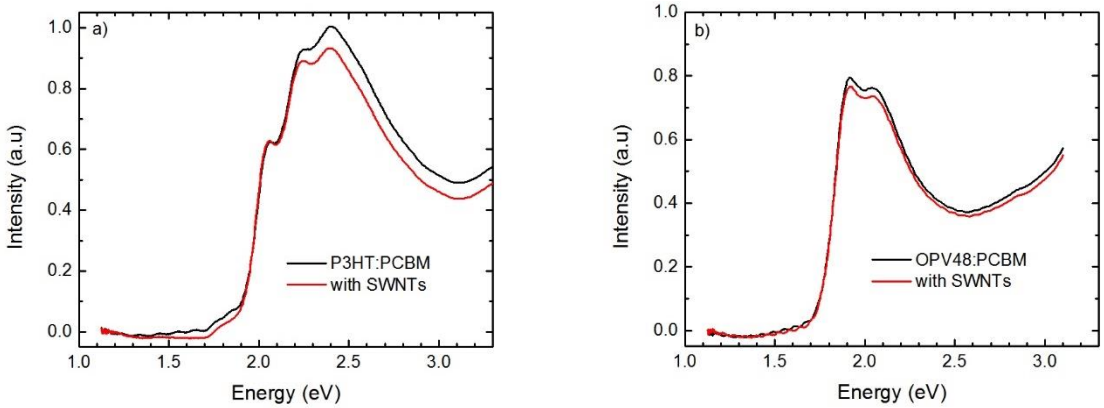

Figure 4-3. Absorption spectra taken from the P3HT:PCBM (a) and OPV48:PCBM (b) blends, respectively, with and without SWNTs

Figure 4-3 shows the absorption spectra of P3HT:PCBM (a) and OPV48:PCBM (b) blends with addition and without addition of the SWNTs. Note, the concentration of SWNTs in the blends is very low that its signal (around 1.2eV) is hidden in the noise. The absorption spectra of both P3HT:PCBM and OPV48:PCBM blends exhibit lower optical densities with the incorporation of the SWNTs. Lambert-Beer's law describes the absorption intensity as a product of wavelength dependent absorption cross-section (σ), absorbance concentration (n) and sample thickness (d). In that context, the difference in the optical density can be thought of a variation in d, as the concentration of the pristine solutions (P3HT:PCBM, OPV48:PCBM) is constant, and σ is not expected to vary upon incorporation of the small amount of SWNTs.

To clarify whether the SWNTs affects the carrier generation in the devices, femtosecond TA spectroscopy is conducted on the devices probing the excited states in a time scale from 100 femtoseconds to 400 picoseconds, covering a wavelength region from 477nm to 1600nm. The

corresponding TA spectroscopy results for both P3HT:PCBM and OPV48:PCBM devices are shown in Figure 4-4. Note, for clarity, only the TA spectra recorded at 400ps are shown, as at this time scale the TA signal mainly arises from the long-lived excited species such as charges. The complete TA spectra for all samples can be found in the appendix.

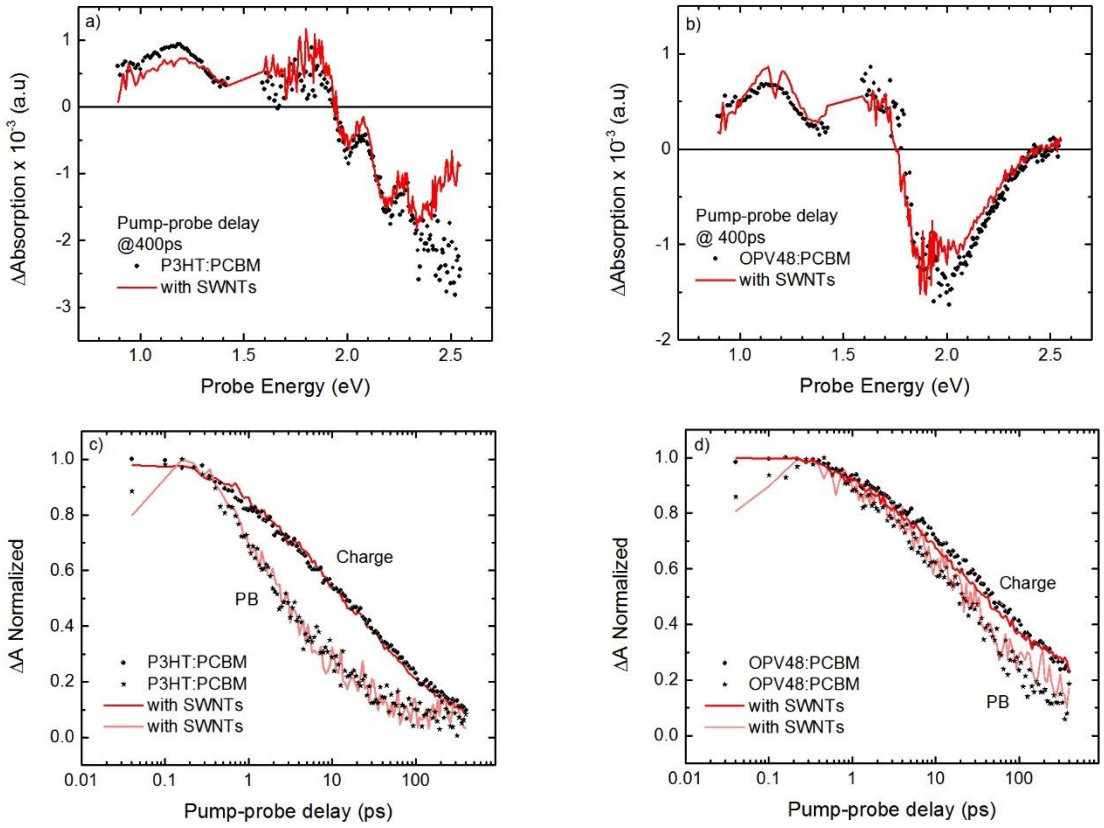

Figure 4-4. TA spectra (a,b) and corresponding charge (1.2eV) and PB (2.0eV) dynamics (c,d) in P3HT:PCBM and OPV48:PCBM devices; both samples are pumped at 2.33eV

Figure 4-4a and b show the TA spectra of P3HT:PCBM and OPV48:PCM devices, respectively, taken at a position in the middle of two finger-like cells (Figure 4-2a). Figure 4-4c and d display the corresponding dynamics of the PB (at 2.0 eV) and charge band (1.2 eV). The charge band of the donor materials in both samples is located around 1.2eV, coinciding with the PB of SWNTs. The PB of SWNTs disappears at 400ps in the P3HT:PCBM (Figure 4-4a) sample (strong PB signal is detected at early pump-probe delays, see the appendix), while it is still present in the OPV48:PCBM sample (Figure 4-4b). Note, the same amount of SWNTs is used in both devices, thus, the amount of SWNTs in the active layer has nothing to do with this observation. Again, it is not possible to detect such a strong PB signal even from a pure SWNT sample with that little amount (see absorption spectra) at this timescale. Hence, It may hint towards negligible interaction

between the excited states of SWNTs and P3HT in the P3HT:PCBM device, whereas a significant charge or long-lived excited state transfers from OPV48 towards SWNTs in the OPV48:PCBM device. The similar TA spectral shapes and seamless PB and charge dynamics in both devices (Figure 4-4c and d) with and without SWNTs reveals that SWNTs did not affect the carrier generation, at least in range of 400ps time scale. Any noticeable change on the spectral shape, on the band location and on the dynamics of charges at longer times may not be expected based on the studies on P3HT:PCBM [4-9], unless there is a considerable interaction among the excited states of polymer, PCBM and SWNTs. Nevertheless, any change in the charge density at longer times refers to processes other than generation, as the main charge generation process takes place at the donor acceptor interface in a picosecond timescale [4-9]. Therefore, we can conclude that the short circuit current loss in the device with SWNTs are not caused by the charge carrier generation loss.

4.3 Effect of SWNTs on Charge Extraction and Recombination

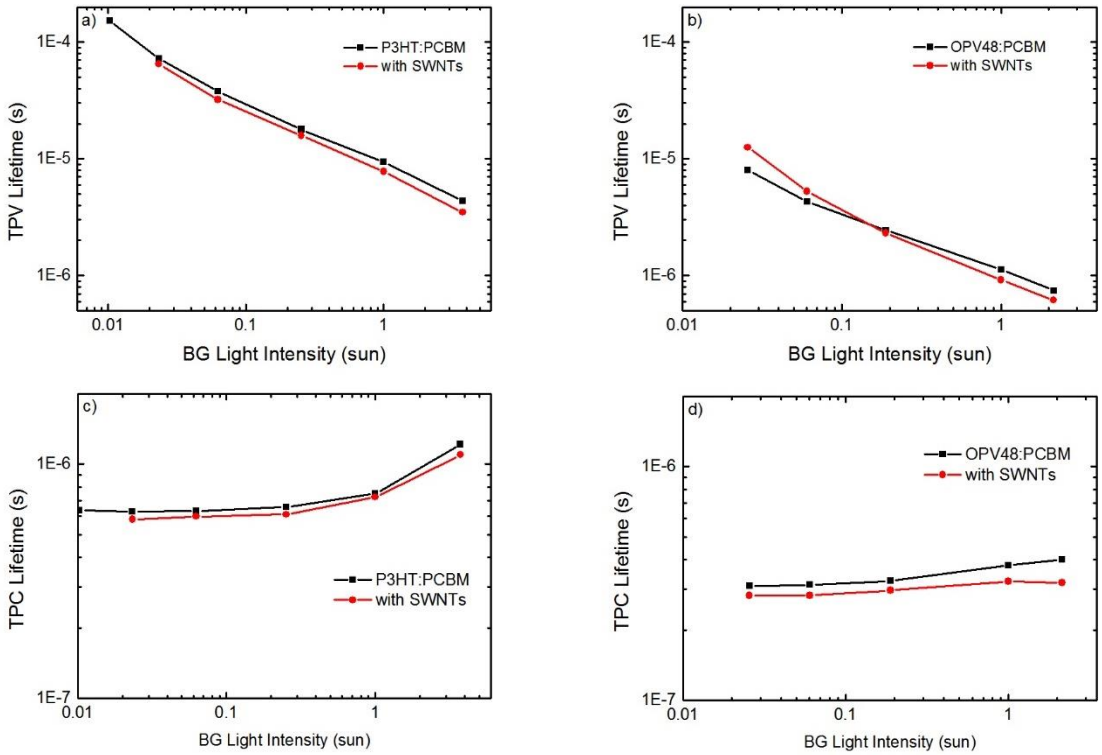

Figure 4-5. TPV (a,b) and TPC (c,d) lifetimes as a function of BG light intensity, measured on P3HT:PCBM and OPV48:PCBM device with and without SWNTs

Figure 4-5 shows the lifetimes of the TPV (a,b) and TPC (c,d) signals, recorded on P3HT:PCBM and OPV48:PCBM devices with and without SWNTs, respectively, as a function of BG light intensity. As exhibited, the presence of SWNTs slightly decreases the recombination (a,b) and extraction (c,d) times of the carriers regardless of the polymers used as electron donor material in the devices. Note, the TPV lifetime of the OPV48:PCBM device (b) is about one order of magnitude shorter than that of the P3HT:PCBM (a), and approaches to the TPC lifetime (d). A small gap between TPV and TPC lifetimes signals a carrier extraction loss in an operating device due to recombination; if it reaches a level of effecting (reducing) J_{sc} , the TPC lifetime cannot purely be regarded as the carrier extraction time of the device but the combination of extraction and recombination. It is shown in Figure 4-15(c,d) that the TPC lifetime is shorter in OPV48:PCBM device by a factor of two in contrast to the P3HT:PCBM device, which might exactly be due to the small difference between TPV and TPC lifetimes (strong recombination), or/and because of a faster hole mobility in the OPV48.

Whether the carrier recombination plays role in the device at short circuit, it can easily be examined from the BG light intensity dependence of J_{sc}. Ideally, at short circuit, the output current can be expressed as a drift current being linearly proportional to the charge density n [4-10, 4-11],

$$J_{sc} = e\mu nE \tag{4-1}$$

where e, μ, E are elementary charge, drift mobility and electric field, respectively. The charge density has been reported to increase linearly with the incident light intensity [4-12, 4-13]. However, due to a considerable carrier recombination and extraction, in some devices the linearity of the J_{sc} decreases and forms a power-law relationship with the BG light intensity [4-14],

$$J_{sc} \infty BG^{a} \tag{4-2}$$

If a approaches the unity, the carrier recombination at short circuit can be disregarded, while values of 0.75 and 0.5 can be attributed to space charge effect [4-14] and bimolecular recombination [4-15].

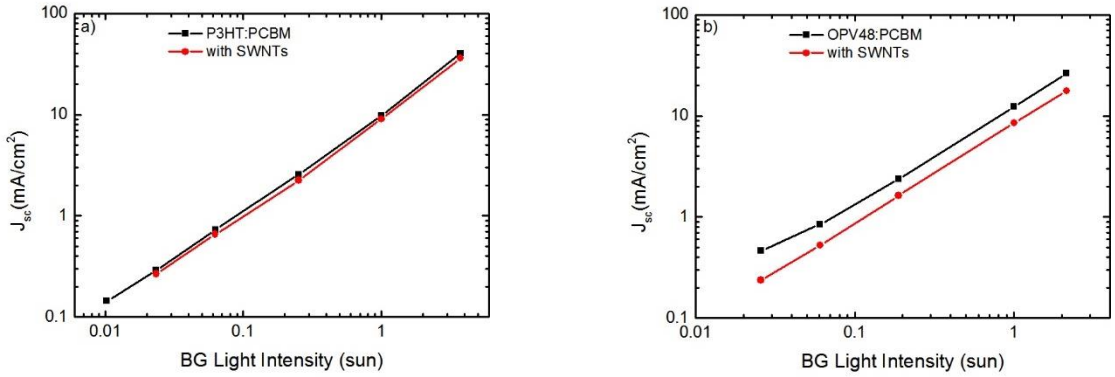

Figure 4-6. Short circuit current as a function of BG light intensity in P3HT:PCBM (a) and OPV48:PCBM (b) devices with and without SWNTs

Figure 4-16 shows the BG light intensity dependence of J_{sc} in the P3HT:PCBM (a) and OPV48:PCBM (b) devices with and without SWNTs, respectively. It shows that SWNTs does not affect much J_{sc} in P3HT:PCBM device at any BG light intensity applied in this experiment but causes a noticeable reduction in the OPV48:PCBM device. Except the OPV48:PCBM with SWNTs, the BG light intensity dependence of J_{sc} of the all devices can be fitted well by eq. (4-2) with α=1.0 (α=0.97 for OPV48:PCBM:SWNTs device, see appendix), which indicates a negligible current loss at short circuit due to carrier recombination. Therefore, the faster carrier extraction in OPV48:PCBM device can be attributed to the higher hole mobility in the OPV48.

This could be a preliminary base to judge the carrier recombination and extraction in the device, yet, the lifetime of the total charge, the corresponding bimolecular recombination coefficient as well as the charge densities at voltage points between short circuit and open circuit are needed to make a thorough conclusion.

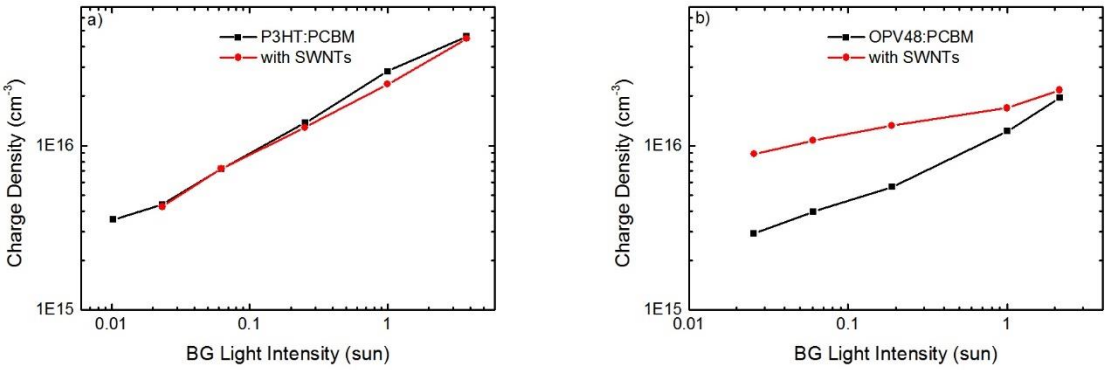

Figure 4-7. Charge density ($n(V_{oc})$) as a function of BG light intensity at open circuit, (a) in P3HT:PCBM and (b) in OPV48:PCBM devices with and without SWNTs, obtained with mTA

spectroscopy using 10^{16} cm2 for the absorption cross-section of charges and 250 nm for the active layer thickness

Figure 4-17 shows the total stationary charge density ($n(V_{oc})$) obtained via the mTA spectroscopy from P3HT:PCBM (a) and OPV48:PCBM (b) devices under various BG light intensities at open circuit, using charge absorption cross-section 10^{16} cm^2 and active layer thickness 250 nm. No significant variation of the stationary charge density is observed upon incorporation of SWNTs in the P3HT:PCBM device at all given BG light intensities, whereas a SWNTs induced drastic change in the charge density is found in OPV48:PCBM:SWNTs device, and that the stationary charge density is 2-3 times more with SWNTs in the OPV48:PCBM device. The differential charging method delivers similar values for the P3HT:PCBM with/without SWNTs as well as for the pristine OPV48:PCBM devices (except at high BG light intensities), but shows three times less charge density for the OPV48:PCBM device with SWNTs (see appendix), opposite to what is obtained from mTA spectroscopy. It is noticed already from the short TPV lifetimes and the imperfect linearity of the J_{sc} with the BG light intensity that there are significant carrier losses both at short circuit and open circuit in OPV48:PCBM:SWNTs device. The discrepancy between the values of the charge density obtained by the two different techniques can be resulted from the carrier loss in the OPV48:PCBM:SWNTs device at short circuit, which causes the under estimation of the charge density in TPV/TPC method (see experimental section).

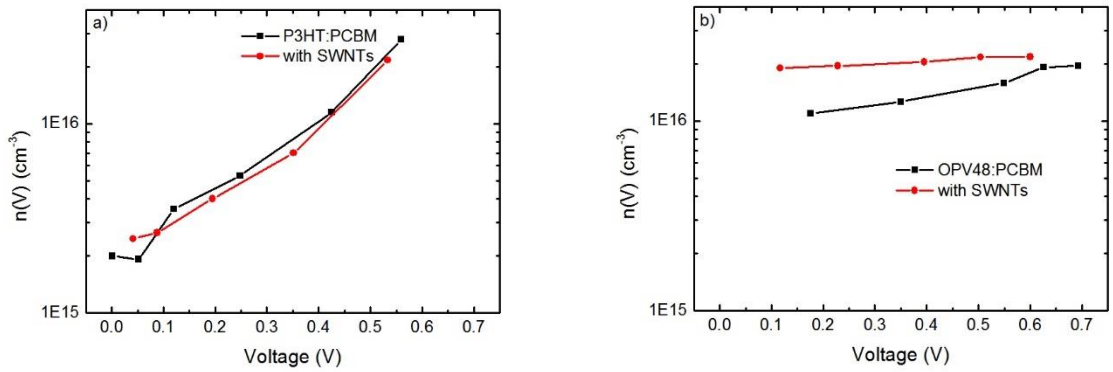

Figure 4-8. Charge density (n(V)) as a function of voltage under one sun BG illumination, (a) in P3HT:PCBM and (b) in OPV48:PCBM devices with and without SWNTs, obtained with mTA spectroscopy using 10^{16} cm2 for the absorption cross-section of charges and 250 nm for the active layer thickness

Figure 4-8 shows the non-extracted stationary charge densities at various applied voltages under constant one sun BG illumination, obtained via mTA spectroscopy (for details see experimental section). It is shown that the SWNTs does not alter the voltage dependence of the charge density

($n(V)$) in P3HT:PCBM device but introduces a huge change in the OPV48:PCBM device; the SWNTs makes charge density almost constant from open circuit to short circuit. In comparison, the charge density in P3HT:PCBM vary over a factor of 10 from short circuit to open circuit, whereas even in the pristine OPV48:PCBM device it changes only within a factor of 2. This result is also confirmed by performing the mTA spectroscopy on the device at short and open circuited conditions under multiple BG light intensities (see appendix).

Besides the charge density, the dependence of TPV lifetime on the charge density is necessary to achieve the bimolecular recombination coefficient (k_b), as introduced in the experimental section.

$$k_b = (\tau_{\Delta V_{oc}}(-S+1)n)^{-1} \quad (4\text{-}3)$$

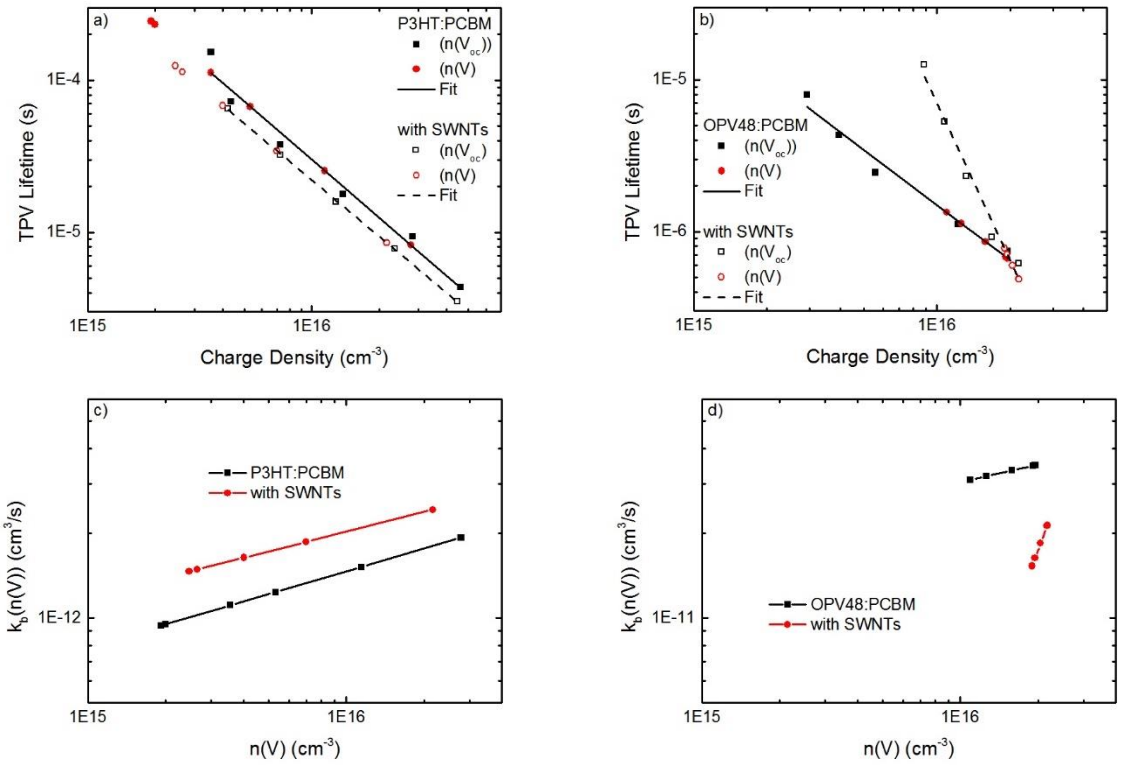

Figure 4-9. TPV lifetime (a,b) and bimolecular recombination coefficient (c,d) as a function of charge density

Figure 4-9 displace the TPV lifetimes as a function charge densities (presented in Figure 4-7 and Figure 4-18) for (a) P3HT:PCBM and (b) OPV48:PCBM devices with and without SWNTs. It is shown that the TPV lifetime always decreases linearly with the increase of charge density in all samples. However, the effect of SWNTs, on the charge density dependence of the TPV lifetime, in the OPV48:PCBM is dramatic (the slope (S) is -1.21 for the pristine device and is -3.44 for the

SWNTs included one), while its effect in the P3HT:PCBM device is trivial (the slope (S) is -1.27 for pristine device and is -1.23 for the SWNTs included one).

Figure 4-9c and d depict the bimolecular recombination coefficient $k_b(n(V))$ as a function of charge density (measured at voltage points from short circuit to open circuit under 1sun illumination) for P3HT:PCBM and OPV48:PCBM devices, respectively, with and without SWNTs (in the calculation, the voltage dependent charge density $n(V)$ presented in Figure 4-8, and the slope (S) values from Figure 4-9(a,b) are used). In the P3HT:PCBM, incorporation of SWNTs induces a significant increase in the bimolecular recombination coefficient, whereas it is just the opposite in OPV48:PCBM device. The bimolecular recombination coefficient in OPV48:PCBM device is an order of magnitude higher in contrast to that in P3HT:PCBM device, which mainly arise from the difference in the charge density.

Using the voltage dependent charge densities $n(V)$ and charge density dependent bimolecular recombination coefficient $k_b(n(V))$, now we can reconstruct the measured device current-voltage (J-V) characteristics via following relation,

$$J(V) = -J_{sc} + edk_b(n(V))n(V)^2 \tag{4-4}$$

where the active layer thickness d is 250nm. In the equation above, the measured short circuit current J_{sc} is regarded as generation current because of the negligible carrier loss at short circuit due to recombination, which cannot be true especially for the OPV48:PCBM device with SWNTs as in which the recombination is significant. Nonetheless, J_{sc} is a single constant value, and does not change the fill factor.

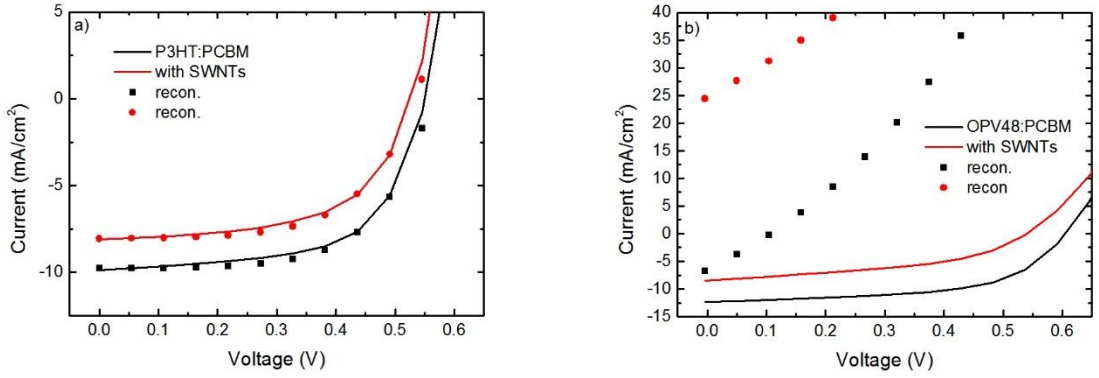

Figure 4-10. Measured and reconstructed J-V curves, represented with markers and solid lines, respectively. The reconstruction done by eq.4-4

Figure 4-10 shows the measured and reconstructed J-V curves for (a) the P3HT:PCBM and (b) the OPV48:PCBM devices with and without SWNTs. The perfect match between the measured and the reconstructed J-V curves in P3HT:PCBM devices reveals that the fill factor and that the PCE loss in the device upon incorporation of SWNTs in the active layer is mainly due to the enhanced bimolecular recombination coefficient. The SWNTs induced small gain in the carrier extraction could not overcome the recombination loss it causes.

However, the same J-V reconstruction method could not reproduce the measured J-V characteristics of OPV48:PCBM devices. It is because of the very little change in the charge density of the device from the open circuit to short circuit, see Figure 4-8b. One possible reason for that could be that the charge density measured by mTA spectroscopy with a 970nm probe beam is not purely of the charges but completely or partially of the other excited states. Organic materials including SWNTs are known to have long-lived excited states, and it has to be checked. The other possibility could be that the bimolecular recombination based model (eq. 4-4) cannot describe the charge dynamics in the OPV48 based devices, it can be tested with the drift-diffusion model [4-17, 4-18]. The nano-microsecond time dependent transient absorption spectroscopy covering the probe wavelength region from 477nm to 1500nm, and the drift diffusion model on the OPV48:PCBM devices with and without SWNTs will be our forthcoming study.

4.4 Conclusions

P3HT:PCBM and OPV48:PCBM BHJ devices were fabricated by mixing (6,5) chirality enriched SWNTs in the active layer. The J-V characteristics under standard electrical measurement conditions always showed a performance loss in the devices with SWNTs. To sort the crucial parameters out that are influenced with the SWNTs, the charge generation, extraction and recombination dynamics is studied by transient optoelectronic characterization techniques.

By performing femtosecond transient absorption spectroscopy, the effect of SWNTs on the carrier generation mechanism of the active layer is evaluated, and the carrier generation is shown to be independent of SWNT in both devices. Furthermore, TPV/TPC and mTA spectroscopy are conducted to detect any SWNT induced variations on the device parameters such as extractable and non-extractable charge density, carrier extraction and recombination, bimolecular

recombination coefficient, recombination current. Regardless of the type of the donor polymer used in the devices, the SWNTs did not improve the charge extraction much, but increased the carrier recombination significantly, specifically the bimolecular recombination coefficient. As a result, the fill factor consequently the power conversion efficiency of the device is affected negatively by SWNTs.

Our conclusions are confirmed for the P3HT based devices by reconstructing the measured J-V curves from the experimentally obtained parameters. However, the reconstruction by the same method did not succeed on the OPV48 based devices owing to either the uncertainty of the charge band in microsecond time scale or the applicability of the bimolecular recombination based model. It is concluded that the strongly diluted SWNTs did not form a well-connected nanotube network in the active layer to provide efficient percolation pathways toward electrodes but isolated islands, thus, it did not boost the charge extraction in the devices instead raised the recombination.

REFERENCES

[4-1]. Gong, Maogang, et al. "Polychiral semiconducting carbon nanotube–fullerene solar cells." *Nano letters* 14.9 (2014): 5308-5314.

[4-2]. Gong, Maogang, et al. "Understanding Charge Transfer in Carbon Nanotube–Fullerene Bulk Heterojunctions." *ACS applied materials & interfaces* 7.13 (2015): 7428-7435.

[4-3]. Jakubka, Florian, et al. "Mapping charge transport by electroluminescence in chirality-selected carbon nanotube networks." *ACS nano* 7.8 (2013): 7428-7435.

[4-4]. Abudulimu, Abasi, et al. "Chirality Specific Triplet Exciton Dynamics in Highly Enriched (6, 5) and (7, 5) Carbon Nanotube Networks." *The Journal of Physical Chemistry C* 120.35 (2016): 19778-19784.

[4-5]. Berny, Stephane, et al. "Solar Trees: First Large-Scale Demonstration of Fully Solution Coated, Semitransparent, Flexible Organic Photovoltaic Modules." *Advanced Science* (2015).

[4-6]. Credgington, Dan, et al. "Quantification of Geminate and Non-Geminate Recombination Losses within a Solution-Processed Small-Molecule Bulk Heterojunction Solar Cell." *Advanced Materials* 24.16 (2012): 2135-2141.

[4-7]. Mauer, Ralf, Ian A. Howard, and Frédéric Laquai. "Effect of nongeminate recombination on fill factor in polythiophene/methanofullerene organic solar cells." *The Journal of Physical Chemistry Letters* 1.24 (2010): 3500-3505.

[4-8]. Albrecht, Steve, et al. "On the field dependence of free charge carrier generation and recombination in blends of PCPDTBT/PC70BM: Influence of solvent additives." *The journal of physical chemistry letters* 3.5 (2012): 640-645.

[4-9]. Karuthedath, Safakath, et al. "The effect of oxygen induced degradation on charge carrier dynamics in P3HT: PCBM and Si-PCPDTBT: PCBM thin films and solar cells." *Journal of Materials Chemistry A* 3.7 (2015): 3399-3408.

[4-10]. Cowan, Sarah R., et al. "Transient photoconductivity in polymer bulk heterojunction solar cells: competition between sweep-out and recombination." *Physical Review B* 83.3 (2011): 035205.

[4-11]. Cowan, Sarah R., et al. "Charge formation, recombination, and sweep-out dynamics in organic solar cells." *Advanced Functional Materials* 22.6 (2012): 1116-1128.

[4-12]. Shuttle, C. G., et al. "Charge-density-based analysis of the current–voltage response of polythiophene/fullerene photovoltaic devices." *Proceedings of the National Academy of Sciences* 107.38 (2010): 16448-16452.

[4-13]. Shuttle, Christopher G., et al. "Measurement of Charge-Density Dependence of Carrier Mobility in an Organic Semiconductor Blend." *Advanced Functional Materials* 20.5 (2010): 698-702.

[4-14]. Koster, L. J. A., et al. "Origin of the light intensity dependence of the short-circuit current of polymer/fullerene solar cells." *Applied Physics Letters* 87.20 (2005): 203502.

[4-15]. Cowan, Sarah R., Anshuman Roy, and Alan J. Heeger. "Recombination in polymer-fullerene bulk heterojunction solar cells." *Physical Review B* 82.24 (2010): 245207.

[4-16]. Ramsdale, C. M., et al. "The origin of the open-circuit voltage in polyfluorene-based photovoltaic devices." *Journal of applied physics* 92.8 (2002): 4266-4270.

[4-17]. Koster, Lambert JA, et al. "Device model for the operation of polymer/fullerene bulk heterojunction solar cells." *Physical Review B* 72.8 (2005): 085205.

[4-18]. Laquai, Frédéric, et al. "Charge carrier transport and photogeneration in P3HT: PCBM photovoltaic blends." *Macromolecular rapid communications* 36.11 (2015): 1001-1025.

5 FIELD EFFECT TRANSISTOR MADE FROM CHIRALITY ENRICHED SWNTS

5.1 Introduction

Besides OSCs, semiconducting SWNTs are also very attractive material to the FET community due to the high charge carrier mobility, large current-carrying capacity and one-dimensional charge transport property (because of their high aspect ratio) they possess. The extraordinary carrier transport property of a SWNT first revealed in FET in 2003 [5-1]. Simulation based studies have shown that the performance of FET devices made from aligned and well-spaced SWNTs arrays can surpass the single crystalline silicon based devices [5-2, 5-3] with a two-five times higher performance or two-five times less energy consumption [5-2, 5-4]. Just recently, M. S. Arnold´s group has reported FET device made from polymer wrapped, aligned, solution based SWNT array, and demonstrated that the device, with a carrier mobility of 1130-1912 $cm^2V^{-1}s^{-1}$, perform better (almost twice) than a conventional same size single-crystalline silicon based device [5-5]. It is known that metallic tubes disturb the performance of the device by creating shorting channels. It seems that alignment of the tubes is also a great deal for improving the device performance.

However, in our case, the SWNTs are not aligned as the purpose is not to make a great FET device, but to fabricate normal working devices with the randomly distributed SWNTs and measure the field effect carrier mobility, since that is the situation in the SWNT based OSCs. Nonetheless, the chirality of the nanotubes is sorted well in a similar fashion of polymer wrapping as in [5-5] (see, experimental section for details).

5.2 Results and Discussion

5.2.1 SWNT Characterization

Figure 5-1 shows the absorption spectra of the (7,5) and (6,5) enriched SWNTs suspensions, respectively, each with three different concentrations. The chirality sorting process involved the polymer wrapping, centrifugation, filtering and sonication as described in the sample preparation section of chapter 2. The procedures are the same for both chiralities except that different polymers have been used. PFO-BPy is used for selecting the (6,5) chirality from the raw material, while for selecting the (7,5) chirality, PFO is used. The peaks around 1050 nm and 650 nm (in the absorption spectra of (7,5) rich sample) and 975 nm and 575 nm (in the absorption spectra of (6,5) rich sample)

are the first and second excitonic transition bands of the (7,5) and (6,5) tubes, respectively. The bands near to 300 nm in both spectra belong to the absorption bands of the remaining polymers, while the peaks close to 850 nm are the phonon side bands of the corresponding main tubes. The rest of the weak absorption peaks can be attributed to minor amount of other chiralities.

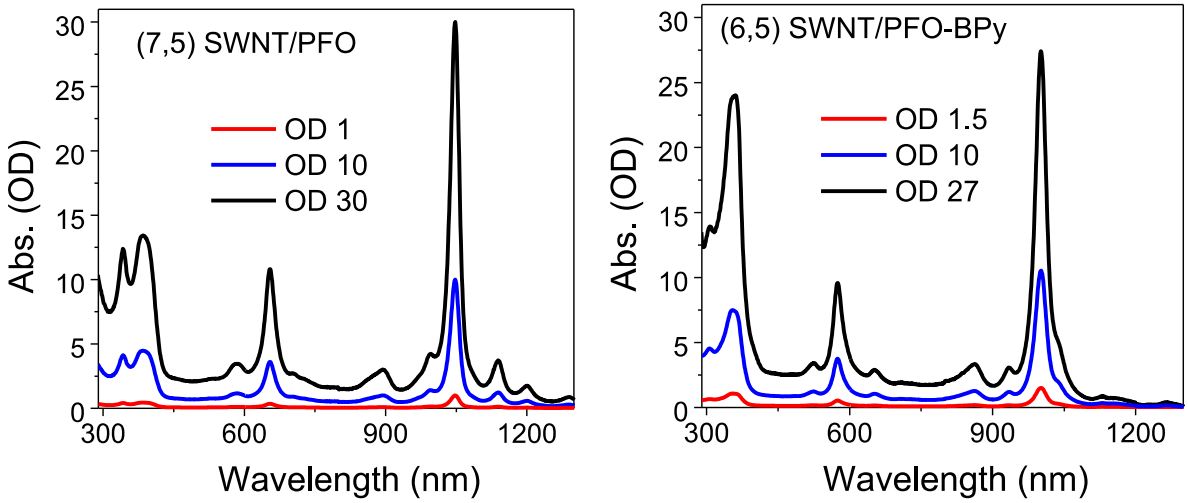

Figure 5-1. Absorption spectra of (7,5) (left) and (6,5) (right) chirality enriched SWNT suspensions with various concentrations

5.2.2 FET Surface Characterization

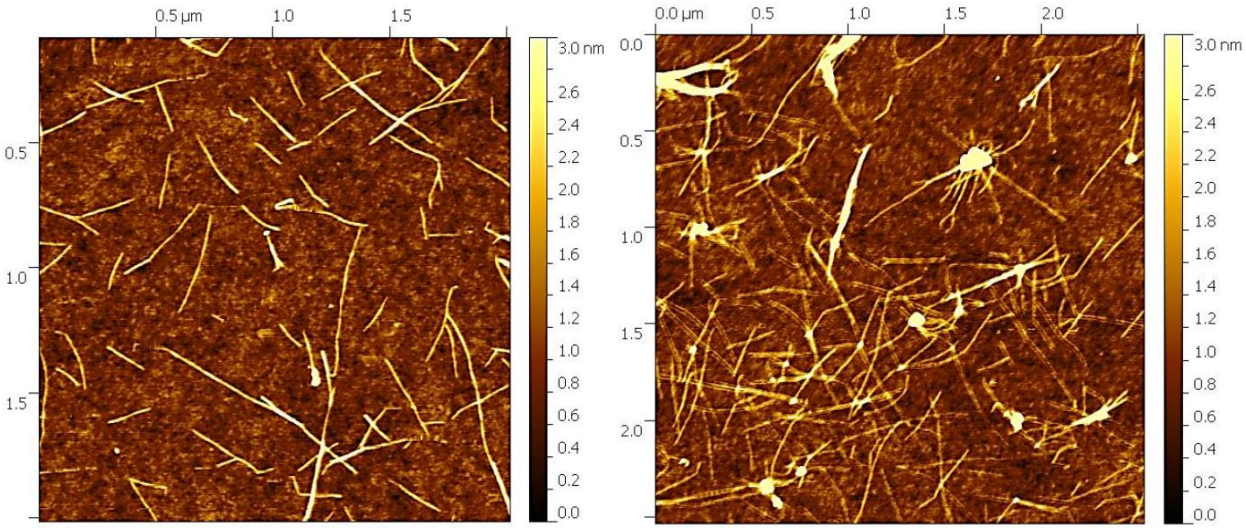

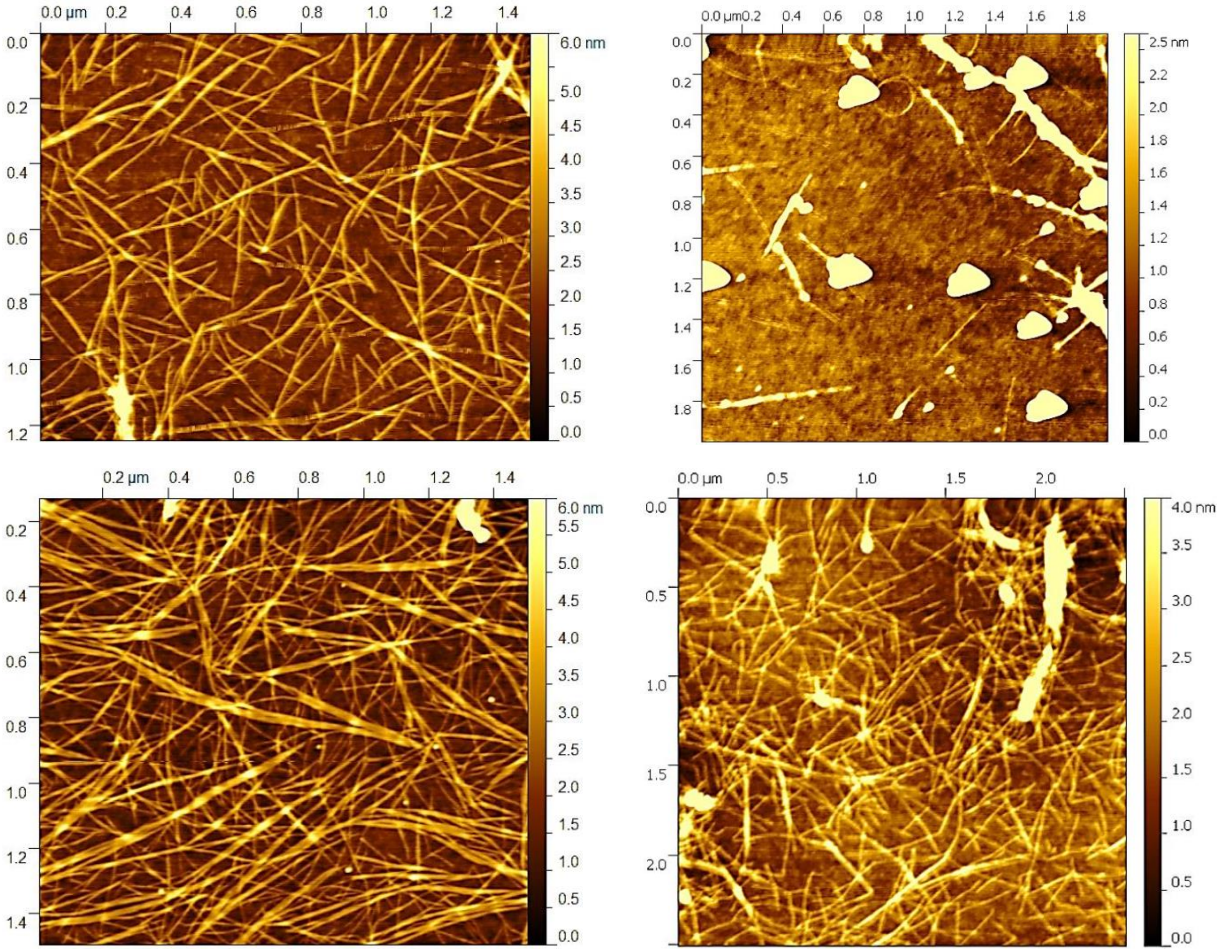

Figure 5-2. AFM images of SWNTs on Si/SiO_2 substrates, spin-casted from (7,5) (left) and (6,5) (right) suspensions with three different concentrations. Top to bottom: 1, 10 and 30OD

Surface characterization of the SWNT coated substrates is done by atomic force microscopy (AFM). Figure 5-2 shows the topography images of the randomly distributed (7,5) and (6,5) SWNTs, respectively, with various concentrations. When the SWNTs are spin-casted from the suspension with OD1, they could not make a well-connected network. From that one could expect a failure on fabricating working devices. Coverage of the substrate surface with SWNTs is improved when the nanotube suspension with 10OD is used in the case of (7,5), and devices with fare performance can be expected. In the case of (6,5), there not many SWNTs are observed but heart-shape like aggregates. That is because of the already aggregated SWNT suspensions. When the SWNT suspensions with 30OD is used, the nanotubes covered most of the substrate surface and formed well connected networks, and the best device performance can be expected.

5.2.3 FET Electrical Characterization

Devices with 10 OD (7,5) Chirality Rich SWNTs

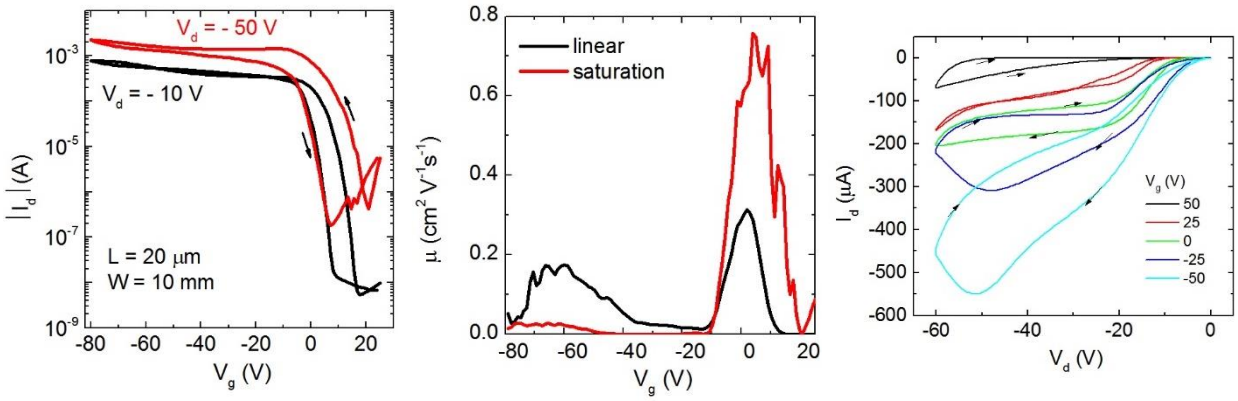

Devices with 30 OD (7,5) Chirality Rich SWNTs

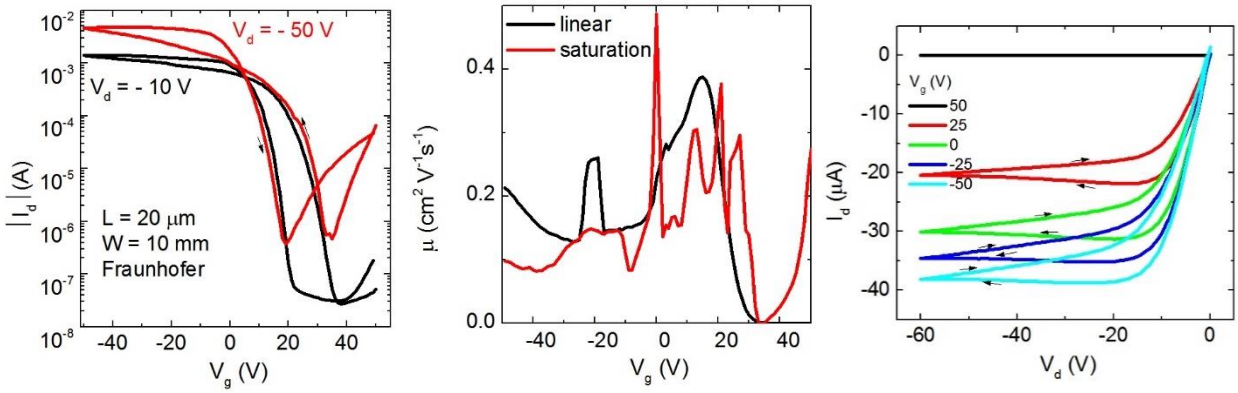

Devices with 10 OD (6,5) Chirality Rich SWNTs

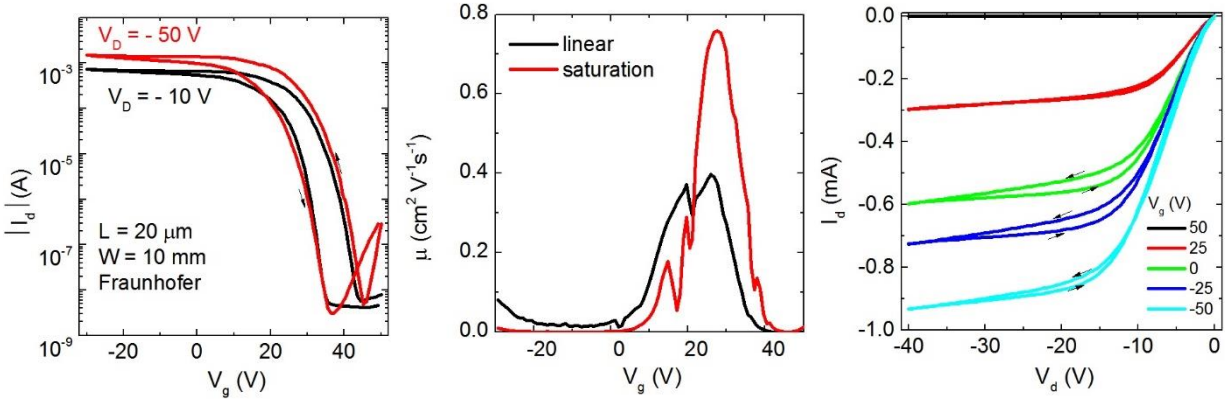

Figure 5-3. Transfer (left column), mobility (middle column) and output curves (right column) of the FETs fabricated from 10OD (7,5) rich (upper row), 30OD (7,5) rich (middle row) and 1OD (6,5) rich (lower row) SWNT suspensions

Figure 5-3 shows the transfer characteristics, mobility and output characteristics of the FET devices fabricated from (7,5) and (6,5) rich SWNT suspensions, respectively. Most of the devices made from 1OD SWNT suspension did not work, which is mainly due to the poorly formed semiconducting layer (see Figure 5-2). Devices prepared from 10OD (7,5) rich dispersion worked well, whereas the devices fabricated from (6,5) rich dispersion with similar concentration did not work at all (see appendix), which is expected already from the AFM topography images (Figure 5-2), as the 10OD (6,5) rich suspension was already aggregated when received from Wurzburg. The devices produced from both (6,5) and (7,5) SWNT dispersions with 30OD have delivered the best performance, which is, as predicted from the surface analysis, largely due to the well-connected nanotube networks on the substrate. The nanotubes almost completely covered the substrate surface.

As shown in Figure 5-3 (middle column), irrespective of tube chiralities, the maximum charge carrier mobility measured at saturation and linear regimes are approximately 0.8 $cm^2V^{-1}s^{-1}$ and 0.4 $cm^2V^{-1}s^{-1}$, respectively. It seems that the mobility does not change much with the concentration of the nanotubes once they form good enough crosslinked networks on the substrate, at least based on the results obtained from these bottom-gate-bottom-contact type of devices made from 10OD and 30OD (7,5) SWNT dispersions. Note, despite electron transfer at certain gate voltages in some devices is observed, the characteristics of the electrical conducting channel are largely dominated by the p-type carriers. Hence, the mobilities measured in these devices are attributed to the holes, which is surprising though as the semiconducting nanotubes are expected to exhibit bipolar behavior [5-6]. This discrepancy can result from the electron traps present at the SWNT/SiO^2, or from atmospheric oxidants [5-7]. Besides that, all devices show certain degree of hysteresis which can be caused by any adsorbates and water contamination on the substrate [5-8]. The current on/off ratio for the best working devices in average is around 10^5.

5.3 Conclusions

In summary, bottom-gate bottom-contact FET devices are produced from (7,5) and (6,5) chirality sorted dispersions with various concentrations, respectively, using the commercially available pre-digitalized Si/SiO_2 based substrates. Whole device fabrication as well as the electrical characterization process are carried out in a systematic procedure in a glovebox under controlled

environment. Chiral purity of the polymer wrapped SWNTs is checked by standard UV-VIS-NIR absorption spectroscopy, and confirmed that the SWNT samples are enriched in (7,5) and (6,5) chirality, respectively, no trace of metallic tubes is detected. Surface characterization is conducted with AFM, and found that the SWNTs spun from 1OD dispersions are not enough to cover the SiO_2 substrate, and does not form a uniform network to make reliable devices. SWNTs from 30OD suspensions, on the other hand, are found to create the best nanotube networks covering most parts of the substrate. The devices built from spin-casting those dense nanotube dispersions delivered the best performance compared to the rest, the hole mobility reaching 0.8 and 0.4$cm^2V^{-1}s^{-1}$ at saturation and linear operating regimes, and the current on/off ratios exceeding 10^5. However, there no significant performance difference is found between devices fabricated from (7,5) and (6,5) chirality rich dispersions.

REFERENCES

[5-1]. Javey, Ali, et al. "Ballistic carbon nanotube field-effect transistors." *nature* 424.6949 (2003): 654-657.

[5-2]. Rutherglen, Chris, Dheeraj Jain, and Peter Burke. "Nanotube electronics for radiofrequency applications." *Nature Nanotechnology* 4.12 (2009): 811-819.

[5-3]. Tulevski, George S., et al. "Toward high-performance digital logic technology with carbon nanotubes." *ACS nano* 8.9 (2014): 8730-8745.

[5-4]. Zhang, Jie, et al. "Carbon nanotube robust digital VLSI." *IEEE Transactions on Computer-Aided Design of Integrated Circuits and Systems* 31.4 (2012): 453-471.

[5-5]. Brady, Gerald J., et al. "Quasi-ballistic carbon nanotube array transistors with current density exceeding Si and GaAs." *Science Advances* 2.9 (2016): e1601240.

[5-6]. Bottacchi, Francesca, et al. "Nanoscale Charge Percolation Analysis in Polymer-Sorted (7, 5) Single-Walled Carbon Nanotube Networks." *Small*12.31 (2016): 4211-4221.

[5-7]. Bottacchi, Francesca, et al. "Polymer-sorted (6, 5) single-walled carbon nanotubes for solution-processed low-voltage flexible microelectronics." *Applied Physics Letters* 106.19 (2015): 193302.

[5-8]. Brady, Gerald J., et al. "High performance transistors via aligned polyfluorene-sorted carbon nanotubes." *Applied Physics Letters* 104.8 (2014): 083107.

6 SUMMARY AND FUTURE STUDIES

6.1 Conclusions

Possessing high charge carrier mobility and tunable bandgap properties, SWNT is believed to be one of the promising candidate materials for OSCs. Due to some known issues related to mixed chiralities, first of all, very pure (6,5) and (7,5) SWNT chiralities are sorted by applying a series of purification techniques. Then, fundamental photophysical properties of SWNTs are studied focusing on identifying possible excited state species and their time dependent concentrations, and the transient absorption (TA) dynamics of (6,5) and (7,5) rich SWNT networks on a femtosecond to microsecond time scale are presented. Because of the very congested spectral features in the TA spectra of SWNTs, a global analysis is performed on the TA spectra using spectral shapes from the absorption, photoluminescence and spectroelectrochemical studies. By introducing a new method for tracing excited state species that reside outside the pump-probe measurement window, presence of an excess photobleach in the TA spectra of both samples are observed besides singlets, charges, trions and phonon side bands, which can neither be assigned to the singlet excitons nor to the charged states. These excess photobleaches with microseconds of lifetimes are assigned to triplet excitons, and reported for the first time the occurrence of triplet exciton transfer from the (6,5) to the (7,5) chirality on a 70ps time scale. By comparing samples with different SWNT densities and varying the pump intensity, it is found that singlet exciton relaxation is the most probable scenario for triplet exciton generation in SWNTs.

In order to get some information about the field effect carrier mobility in the bulk semiconducting nanotube films, SWNTs based FET devices are fabricated on commercially available pre-digitalized Si/SiO2 substrates, and are characterized by electrical and morphological techniques. Field effect carrier mobility of both (6,5) and (7,5) semiconducting SWNTs is found to be approximately in the range of 0.4-0.8 $cm^2V^{-1}s^{-1}$, and the attained carrier mobility is turned out to be of the holes. The measured current on/off ratio reached to 10^5 in the best performing devices. Surface characterization with AFM showed that the spin-casted SWNTs spread on the substrates very randomly, and tend to form aggregation sites. The random distribution of SWNTs often leads to failure of a successful device fabrication by not creating a well-connected network when a diluted SWNT dispersion is used, or by creating shorts in the device when a highly concentrated SWNT dispersion is used. The random distribution of the SWNTs on the substrate can be one of the main reasons for the 10^4 times less carrier mobility measured in the device presented in this

these, in contrast to the recently published results by another group on the aligned and well-spaced SWNTs.

Thereafter, P3HT:PCBM bulk hetero junction OSC devices are fabricated in a well-controlled fabrication system by integrating the chirality sorted SWNTs in the active layer of the devices, and the effect of SWNTs on the device's performance is tested under the standard electrical characterization condition. J-V characteristics showed that the OSC devices with SWNTs perform worse in contrast to the devices without them. To rationalize the findings, a set of OPV48:PCBM devices with/without SWNTs are fabricated in similar fashion, and similar results are obtained. In order to get specific information about the effect of SWNTs on the device's properties and find more precise answer for the fill factor and performance loss in the devices with SWNTs, measurement techniques such as femtosecond TA spectroscopy, TPV/TPC and microsecond TA spectroscopy are conducted on the complete devices.

SWNTs with the concentration of less than 0.1% (weight ratio, high concentration leads to shorting the device) helps little the charge extraction in the P3HT:PCBM devices reported herein but increases the bimolecular recombination coefficient significantly. Basically, SWNTs do not do what is expected them to do—helping the carrier extraction with their high charge transport properties, but instead increase the carrier recombination. It is proposed that the very diluted SWNTs do not form a uniform network in the active layer to successfully transport the collected charge carriers to the electrodes, but in opposite they form isolated islands and helps the carrier recombination.

6.2 Outlook

From the SWNT side, the sample preparation method should be improved. The procedures described in the experimental section and applied for the preparation of the SWNTs samples presented in this thesis is very time consuming (takes at least two days to get 200μL SWNTs). The long sonication time could also lead to creation of damages and traps on the nanotubes, which could have crucial impact on the excited state dynamics of SWNTs as well as on the performance of OSC devices. Also, the residuals left from the dilution of nanotube loaded filters, if not removed completely, could bring complications to the characterization of SWNT photophysics, as well as

some undesired effects on the device's performance. Nevertheless, we have been informed by our collaborator that there are already some improvements on the sample preparation method, like changing the tip sonication procedures to shear mixing, which is said to reduce the damages to the SWNTs.

About the excited state dynamics of SWNTs, we have covered quite a range of the spectrum (from 477nm to 1600nm) and time scales (from 100 femtoseconds to 50 microseconds), but still could not find the exact location of the triplet state. It is important to know such an information from the science and practical application perspectives. Therefore, microwave experiment with high signal sensitivity could be done. We have confirmed the triplet exciton transfer from (6,5) chirality to (7,5) chirality, but did not observe such a phenomenon between (7,5) to (8,4), and conclude that such a triplet transfer mechanism requires a certain offset between tube diameters or band gaps. However, it should be confirmed for many more chiralities. Another important point to mention is that the spectral shape of the TA spectra in the microsecond range is a bit peculiar. The trion band is blue shifted, but the charge band is red shifted and very sharp, also the PB of (6,5) rich sample is very broad. The broad PB can be explained by the closely located (6,5) and (7,5) PBs in the (6,5) rich sample. The red shift in the location of charge band could also be explained by the renormalization energies of the charges, and the sharpness of it by the stark effect and recovered PB of (9,1) tubes which sits just on top of the charge band of (6,5) chirality. The stark effect is a phenomenon in which an electric field, induced by a charge, affects the transition energy of a nearby tube, and results in a first order derivative like spectral shape. However, the blue shift of trion band is hard to explain. Different excitation energies could bring some changes to the spectral shapes in TA spectra; for example, we excited the sample at 387nm in the picosecond time range, but at 532nm in nano-microsecond range due to our equipment limitation. It might be worthy to check it up at various pump energies.

Regarding to the OSC devices with SWNTs, the devices with SWNTs performed worse most of the time due to the increased bimolecular recombination coefficient, but without any significant improvement in carrier extraction. Very diluted SWNT dispersions are used in the OSC devices presented in this thesis, as the random distribution of the tubes is prone to short the devices at higher concentration. However, to reach their potential in the OSC devices, a uniform SWNTs network—a better charge carrier percolation pathways, should be created by providing enough

SWNTs. Aligning the SWNTs may prevent devices being shorted when the tube concentration is increased. The same examination tasks, done in this work, should also be performed on the devices in which SWNTs are used as donor, acceptor and electrodes. One more thing that I would like to mention is that none of the measurement techniques available out there can alone measure parameters of an OSC device at standard working conditions. Some use high excitation power, some measure at open or short circuit conditions. Some run into indirect ways to get specific device's parameters. The TPV/TPC integrated with the microsecond TA spectroscopy is great technique. However, it is still not good enough for the devices very sensitive to the light intensity and measurement time, e.g. perovskite; because the TA spectroscopy measurement at low light intensity or at applied voltages closer to short circuit takes longer time to overcome the noise. The community still needs an automated quick measurement technique that is able to measure all the experimental parameters that are necessary to reproduce the J-V curve of a device.

7 SUMMARY AND FUTURE STUDIES

7.1 Conclusiones

Poseyendo una alta movilidad de portadores de carga y propiedades bandgap sintonizables, SWNT se cree que es uno de los materiales candidatos prometedores para OSC. Debido a algunos problemas conocidos relacionados con las quiralidades mixtas, las primeras, las quiralidades SWNT muy puras (6,5) y (7,5) se clasifican aplicando una serie de técnicas de purificación. En segundo lugar, se estudian las propiedades fotofísicas fundamentales de los SWNTs centrándose en la identificación de posibles especies de estado excitado y sus concentraciones dependientes del tiempo y la dinámica de absorción transitoria (TA) de redes SWNT ricas en (6,5) y (7,5) en un femtosegundo a microsegundo Escala de tiempo. Debido a las características espectrales muy congestionadas en los espectros TA de SWNTs, se realiza un análisis global sobre los espectros TA utilizando formas espectrales de la absorción, fotoluminiscencia y un estudio espectroeléctrico recientemente publicado. Al introducir un nuevo método para localizar especies de estado excitado que residen fuera de la ventana de medición de la sonda de bombeo, se observó la presencia de un exceso de fotobloqueo en el espectro de TA de ambas muestras además de singlets, cargas, triones y bandas laterales de fonón que no pueden ser Asignado a los excitones de singlete ni a los estados cargados. Estos excesos de fotoblanqueo con microsegundos de vidas se asignan a excitones triplete, y se informa por primera vez la ocurrencia de la transferencia de excitones triplete de la quiralidad (6,5) a la (7,5) en una escala de tiempo de 70ps. Comparando muestras de diferente densidad de SWNT y variando la intensidad de la bomba, se encuentra que la difusión de excitones de singlete a los estados de defecto no es el escenario más probable para la generación de excitones de tripletes en SWNTs sino la relajación de excitones de singlete.

Para obtener información sobre la movilidad del portador de efectos de campo en las películas de nanotubos semiconductores a granel, se fabrican y caracterizan en el grupo de Thomas Anthopoulos los dispositivos FET de contacto de fondo con fondo de fondo de la SWNT en sustratos de Si / SiO2 pre digitalizados comercialmente disponibles En el Imperial College de Londres. La movilidad del portador de efecto de campo de los SWNTs semiconductores (6,5) y (7,5) se encuentra aproximadamente en el intervalo de 0,4-0,8 cm2V-1s-1, y la movilidad del portador alcanzada es de los orificios . La relación de activación / desactivación de la corriente medida alcanzó los 105 en los dispositivos de mejor rendimiento. Caracterización de la superficie con AFM mostró que el spin-casted SWNTs difusión sobre los sustratos muy al azar, y tienden a

formar sitios de agregación. La distribución aleatoria de SWNTs a menudo conduce al fracaso de una fabricación de dispositivo exitosa si se utiliza una dispersión de SWNT menos densa, al no crear una red bien conectada, o mediante la creación de cortocircuitos en el dispositivo si se utiliza una dispersión SWNT altamente concentrada. La distribución aleatoria de los SWNTs en el sustrato puede ser una de las razones principales por las que obtuvimos 104 veces menos movilidad de portadores en contraste con los resultados publicados recientemente por otro grupo en SWNTs alineados y bien espaciados.

Después, los dispositivos de OSC de hetero-unión de P3HT: PCBM son fabricados en un sistema de fabricación bien controlado integrando los SWNTs clasificados por quiralidad en la capa activa de los dispositivos y el efecto de SWNTs en el rendimiento del dispositivo es probado bajo la condición de caracterización eléctrica estándar . Las características J-V mostraron que los dispositivos OSC con SWNTs funcionan peor en contraste con los dispositivos sin ellos. Para racionalizar si ese resultado es el mismo también para otros dispositivos basados en polímeros, el rendimiento de un conjunto de dispositivos OPV48: PCBM con SWNT se prueba y se observa el mismo resultado. Con el fin de obtener información más específica sobre el efecto de SWNTs en las propiedades del dispositivo y encontrar una respuesta más precisa para el factor de relleno y la pérdida de rendimiento en los dispositivos con SWNTs, técnicas de medición como el femtosecond TA espectroscopia, TPV/TPC y microsecond TA espectroscopia son Realizados en los dispositivos completos.

Los SWNTs con una concentración inferior al 0,1% (relación en peso, alta concentración conduce a cortocircuitar el dispositivo) ayuda poco a la extracción de carga en los dispositivos P3HT: PCBM descritos en este documento, pero incrementa significativamente la recombinación bimolecular (de manera precisa, el coeficiente de recombinación) La recombinación inducida por la trampa. Sin embargo, no afectan mucho el orden de recombinación en los dispositivos, y el principal mecanismo de recombinación en condiciones de circuito abierto es bimolecular. Básicamente, los SWNT no hacen lo que se espera que hagan, ayudando a la extracción del portador con sus propiedades de transporte de alta carga, sino que aumenten la recombinación del portador. La explicación podría ser que los SWNTs muy diluidos no forman una red uniforme en la capa activa para transportar con éxito los portadores de carga recogidos a los electrodos, pero en opuesto forman islas aisladas y ayudan a la recombinación portadora.

7.2 Perspectivas

Desde el lado SWNT, el método de preparación de la muestra debe ser mejorado. Los procedimientos descritos en la sección experimental y aplicados para la preparación de muestras SWNTs presentadas en esta tesis, consumen mucho tiempo (tardan al menos dos días en obtener SWNTs de 200 μL). El largo tiempo de sonicación también podría conducir a la creación de daños y trampas en los nanotubos, lo que podría tener un impacto crucial en la dinámica del estado excitado de SWNTs, así como en el rendimiento de los dispositivos OSC. Además, los residuos que quedan de la dilución de los filtros cargados con nanotubos, si no se eliminan completamente, podrían traer complicaciones a la caracterización de la fotofísica SWNT, así como algunos efectos no deseados sobre el rendimiento del dispositivo. Sin embargo, hemos sido informados por nuestro colaborador que hay algunas mejoras en el método de preparación de muestras, como cambiar los procedimientos de sonicación de punta a mezcla de corte, lo que se dice reduce los daños a los SWNTs.

En cuanto a la dinámica de estado excitado de SWNTs, hemos cubierto una amplia gama del espectro (de 477nm a 1600nm) y escalas de tiempo (de 100 femtosegundos a 50 microsegundos), pero aún no pudo encontrar la ubicación exacta del estado triplete. Es importante conocer tal información desde la ciencia y las perspectivas de aplicación práctica. Por lo tanto, experimento de microondas con alta sensibilidad de señal debe hacerse. Hemos confirmado la transferencia de excitones triplete de quiralidad (6,5) a quiralidad (7,5), pero no observamos tal fenómeno entre (7,5) a (8,4), y concluimos que tal mecanismo de transferencia triple Requiere un cierto desplazamiento entre los diámetros de los tubos o los huecos de la banda. Sin embargo, debe confirmarse para muchas más quiralidades. Otro punto importante a mencionar es que la forma espectral de los espectros de TA en el rango de microsegundos es un poco peculiar. El azul de la banda de trion se desplaza, pero la banda de carga es roja cambiada y muy aguda, también el PB de (6,5) muestra rica es muy amplia. El PB amplio puede explicarse por los PB situados de cerca (6,5) y (7,5) en la muestra rica (6,5). El cambio rojo en la localización de la banda de carga también podría ser explicado por las energías de renormalización de las cargas, y la nitidez de la misma por el efecto crudo y PB recuperado de (9,1) tubos que se encuentra justo encima de la banda de carga de (6,5) quiralidad. El efecto estelar es un fenómeno que un campo eléctrico inducido por una carga afecta a la energía de transición de un tubo cercano y da como resultado una derivada de

primer orden como las formas espectrales. Sin embargo, el cambio azul de la banda de triones es difícil de explicar. Diferentes energías de excitación podrían traer algunos cambios a las formas espectrales en el espectro TA; Por ejemplo, excitamos la muestra a 387nm en el intervalo de tiempo de picosecond, pero a 532nm en rango de nano-microsegundos debido a nuestra limitación de equipo. Podría ser digno de comprobarlo en varias energías de la bomba.

Con respecto a los dispositivos OSC con SWNTs, los dispositivos con SWNTs se comportaron peor la mayor parte del tiempo debido al aumento del coeficiente de recombinación bimolecular, pero sin ninguna mejora significativa en la extracción de portadores. Dispersiones de SWNT muy diluidas se utilizan en los dispositivos OSC presentados en esta tesis, ya que la distribución aleatoria de los tubos es propensa a cortar los dispositivos a mayor concentración. Pero para alcanzar su potencial en los dispositivos OSC, una red SWNTs uniforme-se debe crear una mejor vía de percolación de portadores de carga proporcionando suficientes SWNTs. Al alinear los SWNT puede evitar que los dispositivos se cortocircuiten cuando se aumenta la concentración del tubo. Las mismas tareas de examen realizadas en este trabajo también deben realizarse en los dispositivos en los que se utilizan SWNT como donante, aceptor y electrodos. Una cosa más que me gustaría mencionar es que ninguna de las técnicas de medición disponibles por ahí solo puede medir parámetros de un dispositivo OSC en condiciones de trabajo estándar. Algunos utilizan alta potencia de excitación, algunos miden en condiciones de circuito abierto o cortocircuito. Algunos se ejecutan en formas indirectas para obtener los parámetros del dispositivo específico. El TPV / TPC integrado con el microsecond TA espectroscopia es una gran técnica. Sin embargo, todavía no es lo suficientemente bueno para los dispositivos que son muy sensibles a la intensidad de la luz y el tiempo de medición, p. Perovskita; Porque la medición de la espectroscopia TA con baja intensidad de luz o con tensiones aplicadas más próximas al cortocircuito toma más tiempo para superar el ruido. La comunidad todavía necesita una técnica de medición rápida automatizada que sea capaz de medir todos los parámetros experimentales necesarios para reproducir la curva J-V de un dispositivo.

APPENDIX

Transient Electrical Studies

P3HT:PCBM OSC

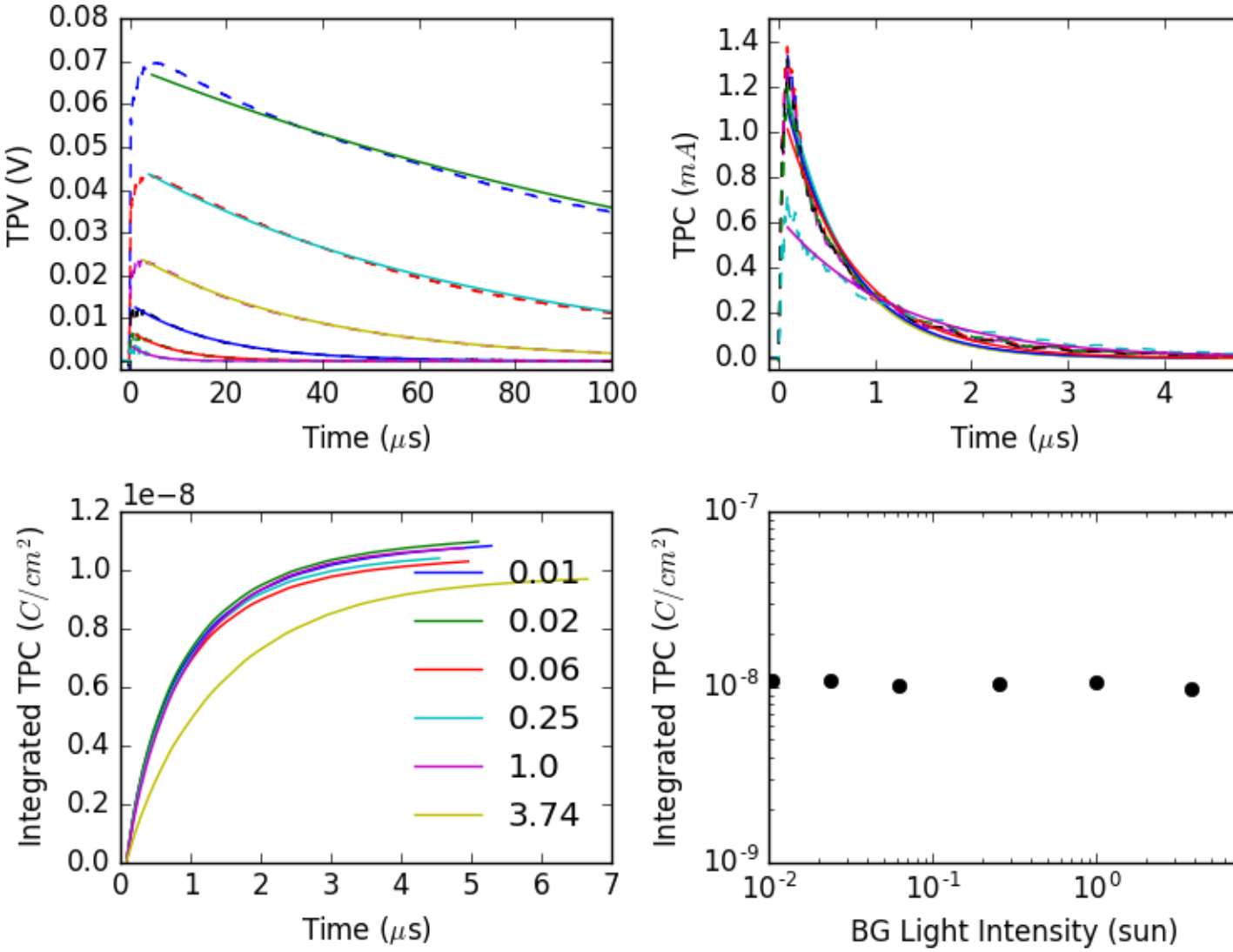

Figure 7-1. TPV (b) TPC traces, and (c,d) integrated TPC, as a function of BG light intensity (0.02-3.74 suns)

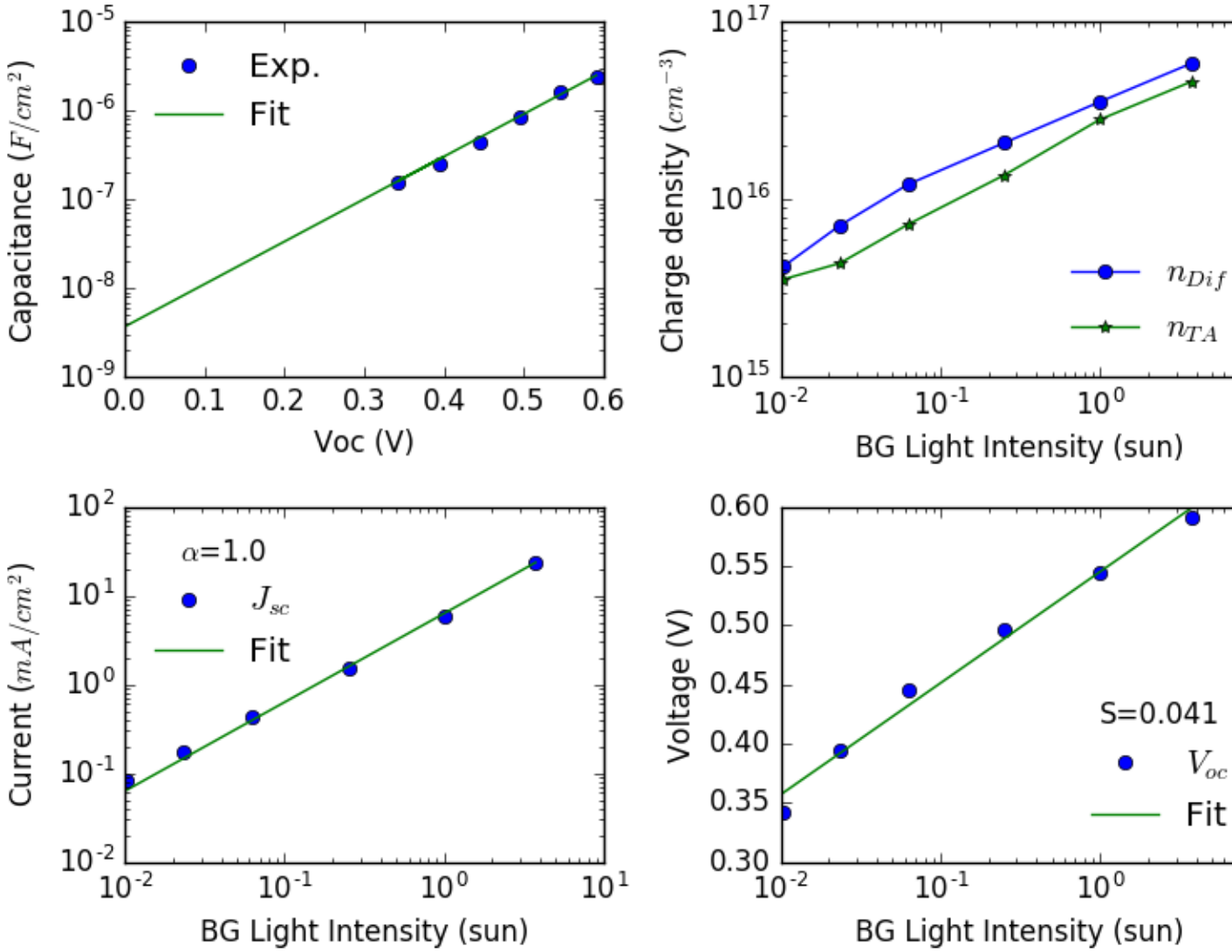

Figure 7-2. (a) Differential capacitance as a function of open circuit voltage; (b) charge density (c) short circuit current (d) open circuit voltage as a function of BG ground light intensity, respectively

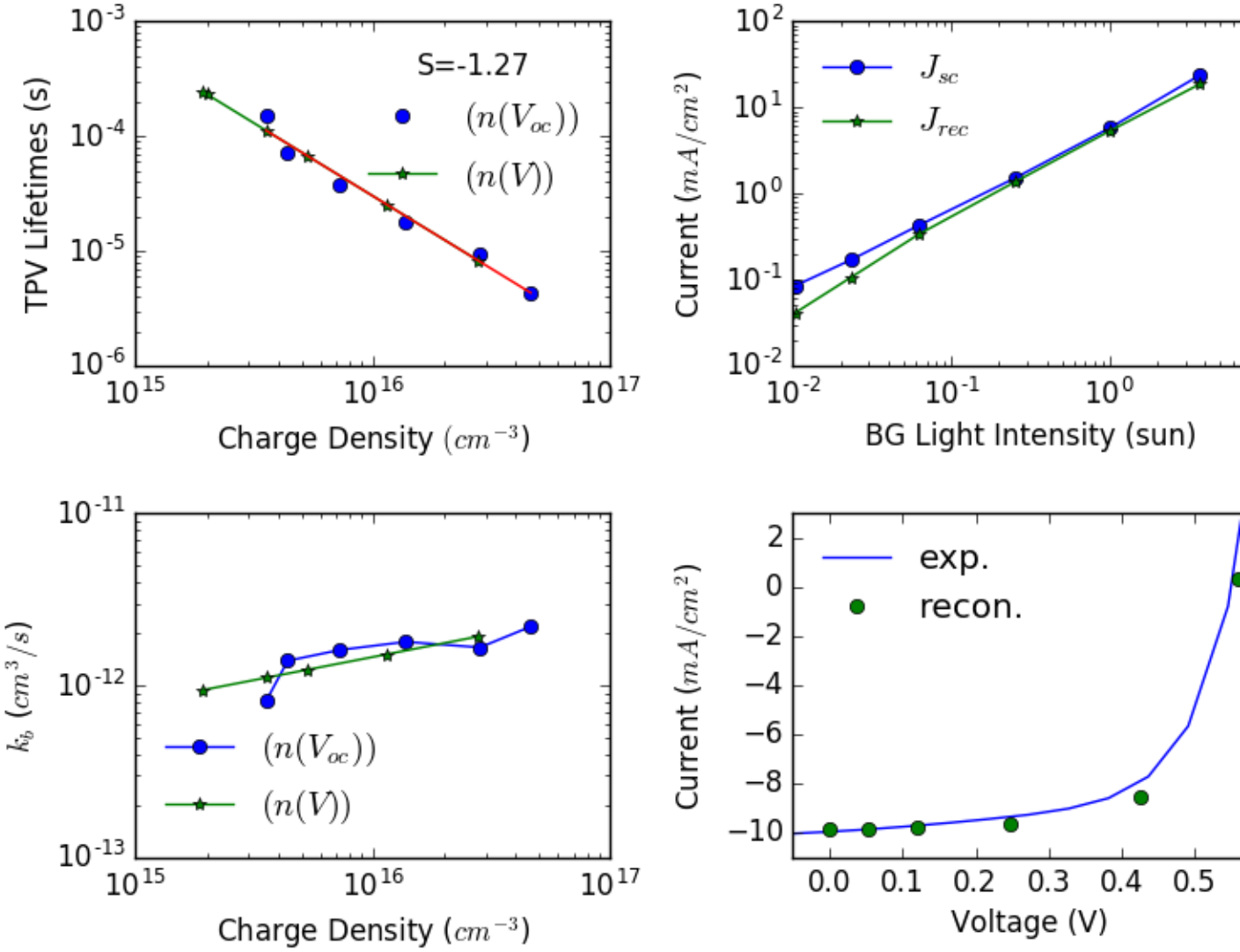

Figure 7-3. TPV lifetime as a function of charge density; (b) short circuit and recombination current density (c) bimolecular recombination coefficient as a function of BG ground light intensity, respectively; (d) measured and reconstructed J-V curves

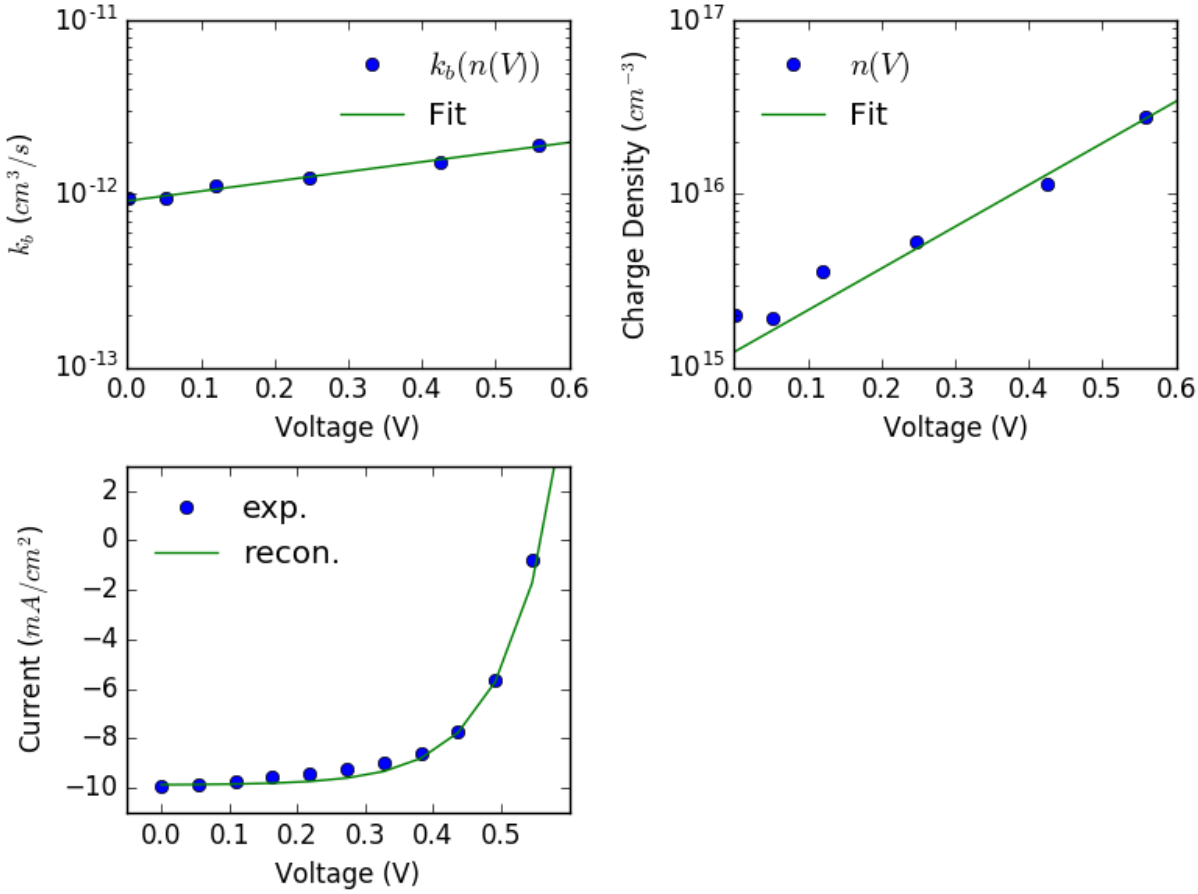

Figure 7-4. (a) Bimolecular recombination coefficient (b) charge density (c) measured and reconstructed J-V curves as a function of n and $n(V)$

P3HT:PCBM:SWNT OSC

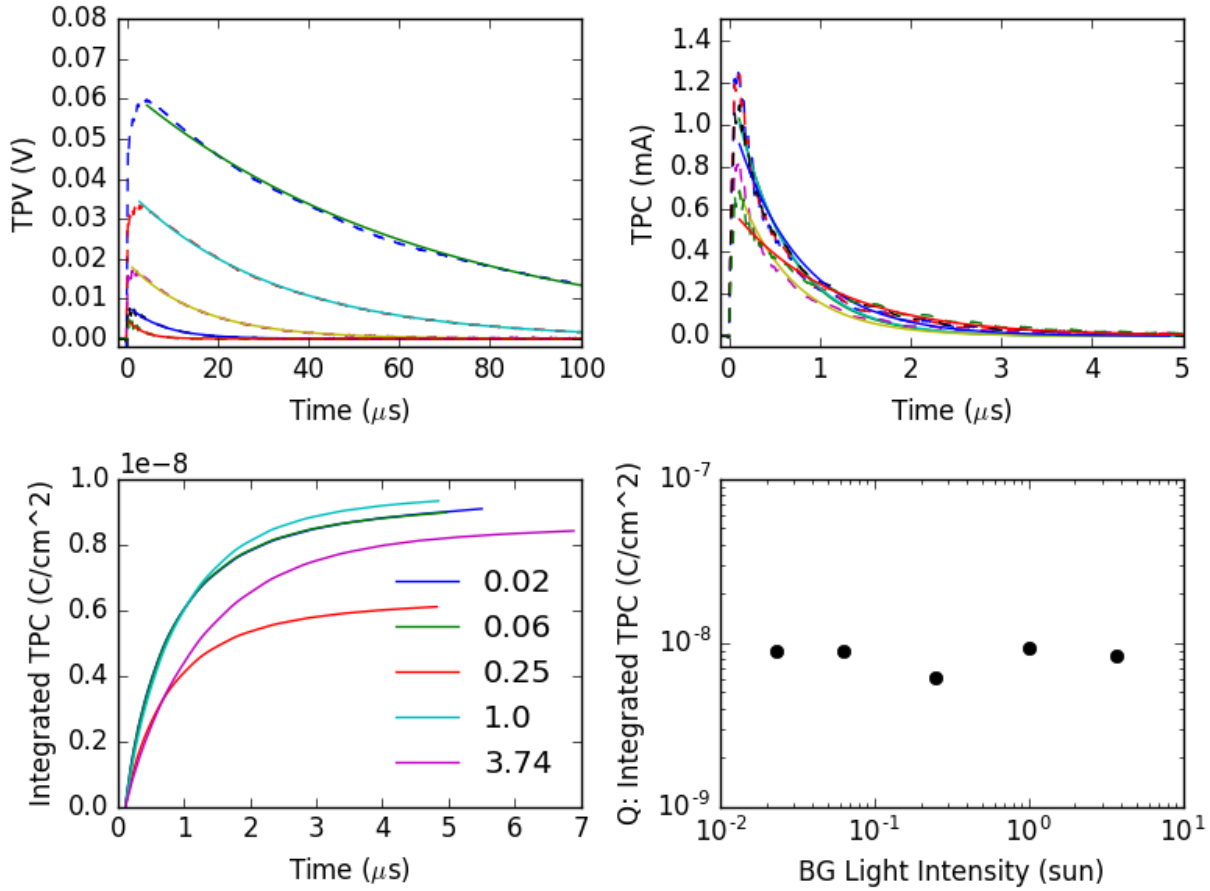

Figure 7-5. (a) TPV (b) TPC traces, and (c,d) integrated TPC, as a function of BG light intensity (0.02-3.74 suns)

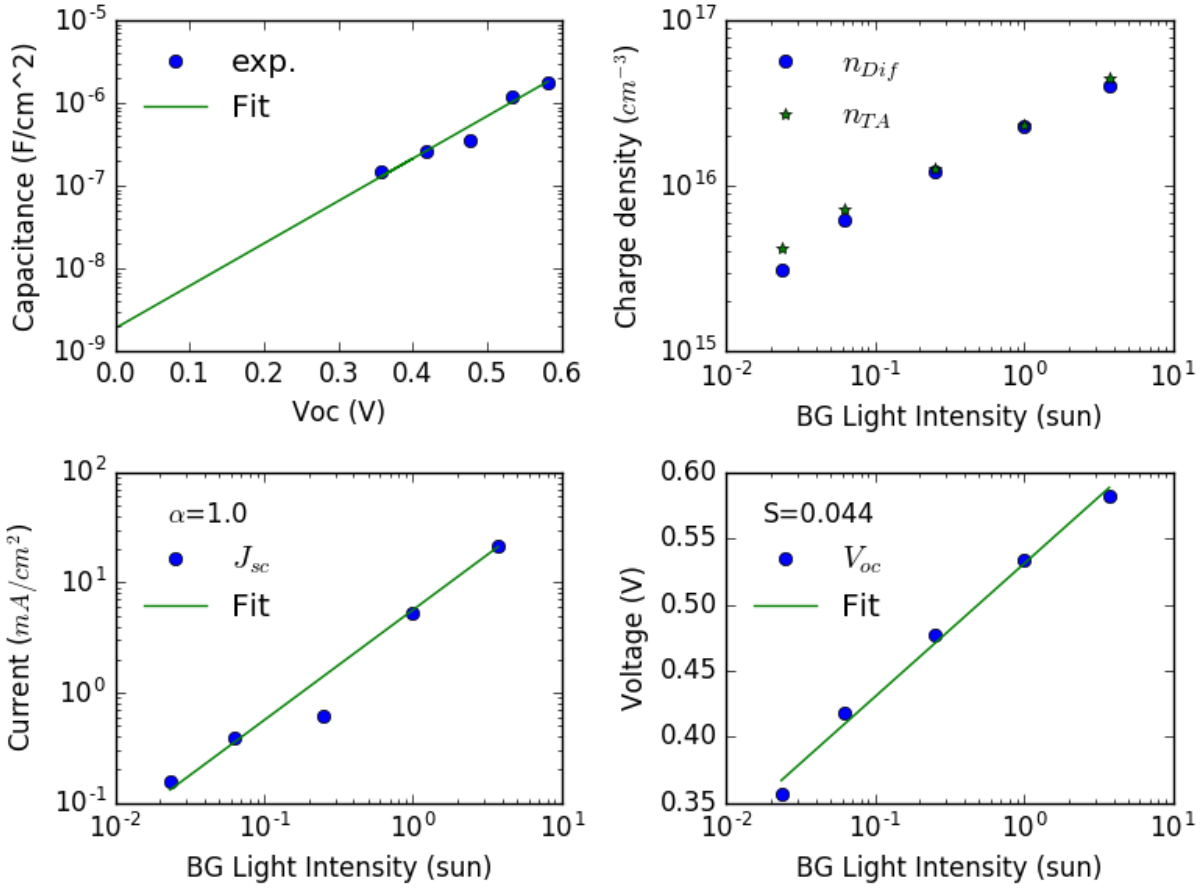

Figure 7-6. (a) Differential capacitance as a function of open circuit voltage; (b) charge density (c) short circuit current (d) open circuit voltage as a function of BG ground light intensity, respectively

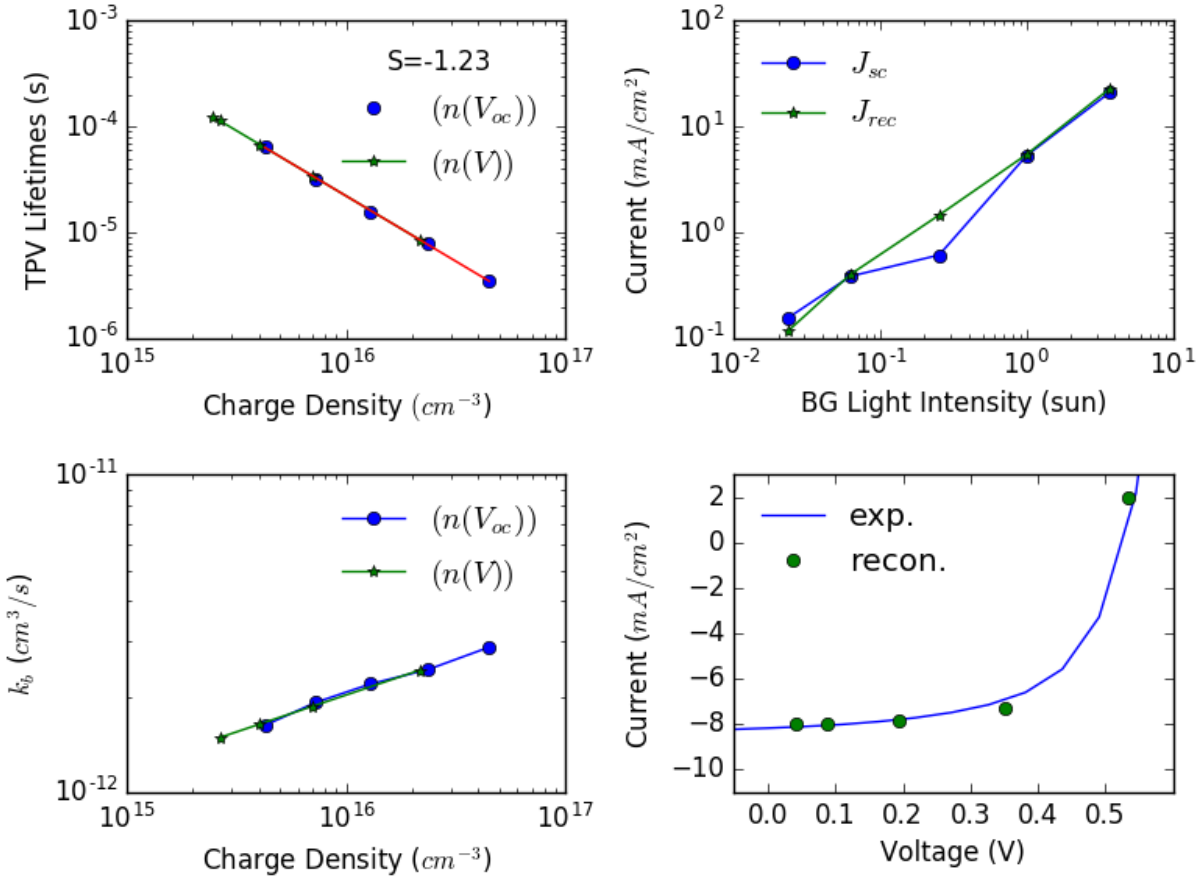

Sv=

Figure 7-7. TPV lifetime as a function of charge density; (b) short circuit and recombination current density (c) bimolecular recombination coefficient as a function of BG ground light intensity, respectively; (d) measured and reconstructed J-V curves

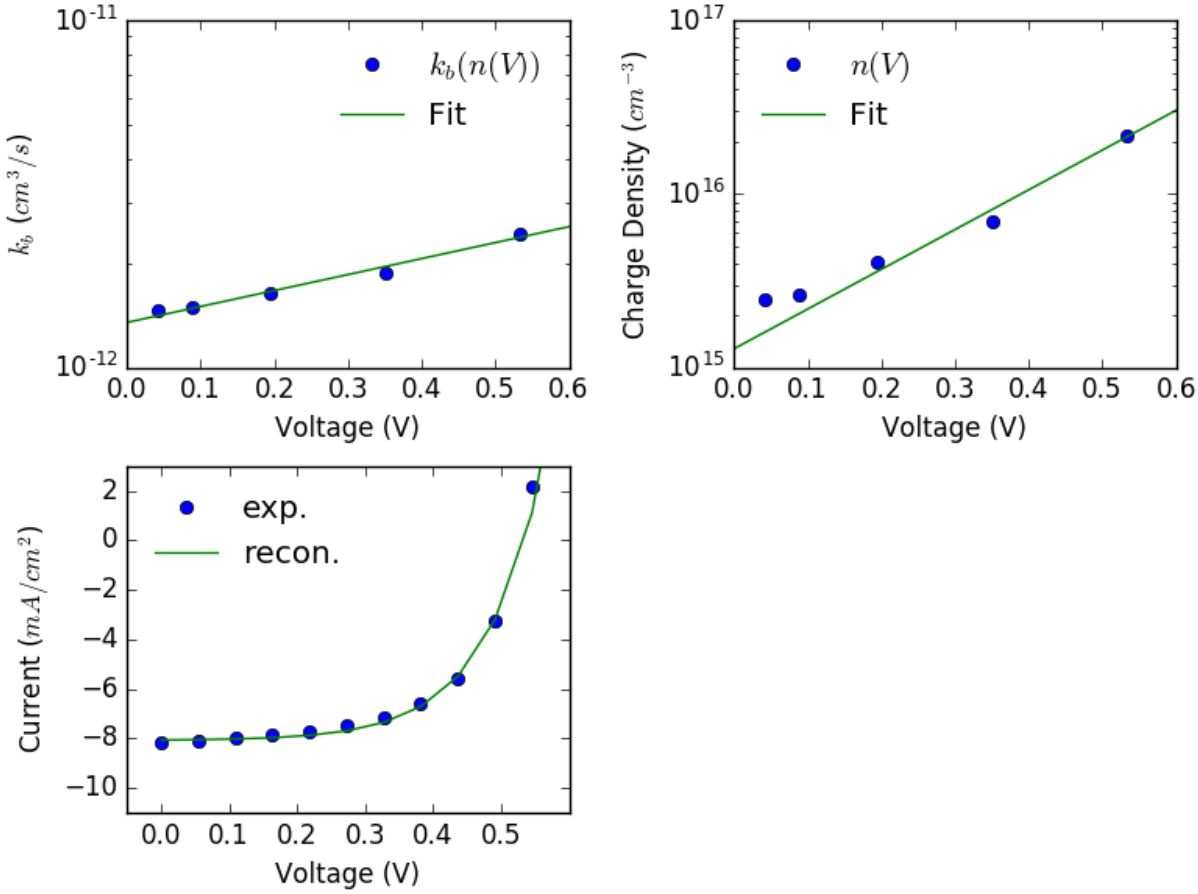

Figure 7-8. (a) Bimolecular recombination coefficient (b) charge density (c) measured and reconstructed J-V curves as a function of n and $n(V)$

OPV48:PCBM OSC

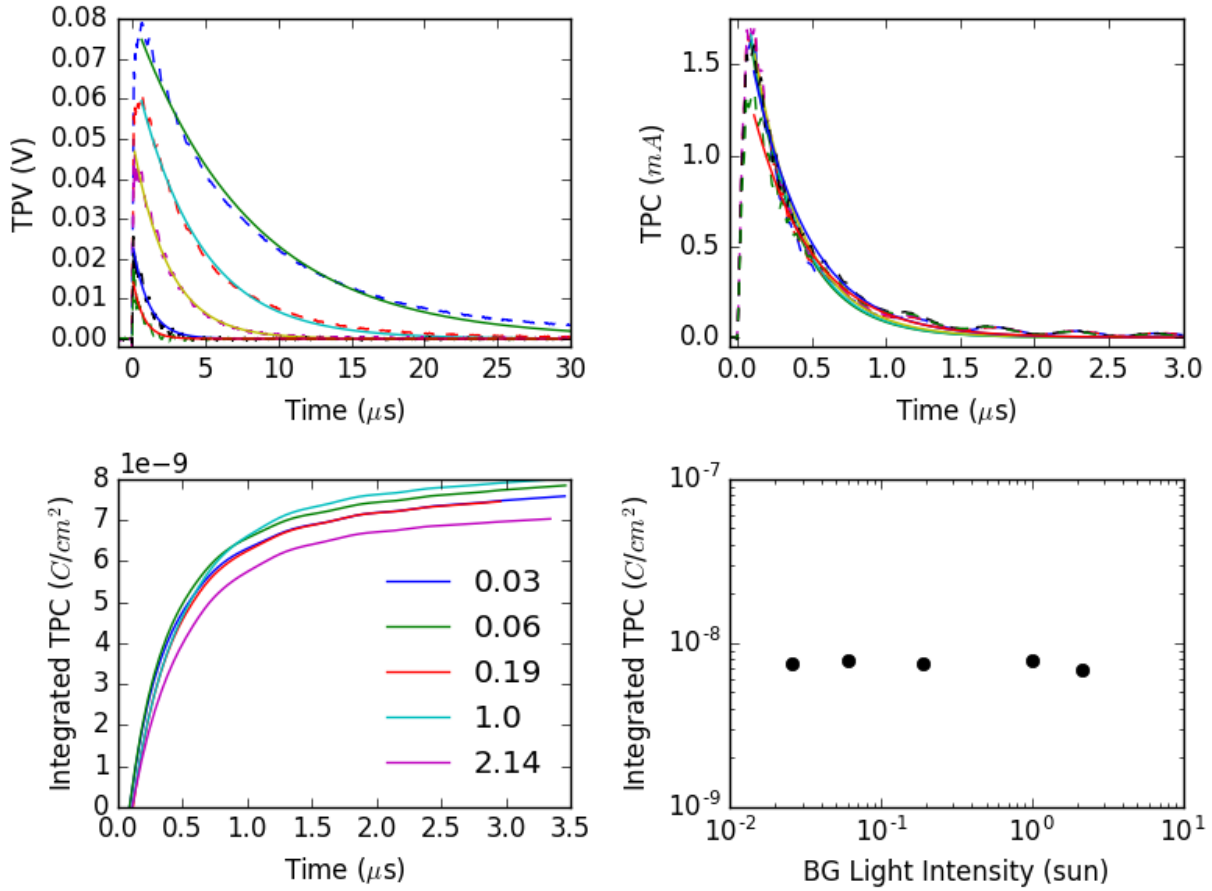

Figure 7-9. (a) TPV (b) TPC traces, and (c,d) integrated TPC, as a function of BG light intensity (0.02-3.74 suns)

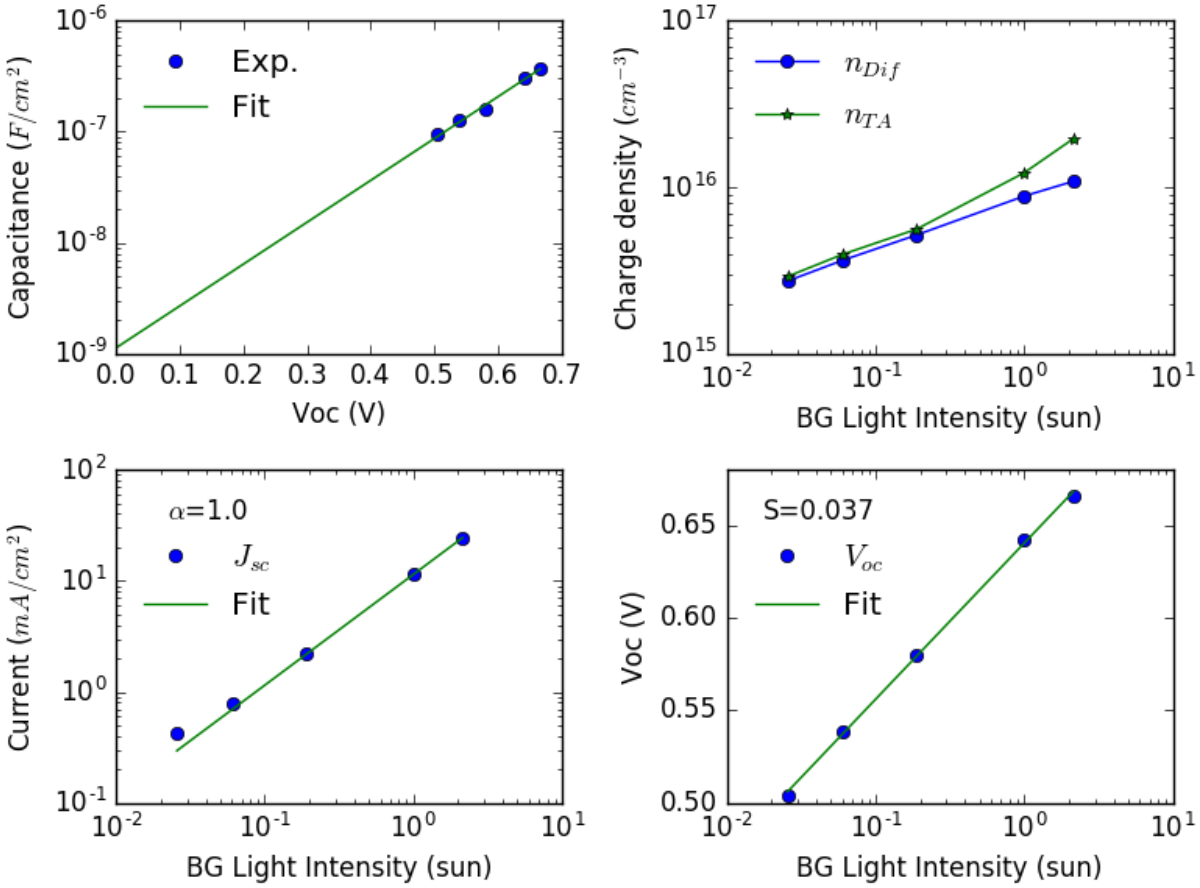

Figure 7-10. (a) Differential capacitance as a function of open circuit voltage; (b) charge density (c) short circuit current (d) open circuit voltage as a function of BG ground light intensity, respectively

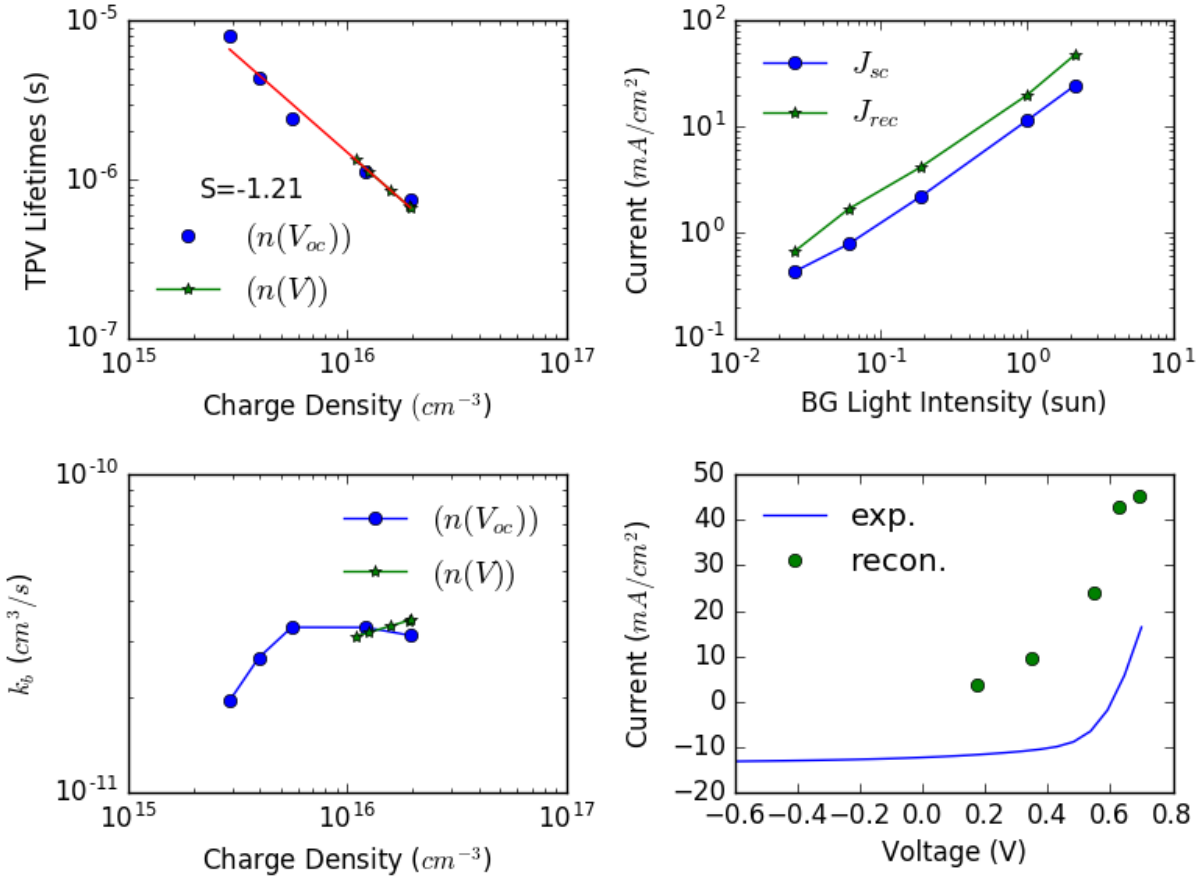

Sv=

Figure 7-11TPV lifetime as a function of charge density; (b) short circuit and recombination current density (c) bimolecular recombination coefficient as a function of BG ground light intensity, respectively; (d) measured and reconstructed J-V curves

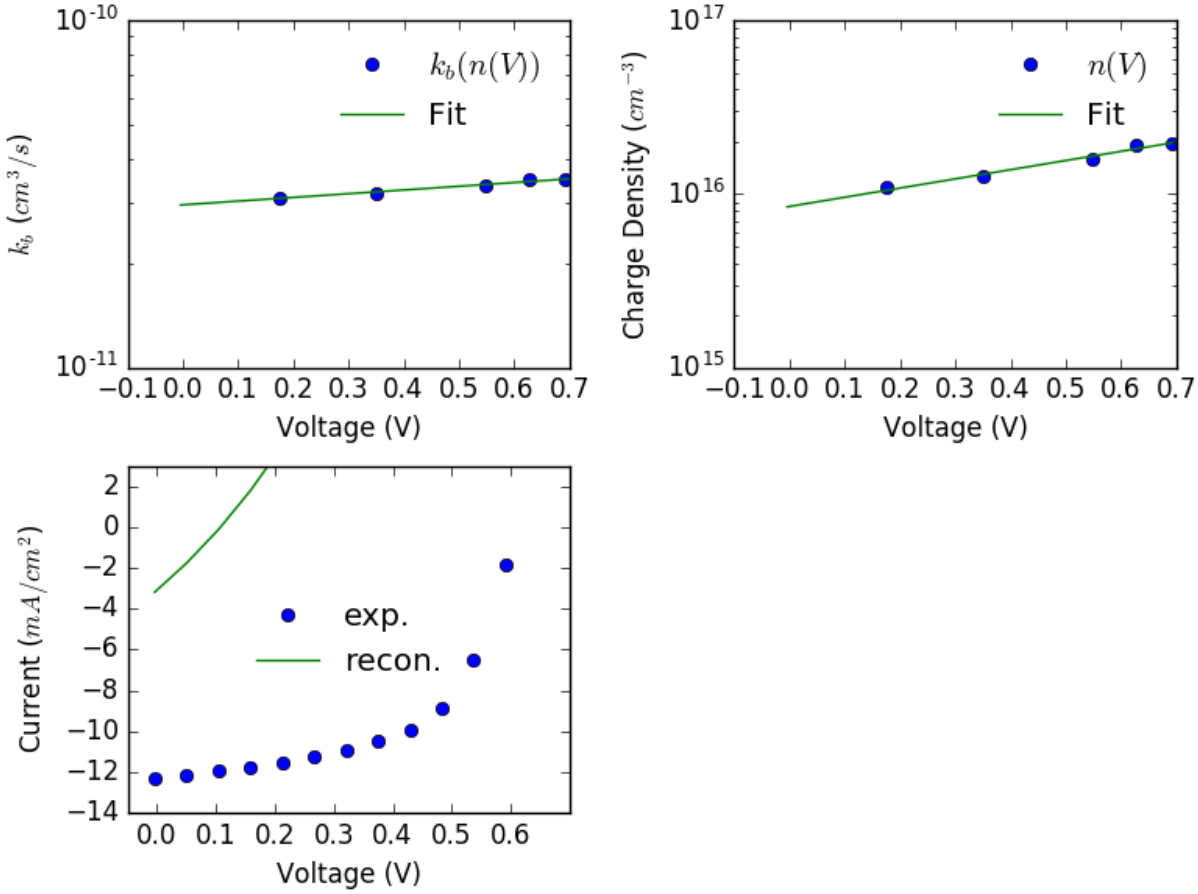

Figure 7-12. (a) Bimolecular recombination coefficient (b) charge density (c) measured and reconstructed J-V curves as a function of n and $n(V)$

OPV48:PCBM:SWNT OSC

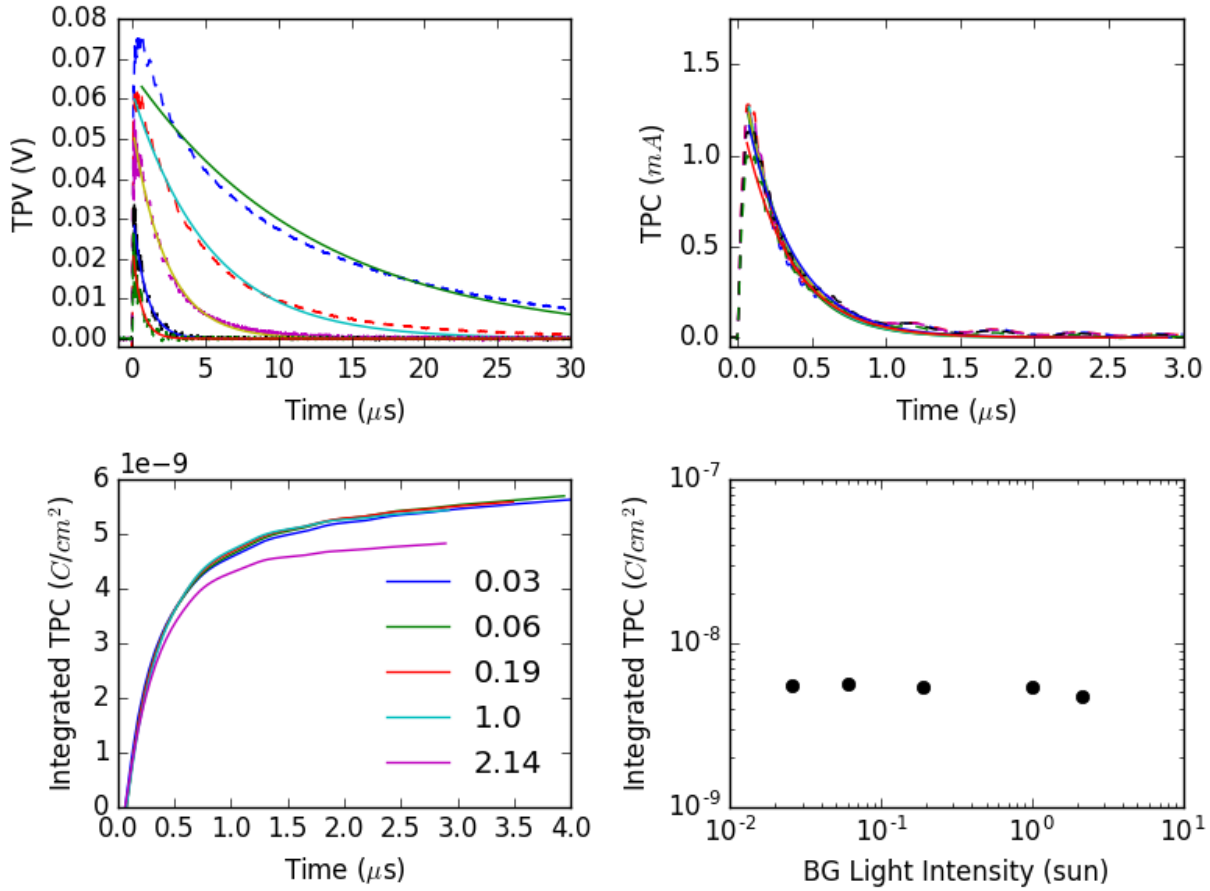

Figure 7-13. (a) TPV (b) TPC traces, and (c,d) integrated TPC, as a function of BG light intensity (0.02-3.74 suns)

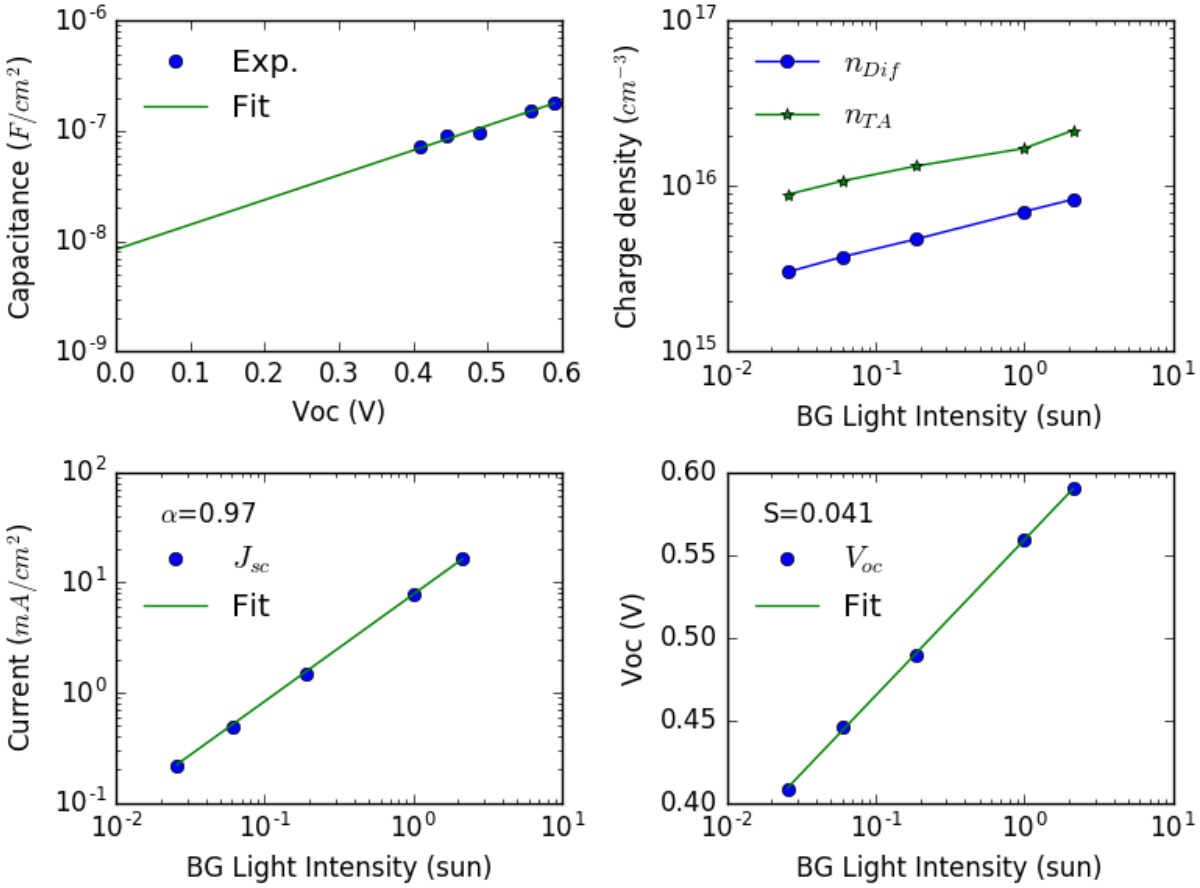

Figure 7-14. (a) Differential capacitance as a function of open circuit voltage; (b) charge density (c) short circuit current (d) open circuit voltage as a function of BG ground light intensity, respectively

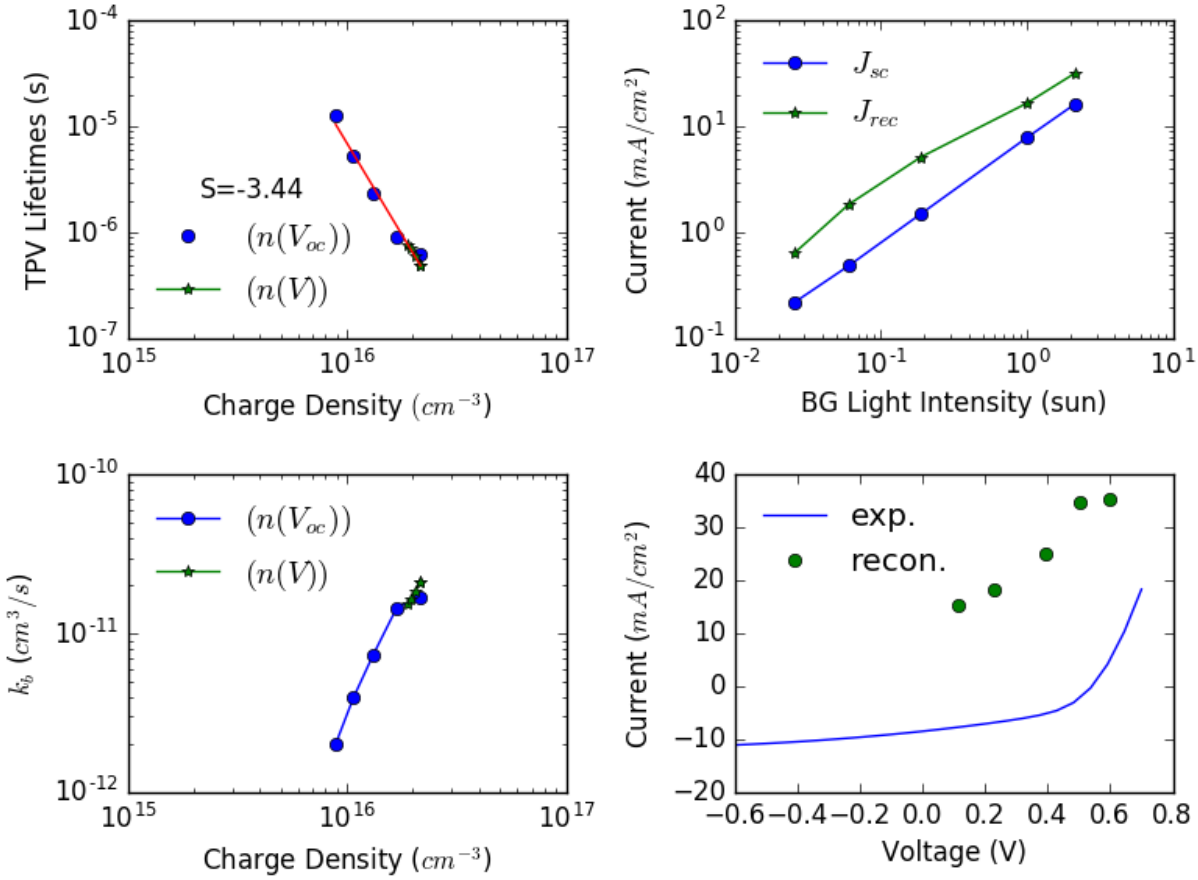

Sv=

Figure 7-15. TPV lifetime as a function of charge density; (b) short circuit and recombination current density (c) bimolecular recombination coefficient as a function of BG ground light intensity, respectively; (d) measured and reconstructed J-V curves

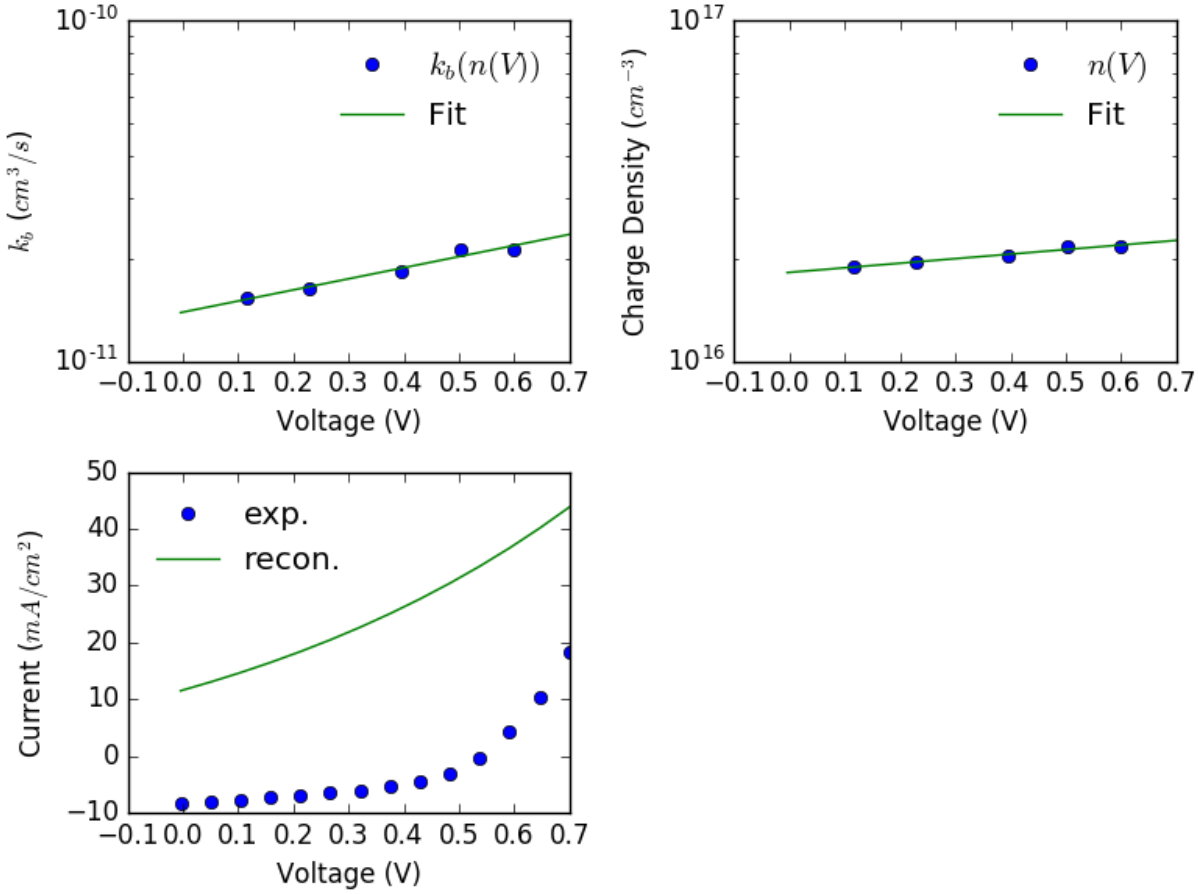

Figure 7-16. (a) Bimolecular recombination coefficient (b) charge density (c) measured and reconstructed J-V curves as a function of n and $n(V)$

Femtosecond Transient Absorption Spectra

P3HT:PCBM OSC

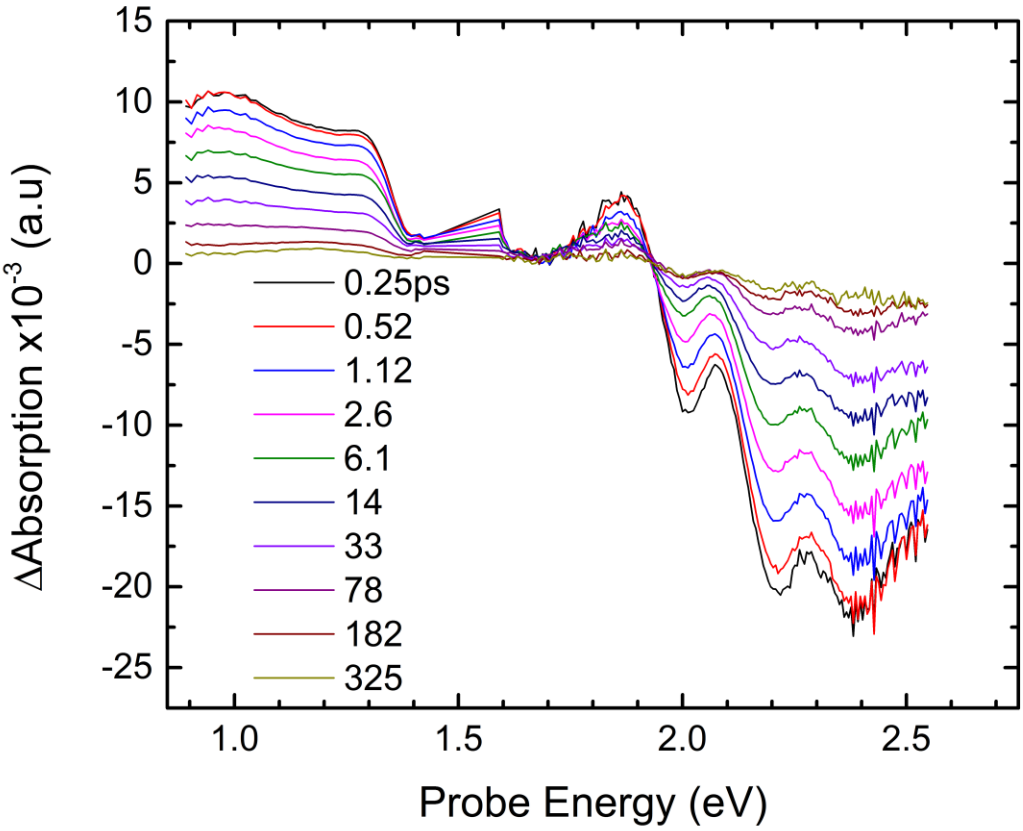

P3HT:PCBM:SWNT OSC

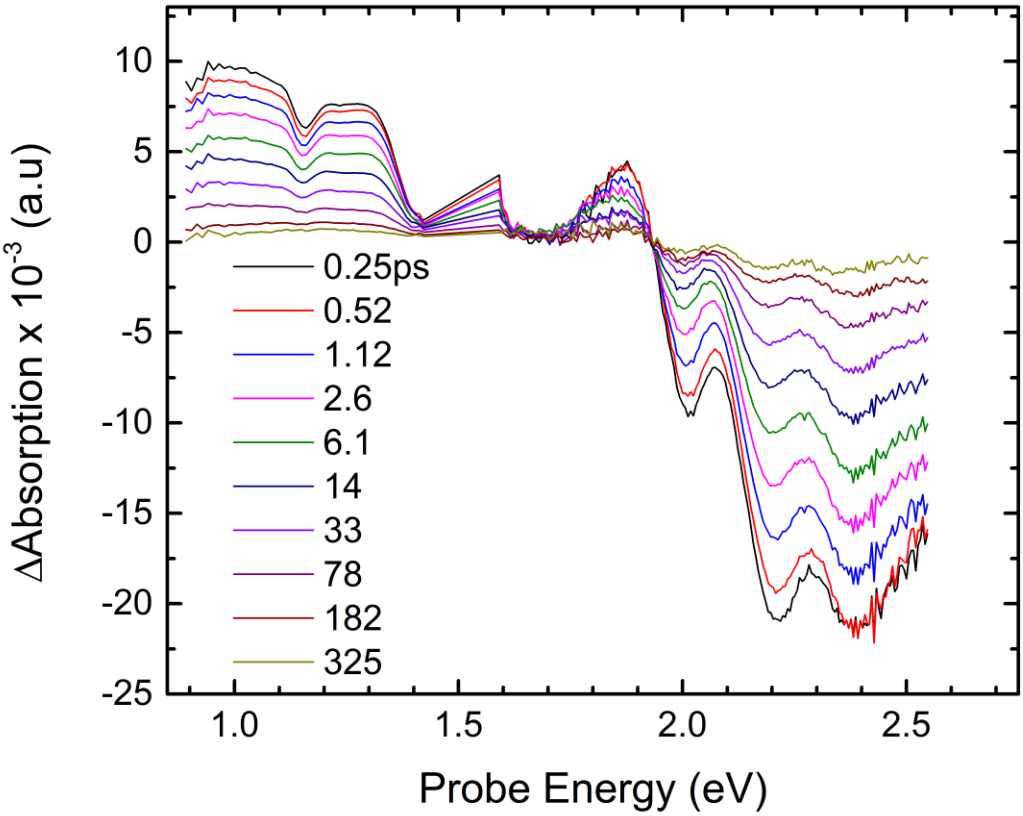

OPV48:PCBM OSC

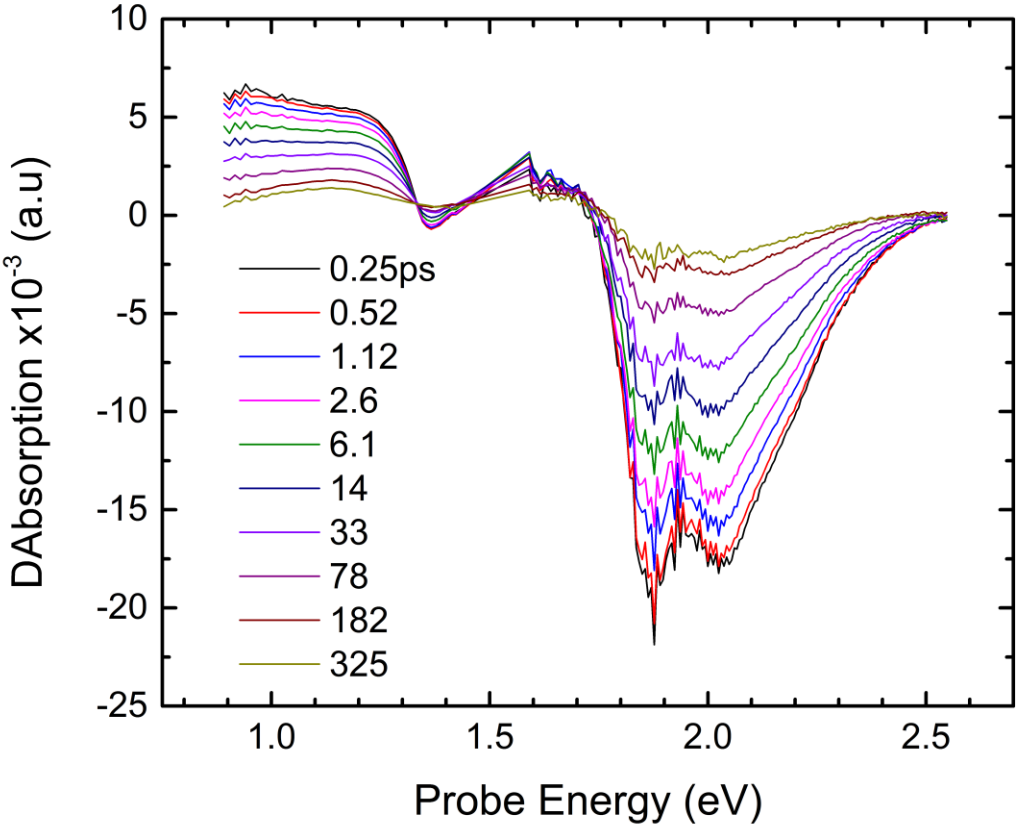

OPV48:PCBM:SWNT OSC

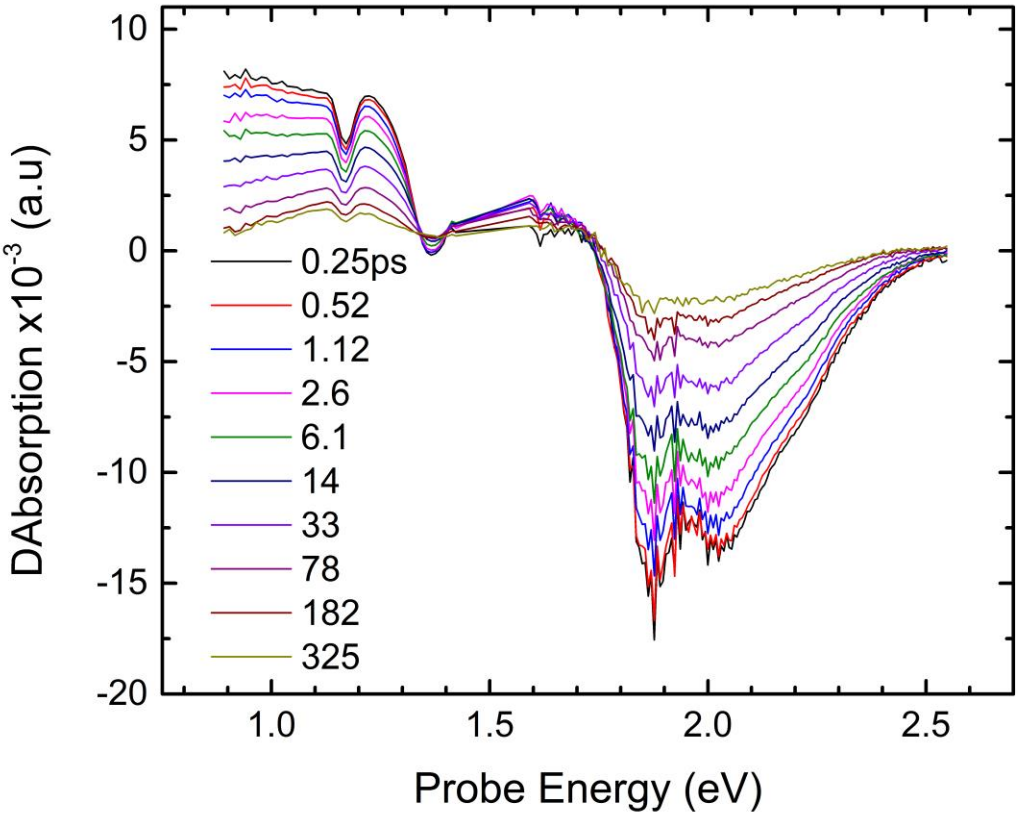

Charge Density Obtained by Microsecond Transient Absorption Spectroscopy

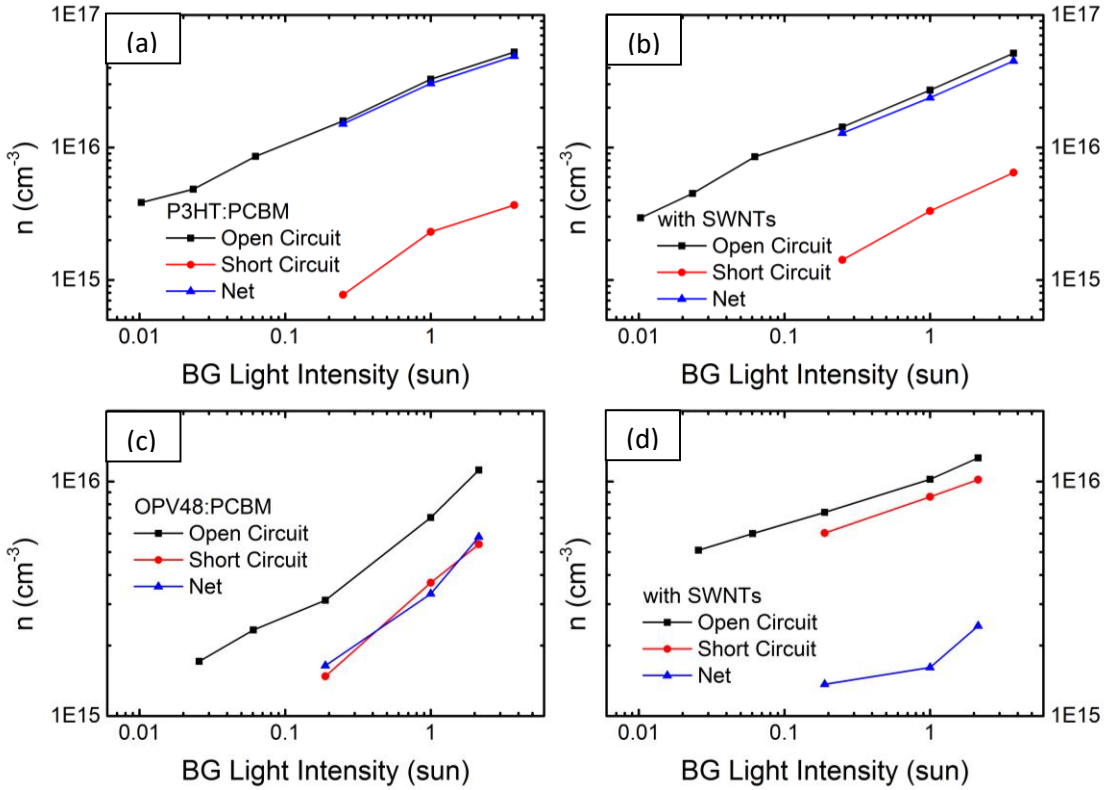

Figure 7-17. Charge density n measured with microsecond TA spectroscopy at open and short circuits as a function of BG light intensity in P3HT:PCBM (a,b) and OPV48:PCBM (c,d) devices with/without SWNTs; the Net means: $n(Net) = n(open\ circuit) - n(short\ circuit)$

Field Effect Transistor Electrical Characteristics

(7,5) SWNT/PFO OD 1

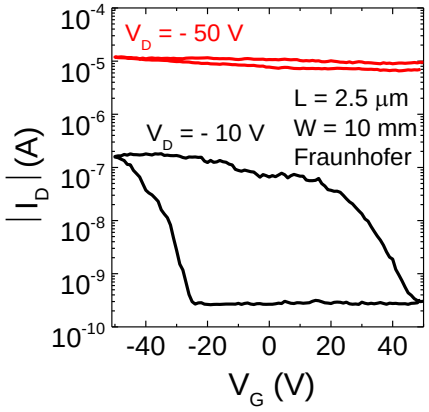

(7,5) SWNT/PFO OD 10

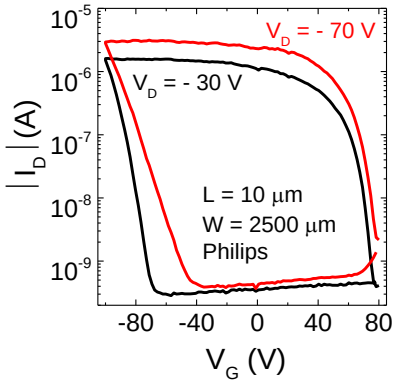

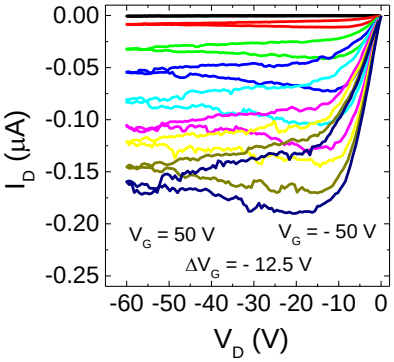

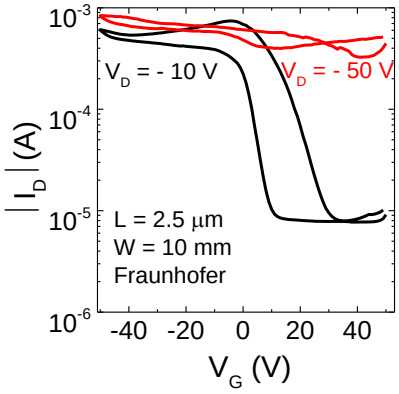

(7,5) SWNT/PFO OD 30

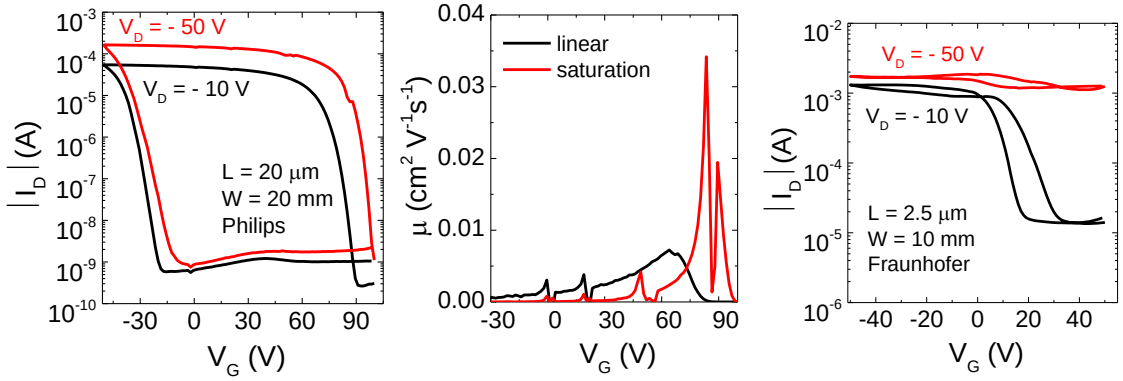

(6,5) SWNT/PFO-BPy OD 1.5

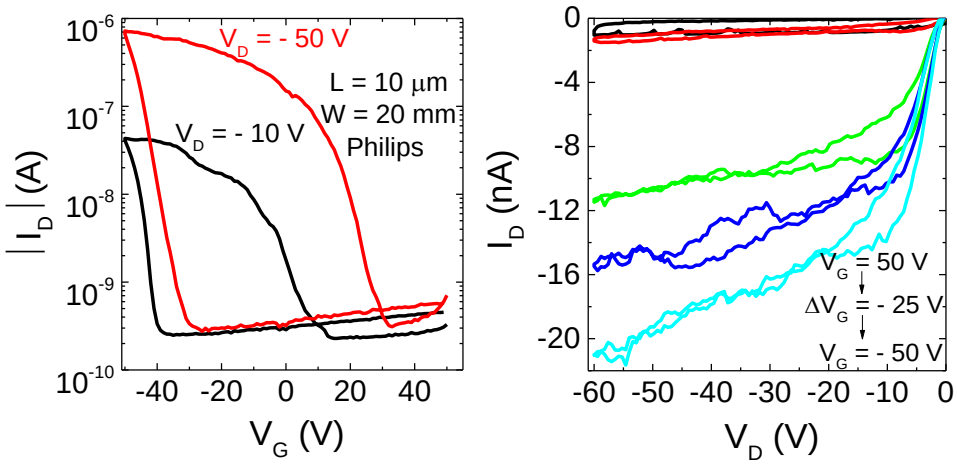

(6,5) SWNT/PFO-BPy OD 10.5 (bundle)

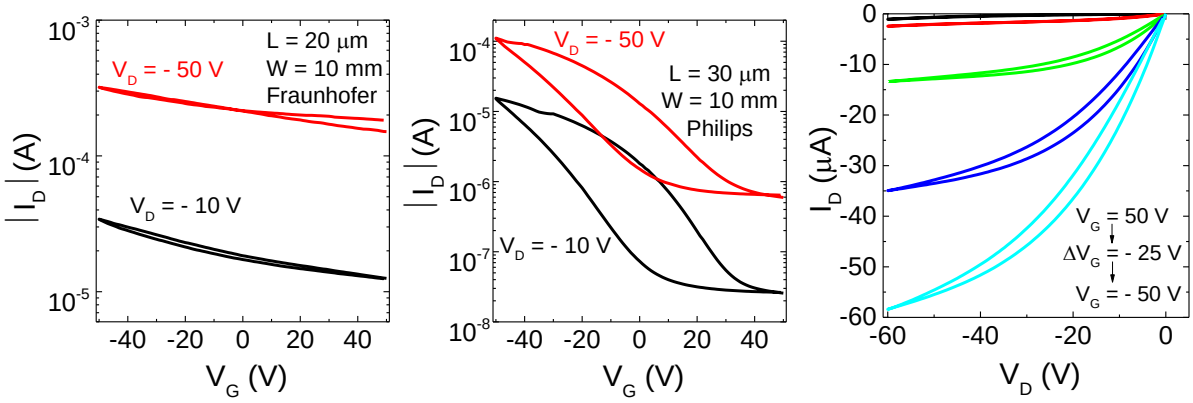

(6,5) SWNT/PFO-BPy OD 27.5

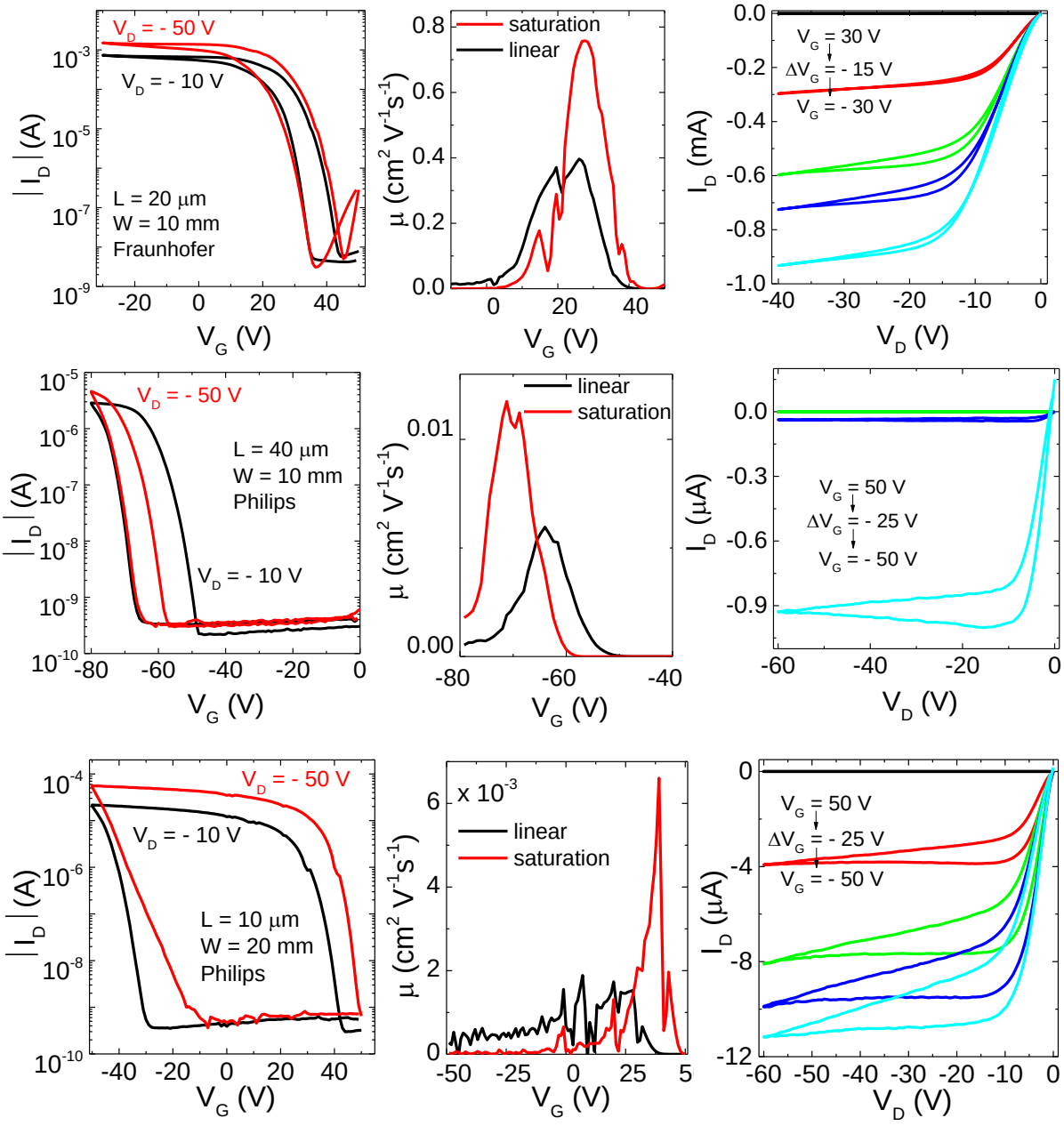
V_D = - 50 V
V_D = - 10 V
L = 20 µm
W = 10 mm
Fraunhofer
|I_D| (A)
V_G (V)
saturation
linear
µ (cm² V⁻¹s⁻¹)
V_G = 30 V
ΔV_G = - 15 V
V_G = - 30 V
I_D (mA)
V_D (V)
L = 40 µm
W = 10 mm
Philips
V_G = 50 V
ΔV_G = - 25 V
V_G = - 50 V
I_D (µA)
L = 10 µm
W = 20 mm
Philips
x 10⁻³